# Laser Cooling and Trapping of $^6$Li: Experimental Tools for Many-Body Fermionic Dynamics and Ring Trap

Xinxin Tang

A dissertation
submitted in partial fulfillment of the
requirements for the degree of

Doctor of Philosophy

University of Washington

2023

Reading Committee:

Subhadeep Gupta, Chair

Boris Blinov

Sara Mouradian

Program Authorized to Offer Degree:
Physics

University of Washington

**Abstract**

Laser Cooling and Trapping of $^6$Li: Experimental Tools for Many-Body Fermionic Dynamics and Ring Trap

Xinxin Tang

Chair of the Supervisory Committee:
Subhadeep Gupta
Department of Physics

This thesis delves into the laser cooling and trapping of $^6$Li, a fermionic atom, with the aim of creating experimental tools for the exploration of many-body fermionic dynamics in quantum degeneracy, specifically within ring traps. We provide an overview of $^6$Li properties, the theoretical underpinnings of many-body fermionic dynamics in cold atom traps, and the principles of AC Stark shift in far-off-resonance light fields. Our experimental apparatus, capable of trapping Yb and Li, and completed experiments on YbLi Magnetic Feshbach Resonance (MFR) and Yb bosonic dynamics are detailed, along with technical adaptations for laser cooling and trapping of $^6$Li towards a single-species Fermi condensate. We discuss our sub-Doppler cooling system, magnetic field stabilization method, and progress towards quantum degeneracy, as well as a developed method of optical pulses to induce dynamics in the paired Fermi condensate. Our work on ring traps and entrainment, including the development of a ring beam setup using a Digital Micromirror Device (DMD), is also elaborated. The thesis concludes by underscoring the significance of our developments in the context of many-body fermionic dynamics in quantum degeneracy and the use of ring traps for studying dual-superfluid systems, contributing to the broader field of ultracold atomic physics.

# ACKNOWLEDGMENTS

From the earliest chapters of my life, my curiosity for the natural sciences has been a steadfast companion. My grandmother fondly recalls my kindergarten days, where I found an inseparable friend in a popular science book for Chinese children titled "One Hundred Thousand Whys." When applying to this PhD program from my alma mater, the University of Science and Technology of China, I declared physics as my "singular focus in life," a statement that was not an exaggeration but a testament to my passion. Over the past six years at the University of Washington, I have had the extraordinary opportunity to live out my childhood dream as an experimental physicist. The intricate elegance of atomic and quantum physics, intertwined with the tangible application of engineering optical and electronic systems, has brought me a level of fulfillment that my younger self could only have imagined.

I am profoundly grateful to my PhD advisor, Prof. Subhadeep Gupta. His deep expertise, patient guidance, and thought-provoking discussions have been instrumental in shaping my understanding of our field and fostering both my academic and personal growth. His intricately designed Yb-Li apparatus has been a constant source of inspiration, and his regular lab visits have been invaluable in my development as a physicist. His high expectations and rigorous standards have often pushed me to reach beyond my limits and strive for perfection, leading to many moments of intense learning and growth. These challenges have ultimately shaped me into a more resilient and capable individual. I am leaving this experience not just as a more knowledgeable physicist, but also as a stronger person, better equipped to face demanding challenges in my future. His mentorship has been a defining aspect of my PhD journey, and for that, I am deeply appreciative.

I had the privilege of having Alaina Green as a mentor from 2017 to 2019. During this time, she led our team's efforts on the Photoassociation project and the YbLi Magnetic

Feshbach Resonance project. Her hands-on approach to problem-solving was transformative, shifting my perspective from the "lectures and homework" mindset of my high school and college days to a more practical, application-oriented approach to physics. Our friendship has continued beyond our PhD programs, and I am deeply appreciative of the energy and enthusiasm she brought to our shared journey.

I extend my deepest appreciation to my colleague, Jun Hui See Toh, who worked alongside me from 2017 to 2022. Our numerous conversations and shared experiences have forged a bond that continues beyond our PhD programs. I cherish the memory of the excitement we shared while collecting the Yb dynamical delocalization data, and the strength of our teamwork in untangling the myriad of technical problems in our complex machine.

I was fortunate to collaborate with Katie McCormick during her time as our postdoc from 2019 to 2021. Her extensive knowledge and exceptional skills were invaluable in addressing complex engineering problems in magnetic field stabilization and DMD prototype testing, among others.

From 2022 to 2023, I had the enriching experience of leading our team's efforts and mentoring the talented new members of our team. Carson Patterson, with her expertise in optical engineering, played a crucial role in overcoming intricate challenges such as optical system design and alignment. Nicolas "Cole" Williams, on the other hand, impressed me with his relentless diligence and astute intellect. His ability to quickly grasp technical details and dissect complex scientific concepts served as a constant source of inspiration. This period provided me with the rewarding opportunity to share the knowledge and experience I had gained in this lab, while also honing my skills as an effective and compassionate mentor. I am deeply grateful for this experience and the growth it has fostered in me, both professionally and personally.

I would like to express my gratitude to our diligent undergraduate researchers, including Yifei Bai and Olivia Peek, among others. The opportunity to mentor them and delve into the details of our work has not only solidified my own understanding but also honed my mentorship skills. I have found great joy in learning about their unique perspectives and

witnessing their academic journeys unfold.

I am also thankful for the enriching discussions and shared resources with members of our sibling lab in the Gupta Group, including Daniel Gochnauer, Katie McAlpine, Tahiyat Rahman, and others. My friendship with Anna Wirth has been a source of enjoyment and camaraderie, from her time in our sibling lab to her transition to Prof. Arka Majumdar's Opto-Electronics Lab. These relationships have added a valuable dimension to my experience in the Physics Department.

My heartfelt gratitude extends to my family for their unrelenting support throughout my career. Despite a time zone difference of 16 hours and the vast expanse of the Pacific Ocean separating us, my beloved mother, Yanmei Tang, has made every effort to maintain our connection. My cherished grandmother, Yunxiu Deng, was my guardian for the first 18 years of my life. As a lifelong educator, her encouragement has been instrumental in paving the path to my academic success. I am also immensely grateful to my extended family for their loving care of my grandma and for facilitating our frequent video calls, ensuring that our bond remains strong despite the geographical distance.

I would like to extend my deepest appreciation to my dear friends in the Physics Department, including Maria Viitaniemi, Jennifer "Jenny" Lilieholm, Liudmila "Mila" Zhukas, Zeeshawn Kazi, Christian Pederson, and many others. Their unwavering support and camaraderie have been invaluable in helping me navigate the challenges of this journey, contributing significantly to my development not only as a physicist but also as a person. I am also immensely grateful to my dear friend and neighbor Jeremy Williams, who has been a constant source of encouragement and compassion throughout our time living in the same apartment building. Our meaningful late-night conversations and shared guitar lessons have enriched my life in immeasurable ways.

Reflecting on the past six years, I am filled with pride at the remarkable achievements of our research team, including our contributions to esteemed journals such as Physical Review X (PRX) and Nature Physics. As I stand on the precipice of completing my PhD journey, I am eager to apply the skills and experiences I have garnered to make a meaningful impact

in the world in the next phase of my career.

*In loving memory of my grandpa, Donglin Tang (1934-2022).*

## TABLE OF CONTENTS

Page

## LIST OF FIGURES

## LIST OF TABLES

# Chapter 1

# INTRODUCTION

Laser cooling and trapping of atomic gases has revolutionized our ability to study and control quantum systems with unprecedented precision. This technique, first proposed independently by Hansch and Schawlow [38] and Wineland and Dehmelt [84] in 1975, has led to exciting discoveries in the fields of quantum information, many-body physics, and precision measurement.

In this thesis (completed in Summer 2023), we focus on laser cooling and trapping of $^6$Li, a fermionic atom with a light atomic mass of 6 atomic mass unit (amu) and a nuclear spin of 1. Our primary goal is to develop experimental tools for studying many-body fermionic dynamics in quantum degeneracy, and in particular for ring traps.

The study of many-body fermionic dynamics is of fundamental importance in physics and has applications in a variety of fields, including condensed matter physics, nuclear physics, and astrophysics. The behavior of fermions at low temperatures can exhibit fascinating phenomena such as fermion pairing, BEC-BCS crossover, and phonon-mediated coupling, leading to further understanding of superfluidity and superconductivity.

In this thesis, we provide an overview of the properties of $^6$Li, the theoretical background of many-body fermionic dynamics in cold atom traps, and the fundamental principles of AC Stark shift in far-off-resonance light fields, which underlie the technologies in optical lattices, optical dipole traps, and temporally-modulated standing-wave potentials used to induce quantum dynamics.

We then present our experimental apparatus, which is capable of cooling and trapping Yb and Li atoms, and our completed experiments on the YbLi magnetic Feshbach resonance and bosonic $^{174}$Yb Quantum Kicked Rotor. We detail the technical adaptations and upgrades we made to our existing apparatus to perform laser cooling and trapping of $^6$Li, including our sub-Doppler cooling system that utilizes the D1 transition lines of $^6$Li. We discuss

loading $^6$Li atoms into our Optical Dipole Trap (ODT), which enables evaporative cooling of a spin-mixture of $^6$Li inside our ODT.

We also describe our method and results in stabilizing our large bias magnetic field to a few parts per million level, which will pave the way to accessing the narrow lines in p-wave and s-wave resonances of $^6$Li ensembles. We discuss the use of short pulses of standing-wave potentials to induce the quantum dynamics of $^6$Li and the technical revisions and upgrades we have achieved for this purpose.

We outline our experimental progress and achievements, which include advancements in cooling towards quantum degeneracy and the successful generation of short optical pulses for the investigation of many-body fermionic dynamics. Furthermore, we delve into the motivation, theoretical underpinnings, and future prospects of studying the Quantum Kicked Rotor within the context of paired fermions.

We then discuss our work on ring traps and entrainment. We explain the motivation behind using complex patterned traps, including non-trivial topology traps like ring traps, the physics of single-superfluid effects like the Josephson effect, phase slips and matter wave interference, and the appeal of developing homogeneous optical box traps for precise study of long-term quantum transport behaviors. We elaborate on the entrainment effect in dual-superfluid systems and our proposed experimental protocol for this study. We discuss our method and progress to develop a ring beam setup using a Digital Micromirror Device (DMD), along with the characterization of the ring beam in comparison to our desired figure of merit, including the technical details of parameters such as size scales and smoothness of the trap. We present our plans for studying entrainment in dual-superfluid systems and discuss the implications of our expected findings for future research directions in the field of ultracold atomic physics.

Finally, we summarize the key progress, findings, and their significance in the context of new insights into the behavior of many-body fermionic dynamics in quantum degeneracy, as well as the use of ring traps as experimental tools for studying dual-superfluid systems. We discuss the future directions of our lab's endeavor built upon our established progress detailed in this thesis.

# Chapter 2

# BACKGROUND

This chapter provides the necessary background information for understanding the experimental and theoretical aspects of our research on laser cooling and trapping of $^6$Li. We begin by discussing the properties of $^6$Li, the atom central to our investigations. We then delve into the mean-field theory, exploring its limitations in the presence of strong interactions and the emergence of fermion pairing and the BEC-BCS crossover. Additionally, we provide a brief overview of the experimental apparatus used in our research, highlighting its dual-species capabilities and the utilization of atom optics kicked rotor and the completed experiments in the recent years. Finally, we will delve into the technical details of AC Stark shift from Far-Off-Resonance light fields, and its applications in Optical Dipole Trap (ODT), Optical Lattice, and pulsed standing waves potentials.

In this chapter, we will explore the fundamental concepts and theoretical foundations that underpin our study of $^6$Li. By gaining a solid understanding of these key elements, we can delve deeper into the intricacies of our experimental investigations and their implications for the broader field of ultracold atomic physics.

## *2.1 Properties of $^6$Li*

This section focuses on the key properties of $^6$Li, a fermionic atom with a light atomic mass and a nuclear spin of I=1. Understanding the specific properties of $^6$Li is essential for comprehending its behavior under laser cooling and trapping, as well as its role in the dynamics of many-body fermionic systems.

### *2.1.1 Atomic Structure and Energy Levels*

$^6$Li, like all lithium isotopes, has three electrons. Two of these electrons fill the 1s shell, and the third resides in the 2s shell, making lithium a member of the alkali metals. The

energy levels of $^6$Li can be calculated using quantum mechanics, and the results are crucial for understanding its spectroscopic properties. As shown in Figure 2.1, the $2\,^2S_{1/2}$ ground state of $^6$Li splits into two hyperfine levels, separated by $h\times$228.2MHz [26], where $h$ is the Planck constant.

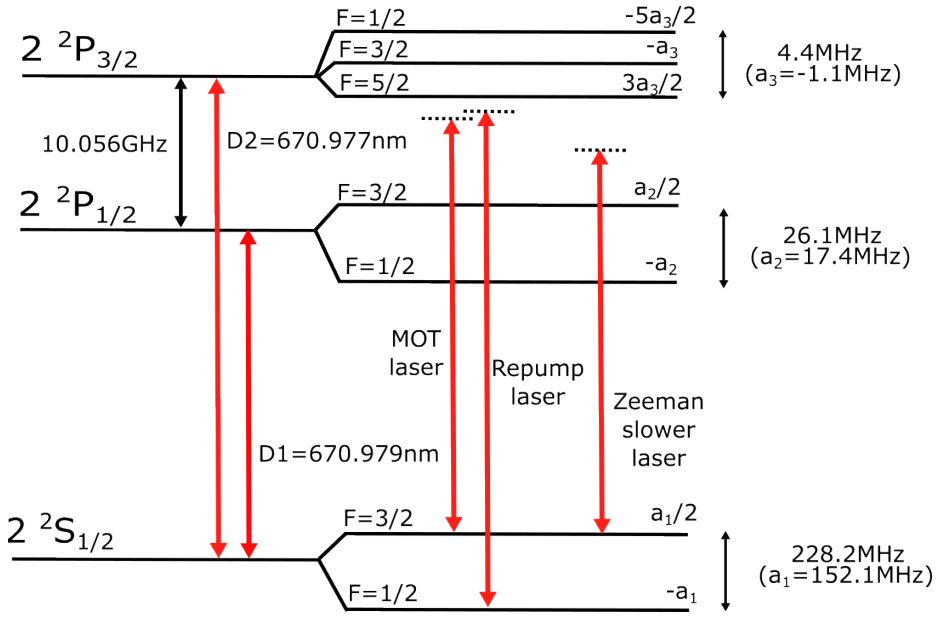


Figure 2.1: Level diagram of the ground and 2P excited states of $^6$Li [26] and the various lasers used in our apparatus, with detunings discussed in Chapter 3. Energy splittings are not to scale. The natural linewidths for D1 transition and D2 transition are both $\Gamma = 2\pi\times$ 5.8724MHz.

The hyperfine structure of $^6$Li arises from the interaction between the nuclear magnetic momemt and the electronic magnetic moment. This interaction leads to a splitting of the energy levels of $^6$Li, which manifests as multiple spectral lines during the absorption or emission of light. The hyperfine structure plays a significant role in laser cooling and trapping experiments, as it facilitates the selective excitation of $^6$Li atoms. In the presence of external magnetic field, the magnetic substates within the hyperfine structure experience different Zeeman shift based on their magnetic quantum number, and this dependence of atomic magnetic substate energy on the external magnetic field (Figure 2.2) enables cooling

and trapping mechanisms like Zeeman slower and Magneto-Optical Traps (MOTs).

$^6$Li has cycling transitions in the D2 line from $|F, m_F\rangle = |3/2, -3/2\rangle$ to $|F', m'_F\rangle = |5/2, -5/2\rangle$, and another one from $|F, m_F\rangle = |3/2, +3/2\rangle$ to $|F', m'_F\rangle = |5/2, +5/2\rangle$; the electric/magnetic dipole selection rule $\Delta m_F = 0, \pm 1$ and the atomic states in the ground state dictate that the spontaneous emission from these excited states must return the atom to the corresponding starting state. However, as shown in Figure 2.1, the hyperfine splitting of 4.4MHz in the $2\,^2P_{3/2}$ excited state of $^6$Li is narrower than the natural linewidth of the D2 transition, and in practice the laser cooling process will inevitably excite a fraction of the atom population to other hyperfine states in the $2\,^2P_{3/2}$ level, which will spontaneously decay to a dark state in $2\,^2S_{1/2}$ with $F = 1/2$ and become unable to be addressed by the same cooling laser beam anymore. Therefore, in processes like laser cooling or Zeeman slowing, a repumping beam is necessary to transition the atoms out of the dark state. This repumping beam ensures that the atoms remain in a cycle of absorption and emission, which is crucial for maintaining the cooling and trapping processes.

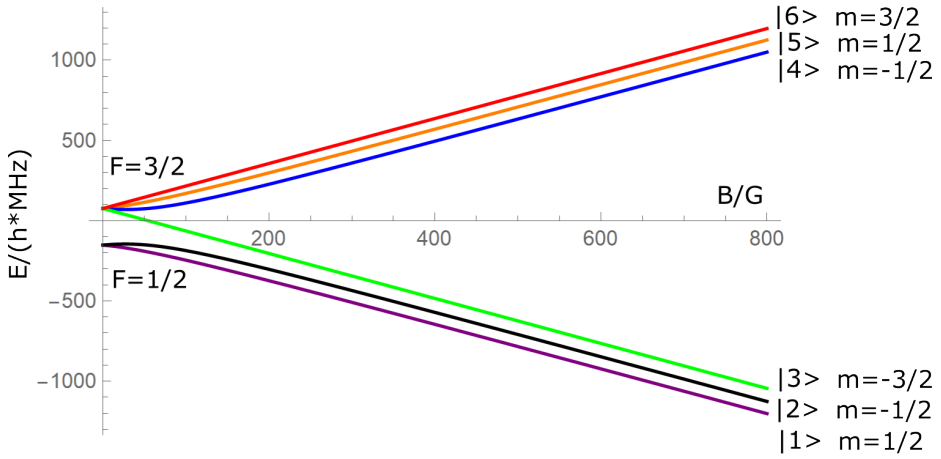


Figure 2.2: Magnetic-field dependence of the $2\,^2S_{1/2}$ ground state of $^6$Li based on the Breit-Rabi formula. For ultracold temperatures, the most relevant magnetic substates are State 1 (F=1/2, $m_F$=+1/2) and State 2 (F=1/2, $m_F$=-1/2), as they have the lowest energy.

### *2.1.2 Atomic transitions and optical properties*

$^6$Li is well-suited to laser cooling and trapping due to its single electron structure and the optical properties that stem from its atomic transitions. When a two-level atom interacts with an optical field that is nearly resonant, this interaction coherently drives the atom to oscillate between these two quantum levels, which is known as the Rabi oscillation. The frequency of this oscillation, known as the optical Rabi frequency, can be determined by

$$\begin{aligned} \Omega &= \frac{\langle b| \hat{\mu} \cdot \mathbf{E} |a\rangle}{h} \\ &= \frac{\mu_{ba} E_0}{h} \end{aligned} \tag{2.1}$$

In the formula above, $\mu_{ba}$ signifies the electric-dipole transition matrix component for states a and b, while $E_0$ corresponds to the strength of the electric field of the optical field. When the Rabi frequency falls below the spontaneous decay rate $\Gamma$, the atom has a higher chance of undergoing spontaneous decay from the excited state rather than being coherently manipulated by the applied field. For higher intensity of the optical field and higher strength of its electric field, the Rabi frequency begins to outpace the spontaneous decay rate, leading to a stronger coherent interaction between the atom and light.

In the scenario where $\Omega \gg \Gamma$, the coherent driving dominates over the spontaneous decay in the short term, leading to coherent oscillations between the ground and excited states. Over the long term, however, spontaneous emission may eventually lead the system to reach a steady state. In this state, the atomic population appears evenly distributed between the ground and excited states, and any further increase in light intensity has no impact on the state populations. This stage is referred to as the saturation of the transition, where the coherent drive is balanced by spontaneous emission, resulting in a stable population distribution.

If we assume the light field's intensity to be $I = (1/2)c\epsilon_0 E^2$ where $c$ is the speed of light and $\epsilon_0$ is the vacuum permittivity, we can define a saturation intensity as follows:

$$I_{sat} = \frac{c\epsilon_0 \Gamma^2 \hbar^2}{4|\mu \cdot \mathbf{e}|^2} \tag{2.2}$$

In the equation above, **e** is the unit vector indicating the polarization of the optical field such that $\mathbf{E} = E_0\mathbf{e}$. Based on this definition, we have the relation $I/I_{sat} = 2(\Omega/\Gamma)^2$. The saturation intensity is specific to each transition. For the circularly polarized light addressing the D2 line in $^6$Li MOT, the saturation intensity is 2.54 mW/cm$^2$ [26].

For the optical molasses cooling technique utilized in a Magneto-Optical Trap (MOT), the Doppler cooling theory[1] predicts the lowest temperature expected as the Doppler limit $T_D = \hbar\Gamma/(2k_B)$, where $\hbar = h/(2\pi)$ is the reduced Planck constant and $k_B$ is the Boltzmann constant. For $^6$Li D2 line, this calculates to about 141 $\mu$K. Beyond that, the hyperfine structure of $^6$Li ground state enables the use of its D1 transition for gray molasses to achieve sub-Doppler cooling, which can further lower the temperature of a $^6$Li gas [69].

### *2.1.3 Scattering Properties*

A typical moderate atomic number density for the gas in a MOT is about $1 \times 10^{11} cm^{-3}$, which equates to a mean free path of 2.154$\mu$m. Meanwhile, with atomic mass $m$ =6 a.m.u. (atomic mass unit), the de Broglie wavelength $\lambda_{dB} = h/\sqrt{3mk_BT}$ for a $^6$Li atom at T=1$\mu$K is calculated to be 0.712$\mu$m. This implies that the majority of collisions in the ensemble are binary collisions (involving only two atoms). For $^6$Li+$^6$Li collisions, the interaction potential is a combination of the molecular singlet and triplet interaction potentials. In the singlet potential, the two atoms approach with their unpaired electronic spins antiparallel, whereas in the triplet potential, the two spins approach in the parallel configuration.

In the context of quantum mechanics, the scattering problem between two particles can be solved using partial-wave expansion; this is also known as the partial-wave analysis. In the case of an ultracold bosonic gas, the s-wave component of the partial wave analysis dominates. However, in the case of identical fermions in identical internal states, s-wave scattering interactions are forbidden, as s-wave scattering requires spatial wavefunctions with exchange symmetry that are forbidden by the Pauli exclusion principle. But in the case of a mixture of fermionic atoms in different internal states, like a spin mixture of $^6$Li atoms in the lowest-energy magnetic substates State 1 (F=1/2, $m_F$=+1/2) and State 2

[1]The reader is encouraged to refer to [21], specifically section 9.3 "The Optical Molasses Technique" and the sub-section 9.3.1 "The Doppler cooling limit" for more detailed discussions of Doppler cooling theory.

(F=1/2, $m_F$=-1/2) within the $2\,^2S_{1/2}$ ground level, s-wave scattering is then permitted, and is the dominating component in the partial-wave expansion in low temperatures. The s-wave scattering length for these collisions between $^6$Li atoms in State 1 and State 2 for different magnetic fields is plotted in Figure 2.3. Note that at zero field, the s-wave scattering length is nearly zero, which means that turning off the magnetic field effectively turns off any interactions. In addition, note the divergence of the scattering length at around 832G, resulting from the Magnetic Feshbach Resonances (MFRs) where a bound state is formed in an energetically closed collision channel, enabling the creation of $^6Li_2$ dimer molecules under the right conditions. This MFR enables nearly arbitrary tuning of the interactions in such spin mixtures, from repulsive (positive scattering length) to attractive (negative scattering length), and spanning a wide range of interaction strengths.

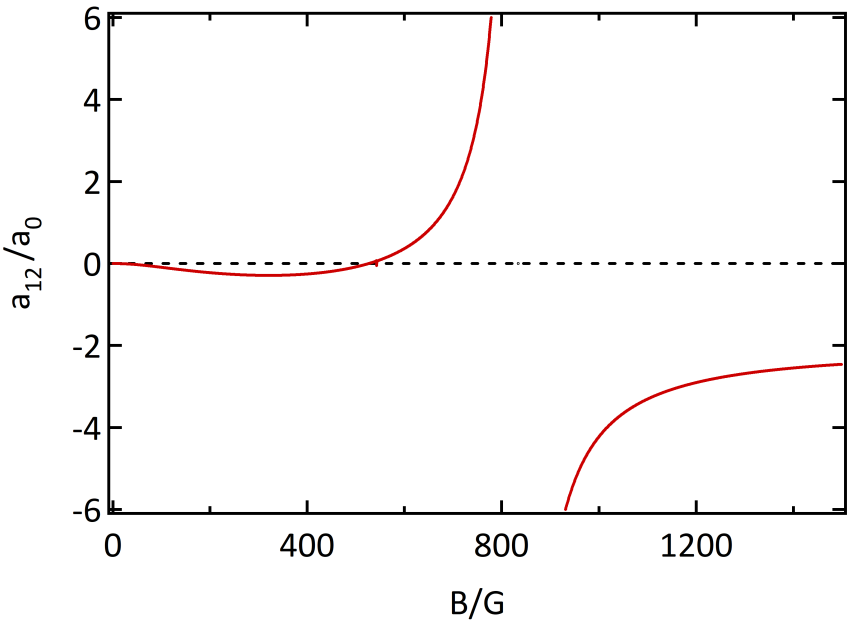


Figure 2.3: s-wave scattering length between State 1 and State 2 $^6$Li atoms at different magnetifc field B.

### *2.1.4 Role in Many-Body Fermionic Systems*

$^6$Li plays a crucial role in the study of many-body fermionic systems. Its properties, such as its scattering length and single-electron structure, make it an ideal candidate for the creation of ultracold Fermi gases. These gases can be used to simulate and study a variety of many-body phenomena, including superfluidity and the BEC-BCS crossover [27, 46].

The physics of quantum degenerate atomic Fermi gases in uniform as well as in harmonically trapped configurations has been reviewed extensively from a theoretical perspective [27]. Emphasis is given to the effect of interactions that play a crucial role, bringing the gas into a superfluid phase at low temperature.

Experimental and theoretical studies concerning many-body phenomena in dilute, ultracold gases has focused on effects beyond standard weak-coupling descriptions, such as the Mott-Hubbard transition in optical lattices, strongly interacting gases in one and two dimensions, or lowest-Landau-level physics in quasi-two-dimensional gases in fast rotation [27].

Moreover, the study of superfluidity and the BEC-BCS crossover in ultracold Fermi gases has been a subject of significant interest [46]. The ability to tune interactions in such spin mixtures, from repulsive to attractive, and spanning a wide range of interaction strengths, has opened up new possibilities for creating $^6$Li molecules under the right conditions and studying their properties.

In conclusion, $^6$Li has proven to be a powerful tool in the study of many-body fermionic systems, providing insights into a range of phenomena that are central to our understanding of quantum mechanics, condensed matter physics, nuclear physics, astrophysics and beyond.

## ***2.2 Mean-Field Theory of Many-Body fermionic Dynamics***

In this section [27, 46], we delve into the mean-field theory, a robust theoretical framework that is frequently employed to elucidate the behavior of interacting quantum gases. We begin with an overview of the Thomas-Fermi profile, a cornerstone concept in the context of the Gross-Pitaevskii equation (GPE). The GPE provides an accurate description of the dynamics of weakly interacting Bose-Einstein condensates (BECs), including the molecular

BEC (mBEC) formed by tightly-bound dimers of $^6Li_2$.

We then transition to the topic of fermionic superfluidity. When a spin mixture of fermions is cooled to quantum degeneracy, the nature of their interactions dictates the resulting state. They could either form tightly-bound bosonic molecules, resulting in a molecular BEC, or a Bardeen-Cooper-Schrieffer (BCS) superfluid of loosely bound pairs. We will discuss the fundamental principles of such fermion pairing, and the mean-field theories that describe these systems.

With the knowledge of Feshbach resonance and the tunability of s-wave scattering between $^6$Li atoms, it is possible to produce a BEC-BCS crossover condensate. We will discuss the evolution of properties during such a crossover, which provides a unique bridge between these two regimes.

However, it is important to note that the mean-field theory has its limitations, particularly when strong interactions come into play in fermionic systems. The mean-field approximation, which assumes that each particle moves independently in an average potential created by all other particles, begins to falter under the weight of strong interactions. This necessitates the exploration of alternative theoretical approaches that can accurately capture the complex dynamics of strongly interacting many-body fermionic systems. We will review these alternative approaches in the literature and discuss their implications for our understanding of quantum phenomena. This exploration of the theoretical landscape is complemented by experimental investigations, which continue to shed light on our understanding of quantum matter.

### *2.2.1 Molecular BEC and GPE*

When the interaction potential between $^6$Li atoms in State 1 and State 2 provides an accessible bound state, it will enable the formation of tightly-bound dimers. These bosonic molecules can form a Bose-Einstein Condensate (BEC) phase in the system when their de Broglie wavelength is longer than the mean free path $l = n^{-1/3}$, where $n$ is the number density of dimers.

*Gross-Pitaevskii Equation (GPE)*

The Gross-Pitaevskii equation (GPE) is a non-linear Schrödinger equation that describes the wave function of a BEC at absolute zero temperature. It is given by:

$$\left(-\frac{\hbar^2}{2m}\frac{\partial^2}{\partial \mathbf{r}^2} + V(\mathbf{r}) + gn(\mathbf{r})\right)\psi(\mathbf{r}) = \mu\psi(\mathbf{r}) \tag{2.3}$$

Here, the parameters are defined as follows:

1. $\hbar$: Reduced Planck's constant.
2. $m$: Mass of the particle.
3. $V(\mathbf{r})$: External potential energy.
4. $g$: Coupling constant, given by $g = (4\pi\hbar^2 a_s/m)$.
5. $a_s$: s-wave scattering length, a measure of the strength of the interaction between particles.
6. $n(\mathbf{r})$: Local number density, non-linear in the wavefunction $\psi(\mathbf{r})$.
7. $\mu$: Chemical potential, a measure of the energy needed to add a particle to the system.

Compared to the typical linear Schrödinger equation, the GPE has an additional mean-field interaction term $gn(\mathbf{r})$, which is non-linear in the wavefunction $\psi(\mathbf{r})$.

*Healing Length*

In discussions about the spatial variations of an atomic trap, the healing length $\xi$ in a BEC is a characteristic length scale that describes how quickly the wave function of the BEC can adjust to changes in the potential. It can be calculated by:

$$\xi = (8\pi n a_s)^{-1/2} \tag{2.4}$$

*Thomas-Fermi Approximation*

In many experimental conditions, the BEC is confined in a harmonic trap, with its harmonic oscillator (characteristic) length $a_{ho} = [\hbar/(m\omega_{ho})]^{1/2}$, where $\omega_{ho}$ is the trap frequency. In the thermodynamic limit when $Na_s/a_{ho} >> 1$, the quantum pressure from the kinetic term in GPE (the first term on the left hand side of Equation 2.3) becomes much less significant than the interaction energy, enabling the Thomas-Fermi approximation. This approximation leads to the Thomas-Fermi profile for the number density:

$$n(\mathbf{r}) = g^{-1}[\mu - V(\mathbf{r})] \tag{2.5}$$

For harmonic traps, this profile has the form of an inverted parabola, and for isotropic traps, this defines a Thomas-Fermi radius $R = a_{ho}(15Na_s/a_{ho})^{1/5}$ for the size of the atomic cloud.

### *2.2.2 Fermion pairing in mean-field theory*

Fermions, unlike bosons, obey the Pauli exclusion principle, which states that no two fermions can occupy the same quantum state simultaneously. This principle leads to fundamentally different behavior in fermionic systems compared to their bosonic counterparts. For example, the degenerate temperature (Fermi temperature) for electrons in a typical metal can easily reach several ten-thousand Kelvins, and yet no superfluid condensate could form until a much lower temperature (several Kelvins) is reached. Indeed, for fermionic systems to form superfluid condensates, fermions in different spin states need to form pairs, and the critical temperature required is proportional to the pair binding energy [46].

Currently, the most widely accepted microscopic theory of superconductivity is the Bardeen-Cooper-Schrieffer (BCS) theory of electron pairing. The framework of BCS theory is based on the fact that when two spin-1/2 fermions are on top of a completely filled Fermi sea in 3D, they only have access to energy states above the level of the Fermi sea. In quantum mechanics, the Fermi sea refers to the collection of all occupied electron energy states up to the Fermi level at absolute zero temperature. It is called a "sea" because it represents a vast, nearly continuous range of energy states that are filled with electrons.

Due to Pauli blocking, which prevents identical fermions from occupying the same quantum state, the fermions above the Fermi sea can only access higher energy states. This effectively changes the density of states in this Cooper problem, resulting in fermion pairing and bounded states even for arbitrarily weak attractive potential between identical fermions, a phenomenon known as Cooper instability. When the same consideration is applied to the fermions inside the Fermi sea, a self-consistent theory of the unstable Fermi sea forming Cooper pairs and hence transitioning into a superfluid was achieved by Bardeen, Cooper, and Schrieffer (BCS) in 1957 [8].

The BCS theory, despite being a mean-field two-body theory describing many-body phenomena, provides a successful description of low-temperature superconductivity near absolute zero. It explains how the formation of Cooper pairs leads to a phase transition to a new superconducting state, where electrical resistance vanishes. The BCS theory also predicts the existence of an energy gap in the density of states of a superconductor, which has been confirmed experimentally.

However, it's important to note that the BCS theory assumes weak attractive interactions and does not fully capture the physics of systems with strong interactions. In addition, it does not apply near the critical temperature where thermal fluctuations become significant.

The Ginzburg-Landau theory, a phenomenological theory developed in 1950, provides macroscopic descriptions of Type-I superconductors in terms of an order parameter that characterizes the phase transition from a normal state to a superconducting state. It is especially useful to describe the behavior near the superconducting phase transition, but is still within the framework of mean-field theory, and fails to describe strongly correlated fermionic systems like many Type-II superconductors and high-temperature superconductors.

In summary, the condensation of fermions into superfluids is intrinsically a many-body phenomenon; non-interacting fermions cannot form superfluids. The many-body physics involved in Cooper pairing is primarily due to the modification of the density of states due to Pauli blocking, rather than the modification of interactions. This understanding of Cooper pairing is a key aspect of the BCS theory of superconductivity, which applies to

Fermi superfluids near absolute zero. For fermions near the superfluid phase transition, the Ginzburg-Landau theory can be used to describe the phenomenological behavior of the order parameter. However, both of these theories still categorize as mean-field theories, and fail to capture the behavior of strongly interacting fermionic systems.

### *2.2.3 BEC-BCS Crossover in Ultracold Fermi Gases*

The tunability of the s-wave scattering length $a_s$ via a magnetic field in the Feshbach resonance between $^6$Li atoms in State 1 and State 2 enables the preparation of a superfluid condensate that exhibits a crossover from a Bose-Einstein Condensate (BEC) state to a Bardeen-Cooper-Schrieffer (BCS) state [46].

Throughout this BEC-BCS crossover, all physical quantities evolve smoothly, with many of them changing monotonically with the interaction strength parameter $1/(k_F a_s)$, where $k_F$ is the Fermi wave vector. However, several qualitative shifts occur during this crossover, each associated with a specific value of $1/(k_F a_s)$. These shifts include changes in the excitation spectrum, critical velocity, normal density, pair size, and the equation of state exponent.

The first Fermi degenerate condensates [10] created in the field of ultracold atoms experiments already realized crossover condensates consisting of large, extended molecules or fermion pairs, which is a significant milestone that bridges two previously separate regimes. This crossover regime is particularly intriguing as it represents a state where bosonic and fermionic descriptions merge or coexist, providing a unique platform for studying many-body quantum phenomena.

### *2.2.4 Beyond Mean-Field Theory: Fermi-Liquid Theory and Unitary Fermi Gas*

As mentioned before, the mean-field approximation, while a powerful tool for understanding many-body quantum systems, begins to falter when strong interactions come into play, particularly in the realm of fermionic systems; as such, alternative theories have been studied to shed light on such systems.

One of the key theoretical frameworks that extends beyond the mean-field approximation

is Landau's Fermi-liquid theory. This theory provides a description of strongly interacting fermions at low temperatures, where the system behaves similarly to a non-interacting Fermi gas, but with renormalized parameters. The quasiparticles in this theory carry the same spin and charge as the original particles, but their mass, known as the effective mass, is renormalized due to interactions. Fermi-liquid theory has been successful in explaining the properties of electrons in metals and has been instrumental in our understanding of strongly correlated fermionic systems.

Another important concept in the study of strongly interacting Fermi gases is the Unitary Fermi Gas (UFG). This refers to a system of fermions interacting via a zero-range potential, where the s-wave scattering length diverges ($a_s \to \infty$), and the system resides at the so-called unitarity limit. UFG is of particular interest to various fields, including nuclear physics and astrophysics, because it represents a maximally interacting system, and yet, some properties can still be calculated exactly. For instance, the energy of UFG is known to be a universal constant times the energy of an ideal Fermi gas. Furthermore, UFG exhibits a high value of the superfluid critical temperature, making it a fascinating system for the study of superfluidity in strongly interacting fermionic systems.

In summary, while the mean-field theory provides a useful starting point for understanding many-body quantum systems, it is the exploration of theories beyond mean-field, such as Fermi-liquid theory and the study of unitary Fermi gases, that truly opens up the rich and complex world of strongly interacting fermionic systems. These theoretical frameworks not only provide deeper insights into the fundamental properties of quantum matter but also open up exciting possibilities for the discovery of novel quantum phases and phenomena. The study of strongly interacting fermions, therefore, remains a vibrant and fruitful field of research in quantum physics.

### *2.3 Experimental Apparatus and its Dual-Species Capabilities*

Our experimental apparatus, designed for the study of ultracold Ytterbium (Yb) and Lithium (Li) atoms, is a unique setup that allows for dual-species operations [33, 47]. The experiments are conducted in an ultra-high vacuum chamber, ensuring a longer lifetime for the atoms in the trap by minimizing collisions with residual background molecules inside

the vacuum chamber.

The apparatus includes separate ovens for Yb and Li, which are heated to produce corresponding atomic vapors. The vapors are then laser cooled and slowed using a Zeeman slower approach, which employs a resonant laser beam and a spatially varying magnetic field. The cooled atoms are captured and further cooled in a magneto-optic trap (MOT), which uses laser cooling and a magnetic field gradient to reduce the temperature and increase the density of the atomic sample.

After the MOT stage, the Yb atoms are sufficiently cooled to be captured by our optical dipole trap (ODT) for further cooling. The Li atoms, with a higher Doppler limit in optical molasses cooling, has a higher temperature in the MOT than Yb, due to a larger natural linewidth. As a result, the efficiency of loading Li atoms into the ODT is significantly lower than Yb. Techniques such as sub-Doppler cooling with the D1 transition can be applied to lower Li atoms' temperature to improve ODT loading, a topic we will delve into in the subsequent chapter.

The ODT operates by using a far-detuned laser light to generate a conservative potential, effectively trapping the atoms. To further reduce the temperature, we employ forced evaporative cooling within the ODT, which, although it results in a decrease in the number of trapped atoms, significantly lowers the temperature and raises the Phase Space Density (PSD). When Yb atoms are present in the same ODT, Li atoms can benefit from a process known as sympathetic cooling resulting from interspecies elastic collisions.

Finally, we probe the trapped atoms using absorption imaging, which uses the absorption of a resonant imaging light by the atomic cloud to quantify the atomic density distribution in space and the number of atoms in the relevant quantum state. We will delve into the details of absorption imaging in subsequent chapters.

In 2019, we adapted the apparatus for a YbLi Magnetic Feshbach Resonance experiment [29]. I contributed to many operational tasks, including optical setup and alignment, fiber coupling, data taking, and data processing. I also contributed to the design of spin polarization and state detection of our Yb atoms, separating and manipulating the quantum spin states of these ultracold atoms at around $1\mu$K using optical pumping and Optical Stern-Gerlach methods.

From Fall 2019 to Spring 2022, we configured the apparatus for the integration of optical lattice laser beams in all three dimensions and single-species operations involving only Yb, specifically the bosonic isotope $^{174}$Yb. We focused on the quantum transport of $^{174}$Yb atoms in one-dimensional (1D) tubes, with Quantum Kicked Rotor Hamiltonian. Our observations led to the discovery of Many-body dynamical delocalization in 1D kicked quantum gases [76] and evidence supporting the existence of a Many-Body Anderson Metal-Insulator Transition [80]. In these experiments, my contributions encompassed generating pulses, setting up the optical system, collecting and analyzing data, and visualizing the data for the final manuscript.

In summary, our dual-species apparatus provides a robust platform for studying the complex dynamics of ultracold atoms, offering unique capabilities for exploring many-body quantum phenomena. It has proven to be a valuable tool in our research, enabling us to make contributions to the field of experimental ultracold atomic physics.

### *2.4 AC Stark Shift and Far-Off-Resonance Light Fields*

The AC Stark Shift, also known as the Autler-Townes effect, is a fundamental phenomenon that forms the basis for several techniques employed in our atomic physics experiment. These techniques include the optical dipole trap, optical lattice, and pulsed standing wave kicks. The AC Stark Shift arises from the interaction between an atom and an oscillating electric field, such as that produced by a laser beam. To minimize the scattering rate and associated heating from the light field, the laser frequency $\omega$ is tuned to be far-off-resonance from the atomic transition frequency $\omega_0$, and the intensity of the light field is strong to create sufficient optical force. This means, the detuning $\Delta = \omega - \omega_0$, the natural linewidth $\Gamma$ of the atomic transition, the light intensity $I$ and that saturation intensity $I_{sat}$ satisfies $|\Delta|/\Gamma \gg I/I_{sat} \gg 1$.

When an atom is exposed to an oscillating electric field, the field induces a dipole moment within the atom. This induced dipole moment then interacts with the electric field, leading to a shift in the atom's energy levels. This energy shift, known as the AC Stark Shift, is a direct result of the atom's response to the external field. The magnitude and direction of this shift are dependent on several factors; quantitatively, in general, we have the dipole potential

$U(\mathbf{r}) = -\alpha(\lambda_L)I(\mathbf{r})/(2\varepsilon_0 c)$, where $\alpha(\lambda_L)$ is the real part of the atomic polarizability at the laser wavelength $\lambda_L$ [31]. For $|\Delta|/\Gamma \gg I/I_{sat} \gg 1$, the potential energy experienced by an atom at location $\mathbf{r}$ is $U(\mathbf{r}) = -(\frac{\hbar\Gamma^2/8}{\omega_0-\omega} + \frac{\hbar\Gamma^2/8}{\omega_0+\omega})[I(\mathbf{r})/I_{sat}]$. For the case where $|\Delta| \ll \omega_0 + \omega$, Rotating Wave Approximation applies, and therefore $U(\mathbf{r}) = \frac{\hbar\Gamma^2}{8\Delta}[I(\mathbf{r})/I_{sat}]$.

In applications that utilize the optical dipole force, it is common practice to use a far-off-resonance light frequency. This is because a smaller detuning would increase the photon-atom scattering rate much faster than it increases the dipole potential energy, leading to undesirable heating of the atoms. As detailed in [31], for $|\Delta|/\Gamma \gg I/I_{sat} \gg 1$, the scattering rate is given by $R_{sc}(\mathbf{r}) = (\omega/\omega_0)^3|(\frac{\Gamma}{\omega_0-\omega} + \frac{\Gamma}{\omega_0+\omega})\frac{U(\mathbf{r})}{\hbar}|$. Again, for the case where $|\Delta| \ll \omega_0 + \omega$, Rotating Wave Approximation applies, and therefore $R_{sc}(\mathbf{r}) = |\frac{U(\mathbf{r})}{\hbar\Delta/\Gamma}|$. However, this Rotating Wave Approximation is not applicable for large detunings such as our Optical Dipole Trap (ODT) beam at 1064nm, when the atomic transitions addressed are 671nm for Li and 556nm and 399nm for Yb.

Furthermore, the behavior of the atoms in the light field can be manipulated by adjusting the detuning. If the light frequency is lower than the resonant atomic transition frequency, a configuration known as "red detuning," the atoms will be drawn to regions of higher light intensity in an attempt to minimize their potential energy. Conversely, if the light frequency is higher than the resonant atomic transition frequency, a configuration referred to as "blue detuning," the atoms will seek out regions of lower light intensity to minimize their potential energy. This ability to control the spatial distribution of atoms using detuning is a powerful tool in atomic physics experiments, specifically for designing confinements (traps, lattices) and inducing dynamics.

It is also worth mentioning the recoil energy $E_{rec} = \hbar^2k^2/(2m)$, which is the kinetic energy imparted in an atom initially at rest by "recoil" during the spontaneous emission of a photon. Correspondingly, the recoil frequency is defined as $\omega_{rec} = \hbar k^2/(2m)$. Here, $k = 2\pi/\lambda$ is the wave vector of the light field, and $m$ is the mass of the atom. The recoil energy and frequency are crucial parameters in understanding the dynamics of atoms in light fields, especially in the context of atom optics and momentum transfer.

### *2.4.1 Optical Dipole Trap*

In the context of an Optical Dipole Trap (ODT), the AC Stark Shift is harnessed to trap and cool atoms. A tightly focused laser beam in Gaussian spatial mode ($\text{TEM}_{00}$), far red-detuned from the atomic resonance, creates an intensity gradient that leads to a spatially dependent AC Stark Shift. Atoms are drawn to the regions of highest intensity, effectively trapping them in the focus of the laser beam. The detuning of the laser ensures that the atoms are not excited to higher energy states, allowing for the trapping of atoms without causing significant heating, and the high intensity ensures sufficient trap depth to capture the atoms. This technique is a cornerstone of our experimental setup, enabling us to confine and manipulate the $^6$Li atoms, and apply evaporative cooling to reach quantum degeneracy or even superfluidity.

For our linearly polzrized ODT beam at 1064nm, the red detuning from both the D1 and D2 transition is about $\Delta = 2\pi\times165.0\text{THz}$ with a natural linewidth $\Gamma = 2\pi\times5.8724\text{MHz}$; in this case, the fine structure splitting between D1 and D2 line can be ignored, and $I_{sat} = 2.54\text{mW/cm}^2$ is used [31]. This dipole potential $U(\mathbf{r}) = -\alpha(\lambda_L)I(\mathbf{r})/(2\varepsilon_0 c) = -(\frac{\hbar\Gamma^2/8}{\omega_0-\omega} + \frac{\hbar\Gamma^2/8}{\omega_0+\omega})[I(\mathbf{r})/I_{sat}]$ can be calculated, and the resulting coefficient is $\alpha(\lambda_L = 1064\text{nm})/(2\varepsilon_0 c) = 8.36\times10^{-37}\text{m}^2\text{s}$, consistent with Equation (4.1) of [69].

The waist of our ODT beam at its focus is estimated to be $w_0 = 30\mu\text{m}$ [69, 79], and with a typical power of P=50W, the peak intensity is estimated to be $I_0 = 2P/(\pi w_0^2) = 3.54\times10^{10}\text{W/m}^2$. Our ODT beam therefore provides a trap depth of about $k_B\times2.15\text{mK}$.

### *2.4.2 Optical Lattice*

Similarly, the AC Stark Shift is the underlying principle behind the creation of an Optical Lattice. In this case, two identical counter-propagating laser beams (or a laser beam and its own reflection) interfere to create a standing wave of light. The intensity of the light varies periodically in space, and the frequency of the light is far red detuned from the atomic transitions, creating a lattice of potential wells where atoms can be trapped. With a standing wave providing lattice confinement in one dimension, we will have 2D "pancakes" of atomic clouds; with two standing waves providing lattice confinement in two orthogonal

dimensions, we will have 1D "tubes" of atomic clouds; with three standing wave providing lattice confinement in all three orthogonal dimensions, we will have points of atomic clouds at each lattice site, which is the usual configuration for optical lattices. [79] provides more details about such geometry and calculation of the lattice potentials.

This optical lattice serves as a versatile tool for studying many-body fermionic dynamics, as it allows for precise control over the atomic motion, number density, and interactions.

### *2.4.3 Pulsed Standing Wave Kicks*

The AC Stark Shift plays a crucial role in the Pulsed Standing Wave Kicks technique. This method uses a temporally modulated standing light wave, with a lattice depth of $V_{lat}$, to impart momentum to atoms. The AC Stark Shift not only creates a spatially periodic potential, but this potential is also periodically "flashed" on for a pulse duration $t_p$, and off during the pulse's downtime.

When a Bose-Einstein Condensate (BEC) interacts with the diffraction grating formed by a standing light wave, two scenarios can occur. In Bragg diffraction, the light resonantly couples the different momentum states, enabling the atoms to oscillate between these states. However, if the different momenta are not resonantly coupled, Kapitza-Dirac diffraction can still occur if the interaction time is sufficiently short. This situation, first proposed by Paul Dirac and Pytor Kapitsa in 1933, falls under the Raman-Nath approximation, where the atomic motion during the brief interaction time is negligible compared to the wavelength of the standing light wave. This requires that $t_p$ be much less than the inverse of recoil frequency ($1/\omega_{rec}$). For $^6$Li and 671nm light, this means $t_p \ll \omega_{rec}^{-1} = 2.15\mu$s[2].

In the context of our $^{174}$Yb experiment [79], the Kapitza-Dirac (KD) diffraction governs the transfer of probability amplitudes of the atoms to different momentum lattice sites during each kick of the Quantum Kicked Rotor (QKR). This is part of the broader field of atom optics, where an ultracold atom cloud is treated similarly to an optical beam, reversing the roles of light and matter. The phase coherence of ultracold quantum degenerate gases allows us to treat it as a coherent optical beam, with atoms often coherently manipulated

[2]Here, $\omega_{rec}$ is an angular frequency in units of radians per second, and not an ordinary frequency in units of Hz. However, when the condition $t_p \ll \omega_{rec}^{-1}$ is satisfied, the condition $t_p \ll (\omega_{rec}/2\pi)^{-1}$ is also satisfied.

with a standing light wave acting as matter.

The final state of the atoms is a superposition of different multiples of $2\hbar k_L$ momentum states, where $k_L$ is the wave number of the standing light wave. The probability of the atoms populating the $2n\hbar k_L$ state after the diffraction is given by $[J_n(\phi_{kick})]^2$, where $J_n$ is the nth order Bessel function and $\phi_{kick} = V_{lat}t_p/(2\hbar)$ is the pulse area. This was the method we used to calibrate the potential depth of our kicking lattice beam.

By carefully controlling the timing and intensity of the light pulses, we can manipulate the motion of the atoms. This technique provides a powerful means of inducing and probing the dynamics of the $^{174}$Yb atoms in our experiment. The atom optics kicked rotor for fermionic $^6$Li in a superfluid state presents a richer variety of physics, which will be the primary topic for Chapter 4 of this thesis.

In conclusion, the AC Stark Shift is a fundamental effect that allows for the manipulation and control of atomic motion in various experimental techniques. Gaining a comprehensive understanding and control of this effect is essential for the effective execution of these techniques in our experiment.

This chapter has explored the properties of $^6$Li, the mean-field theory, the capabilities of our experimental apparatus, and the optical dipole force that underpins various technologies in our atomic physics experiment. This foundational knowledge sets the stage for the subsequent chapters. With this understanding, we are now prepared to delve into our experimental findings and theoretical analyses, which will provide insights into the world of laser cooling and trapping of $^6$Li.

# Chapter 3

# EXPERIMENTAL TOOLS FOR MANY-BODY FERMIONIC DYNAMICS

From Fall 2019 to Spring 2022, our experimental apparatus was primarily employed for the study of many-body quantum dynamics of bosons with $^{174}$Yb single-species operation [76, 80], following its use in YbLi magnetic Feshbach resonance research [29].

In August 2021, as we were finalizing the data analysis of our Yb 1D Quantum Kicked Rotor experiment and the manuscript for our "Many-body Dynamical Delocalization in a Kicked One-dimensional Ultracold Gas", I had the opportunity to breathe new life into the Li setup in anticipation of future experiments with $^6$Li fermions. Within a month, I successfully updated the Li Zeeman slower laser diode (OpNext diode) and its injection lock, revitalized the optical alignment of various Acousto-Optical Modulators, optical fibers and other setups, and restored the Saturated Absorption Spectroscopy for frequency-stabilization of the laser sources. Despite these advancements, the Li MOT presented a complex challenge that required more time and resources than initially anticipated. Recognizing the potential of the continued research on Yb experiment, we decided to prioritize it and revisit the Li experiment at a later date.

In June 2022, after we completed the data collection for the "Many-Body Anderson Metal-Insulator Transition using Kicked Quantum Gases" experiment, we committed to a journey to revitalize and enhance the $^6$Li cooling setup for single-species operation and reaching $^6$Li Fermi condensate. Our immediate objective was to study many-body quantum transport using the quantum kicked rotor Hamiltonian for paired $^6$Li fermions, facilitated by pulsed kicking standing waves. This chapter delves into the modifications and improvements made to our apparatus to facilitate these experiments.

The forthcoming sections will detail the process of laser cooling and trapping of $^6$Li to achieve sub-Doppler temperatures. We will then discuss the procedure of loading $^6$Li

atoms into an optical dipole trap, preparing a spin mixture of these atoms, and executing evaporative cooling to attain quantum degeneracy. Subsequently, we will discuss the active stabilization of the large bias magnetic field, a crucial step for accessing narrow Feshbach resonances. Lastly, we will present our design of short pulses, a key component in inducing dynamics in paired $^6$Li fermions.

### *3.1 Laser cooling and trapping of $^6$Li*

The experimental setup for our system begins with metallic Li samples housed in a vertically oriented cup, heated to 400 degrees Celsius. The atomic vapor navigates a rounded L-shaped section, passing through a nozzle and a differential pumping tube, which maintains a differential pressure between sections. This path leads the atoms into our Zeeman slower, where they are slowed down by a red-detuned laser beam (consistent with Doppler cooling theory[1]), and a spatially-varying magnetic field Zeeman shifts the resonant frequency of the atoms to match the decreasing Doppler shift as they are slowed down to lower velocities. After the nozzle, only a small fraction of atoms makes it through the thin, long Zeeman slower to the main chamber to reach the Magneto-Optical Trap (MOT), and this fraction has nearly zero transverse velocities due to the thin, long geometry of the Zeeman slower. As previously mentioned, the Zeeman slower reduces the longitudinal velocities using a red-detuned laser beam and a spatially-varying magnetic field, which means that the fraction of atoms reaching the MOT has low velocities in every direction, allowing for capture by the MOT.

Within the Zeeman slower, the Li atoms undergo continuous Doppler cooling as they interact with photons from our Li slower laser and its sidebands for repumping. The fraction of atoms exiting the slower and reaching the MOT can then be captured, as long as they are sufficiently slow in velocities. The MOT setup comprises a magnetic gradient field, several small bias fields to compensate for stray magnetic fields and the geomagnetic field, and three pairs of MOT cooling light and repump light.

After loading the Li atoms into our MOT, we perform MOT compression, which lasts

[1]The reader is encouraged to refer to [21] section 9.3 “The Optical Molasses Technique” for a more detailed discussion of Doppler cooling theory.

about 40ms. This is achieved by adiabatically reducing the red-detuning of our MOT laser frequencies and simultaneously diminishing the intensities of our MOT and repump light to nearly zero, while also increasing the magnetic field gradient in the MOT (the numerical values of this gradient field is discussed in the subsequent section for MOT compression). This process must be much slower than $\omega_{rec}^{-1} = 2.15\mu$s and $\Gamma^{-1} = 27.1$ns, and allows us to reach a temperature of approximately $400\mu$K, while also increasing the number density of the atoms by achieving a smaller atomic cloud.

To quantify the number of atoms captured at the end of each run of our experimental sequence, we employ absorption imaging light at the resonance frequency of atomic transitions. A CCD camera (Andor iXon3) is used to capture a triplet of images of the optical intensity distributions: the first one with the imaging light and the atomic cloud $I_1(x, y)$, the second one with the imaging light but no atomic cloud (a relaxation timestep is used for the atoms to dissipate away) $I_2(x, y)$, and the third one without the imaging light to capture any background light $I_b(x, y)$. Based on the principles of Beer-Lambert Law, the atom number column density (also known as area number density, the number of particles per unit area in the image) will be proportional to $\ln \frac{I_2(x,y)-I_b(x,y)}{I_1(x,y)-I_b(x,y)}$. The total atom number and the height/width of the atomic cloud are subsequently extracted from the spatial distribution based on numerical fits of the accumulated atomic density in the vertical/horizontal profile.

Due to the narrow linewidths of the atomic transitions, the successful execution of the aforementioned sequence necessitates the use of narrow linewidth laser sources with adequate power. Additionally, we must be able to shift the frequencies of the light to address different transitions with varying detunings for diverse purposes. Furthermore, we require precise control over these parameters, including the individual laser beams' on/off switch, laser frequencies and amplitudes, and the magnetic field's on/off switch and amplitude, with $\mu$s accuracy.

Finally, frequency stabilization of the laser sources is a critical aspect of our setup, as it prevents frequency drifts over time. The features described above are visually represented in the optical layout diagram provided in Figure 3.1.

In Figure 3.1, several Acousto-Optical Modulators (AOMs) are employed for the pur-

poses mentioned earlier. These AOMs are instrumental in shifting the laser beams' frequencies, controlling their powers, and rapidly switching them on and off (sub-microseconds) during an experimental sequence run. The typical values for these AOM frequencies are as follows:

1. MOT AOM: 65.2MHz at MOT loading step, 79.2MHz at MOT compression endpoint;

2. Repump AOM: 189.3MHz at MOT loading step, 192.3MHz at MOT compression endpoint;

3. Slower light: injection seed AOM at 276MHz (sideband RF modulation at 229MHz);

4. Saturated Absorption Spectroscopy (SAS): AOM centered at 283.7MHz;

5. Imaging AOM: for low magnetic bias field, AOM at 200MHz; high magnetic bias field imaging frequency depends on the Zeeman shift of the transition addressed.

Based on the aforementioned AOM frequencies, we can calculate the optical frequencies of the various laser beams used in our experiment. As discussed in Chapter 2 (Figure 2.1), for $^6$Li, the hyperfine splitting in the $2\,^2P_{3/2}$ level ($2\pi\times$4.4MHz) is smaller than the natural linewidth ($\Gamma = 2\pi\times$5.87MHz) of the D2 transition to the ground level $2\,^2S_{1/2}$. Therefore, in the following discussion, we do not distinguish the hyperfine levels in the excited level $2\,^2P_{3/2}$. We define the transition frequency from $2\,^2S_{1/2}$, F=1/2 to $2\,^2P_{3/2}$ level as $\omega_{D2,F=1/2}$, and the transition frequency from $2\,^2S_{1/2}$, F=3/2 to $2\,^2P_{3/2}$ level as $\omega_{D2,F=3/2} = \omega_{D2,F=1/2} - 2\pi\times$228.2MHz. The following discussion and calculation are based on the technical details described in subsequent sections in this chapter, and a visualization of these laser frequencies can be found in Figure 2.1.

1. SAS lock: For the Saturated Absorption Spectroscopy, the Pump beam undergoes a double-pass through an AOM at 283.7MHz in the +1 order, and we lock our primary laser source to the crossover peak in the D2 line $\omega_{SAS}=\omega_{D2,F=1/2} - 2\pi\times$

114.1MHz=$\omega_{D2,F=3/2} + 2\pi\times$114.1MHz. Therefore, the optical frequency for our primary laser source (master laser) is $\omega_{master} = \omega_{D2,F=1/2} - 2\pi \times 397.8$MHz=$\omega_{D2,F=3/2} - 2\pi \times 169.6$MHz.

2. MOT laser: The MOT laser beams are frequency-shifted from the master laser by a double-pass through an AOM in the +1 order. This results in a red detuning from $\omega_{D2,F=3/2}$ by 6.68$\Gamma$ at the MOT loading step, and 1.91$\Gamma$ at the MOT compression endpoint, where $\Gamma = 2\pi\times$5.87MHz is the natural linewidth of the D2 line.

3. Repump laser: The Repump laser beams are frequency-shifted from the master laser by a double-pass through an AOM in the +1 order. This results in a red detuning from $\omega_{D2,F=1/2}$ by 3.27$\Gamma$ at the MOT loading step, and 2.25$\Gamma$ at the MOT compression endpoint.

4. Slower light: The injection seed laser beam for the slower laser diode is frequency-shifted from the master laser by a double-pass through an AOM in the -1 order. This results in a red detuning from $\omega_{D2,F=3/2}$ by 122.88$\Gamma$, and its blue sideband from the RF modulation at 229MHz has a red detuning from $\omega_{D2,F=1/2}$ by 122.75$\Gamma$.

5. Imaging light: The imaging laser beam for low magnetic bias field is frequency-shifted from the master laser by a double-pass through an AOM in the +1 order. This means that the imaging light is roughly on resonance with $\omega_{D2,F=1/2}$, with a slight blue detuning of 0.37$\Gamma$ or about 2MHz from the atomic transition frequency, which may be a result of ambient or stray magnetic field (e.g. from the nearby ion pumps).

The typical optical power for the MOT laser is about 40mW (measured at the MOT shutter), and for the repump, it is about 10mW. The optical intensities of these laser beams are also measured at their entry point into the vacuum chamber before interacting with the atoms, using a 300$\mu$m diameter precision pinhole (Thorlabs P300K). In terms of $I_{sat}$=2.54 mW/cm$^2$, the Li MOT beams measure to be 8.7$I_{sat}$ and 9.5$I_{sat}$ in the two horizontal axes, and 16.2$I_{sat}$ in the vertical axis; the Li repump beams measure to be 0.78$I_{sat}$ and 0.67$I_{sat}$ in the two horizontal axes, and 3.1$I_{sat}$ in the vertical axis.

The earliest initial version of this setup was constructed by previous PhD students Alex Khramov and Anders Hansen. The typical values, lens focal lengths, and other numerical values in this thesis are current as of Summer 2023, reflecting the ongoing evolution and refinement of our experimental setup.

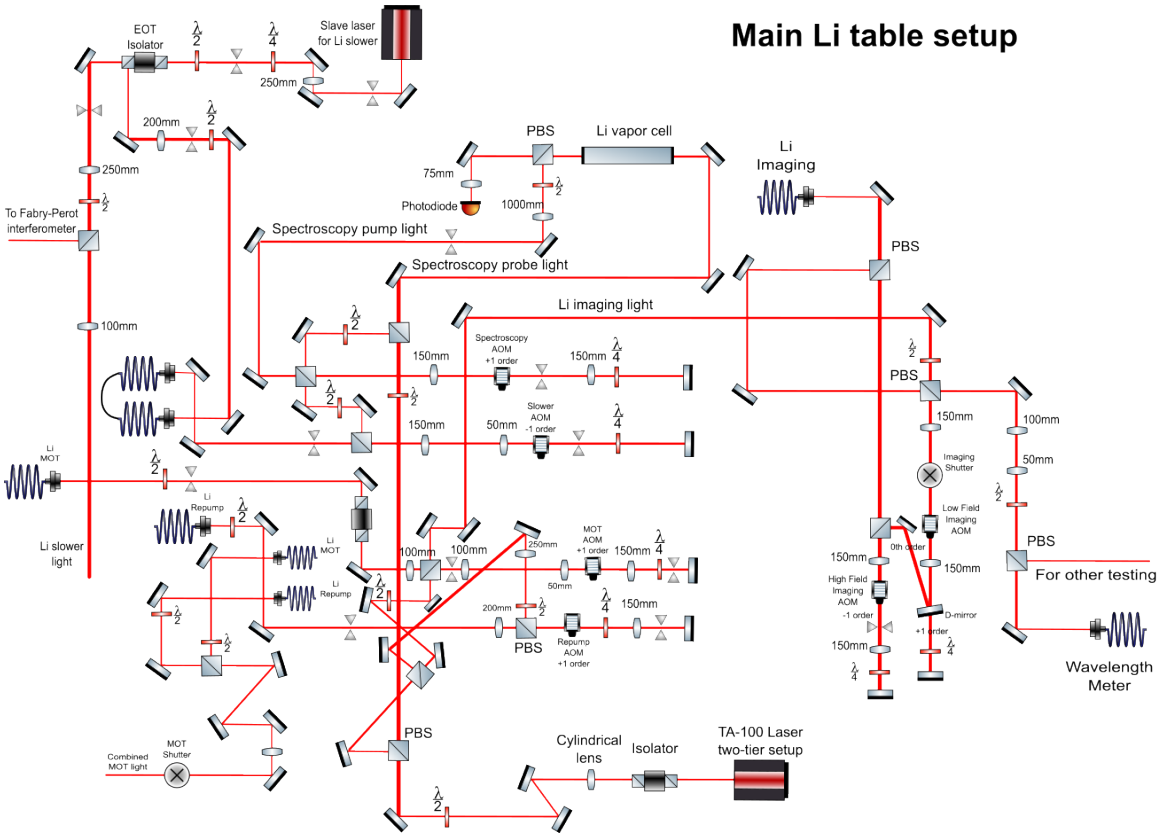


Figure 3.1: Main Li table setup, including Li MOT/repump light, Li Zeeman slower light and saturated absorption spectroscopy setup for main laser (TA-100) frequency stabilization. Diagram created with the ComponentLibrary from gwoptics.

### *3.1.1 Primary laser source*

The primary laser source (main laser) in our Li setup is the Toptica TA-100, an Amplified Tunable Single-mode Laser System. This laser has been a part of our lab for over a decade as of 2022. However, as we made our efforts into revitalizing the Li setup, we found that

the Tapered Amplifier (TA) within the system had degraded beyond repair. Despite our best efforts to realign the seed light from the 671 nm diode inside to the Tapered Amplifier, we were unable to achieve sufficient power output after the TA.

Faced with this challenge, our team turned to innovative problem-solving. Cole Williams and Carson Patterson spearheaded the design of a two-tier optical platform (see Figure 3.2) to maximize the limited space available on our busy optical table. Their ingenious design allowed us to incorporate a home-made Tapered Amplifier beneath the platform. However, the initial design resulted in frequency noises in our primary laser source that couldn't be stabilized by the saturated absorption spectroscopy, which greatly hindered our progress in the experimental setup.

Upon encountering this issue, I took the initiative to troubleshoot the problem and discovered that the mechanical stability of the initial design of the two-tier system was insufficient to decouple the environmental acoustic vibrations (from the optical table and so on) from our main laser's external cavity. After thoughtful discussions with Prof. Gupta and the rest of our team, I collaborated with Carson to procure and modify a brass plate to attach to the platform and provide further stability. The result was a significant improvement, with the new setup yielding 400 mW of optical power (Figure 3.3) and a sufficiently stable frequency lock with the saturated absorption spectroscopy. This creative solution, a product of our team's collective efforts and problem-solving, allowed us to rejuvenate our Li setup and continue our experimental work.

### *3.1.2 Frequency stabilization*

Following the output of the Tapered Amplifier, we employ polarization optics, specifically half-wave plates and polarizing beam splitters (PBS), to distribute and split the primary laser into several distinct paths, each with its own linear polarization, while also passing through a series of components such as spherical lenses, Acousto-Optic Modulators, optical isolators, and more. This constitutes a significant portion of the optical engineering in our experiment. During the time when our apparatus was primarily employed for Yb-only experiments, some of the opto-mechanical parts, such as knobs and screws, had drifted

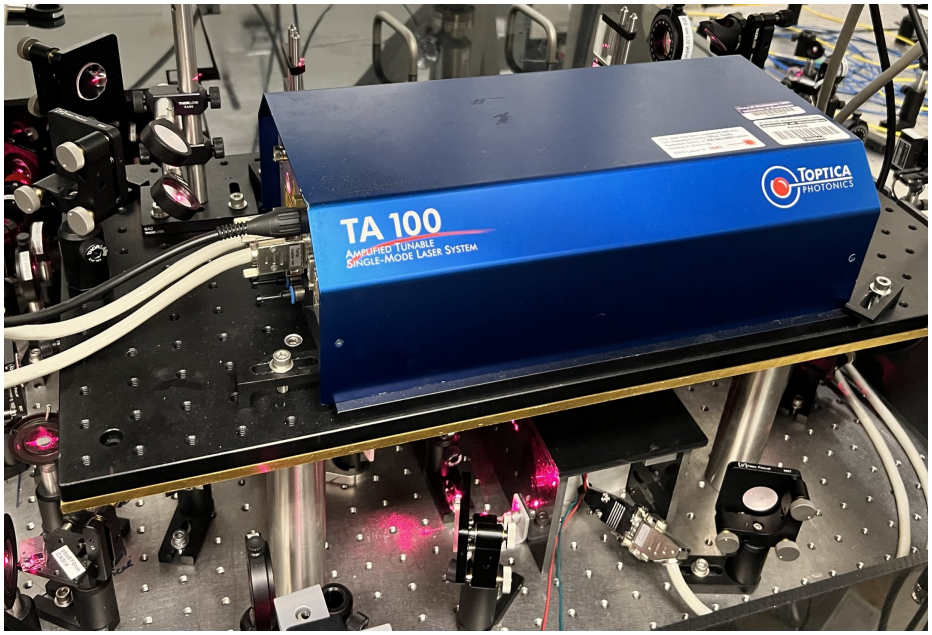


Figure 3.2: The two-tier optical platform for our primary laser source. The master diode is inside the blue enclosure of Toptica TA-100, but the under-performing TA chip inside it is removed. The master diode's light (25mW), after passing through a few optics, is fed into a homebuilt TA mount (black enclosure) underneath the optical platform.

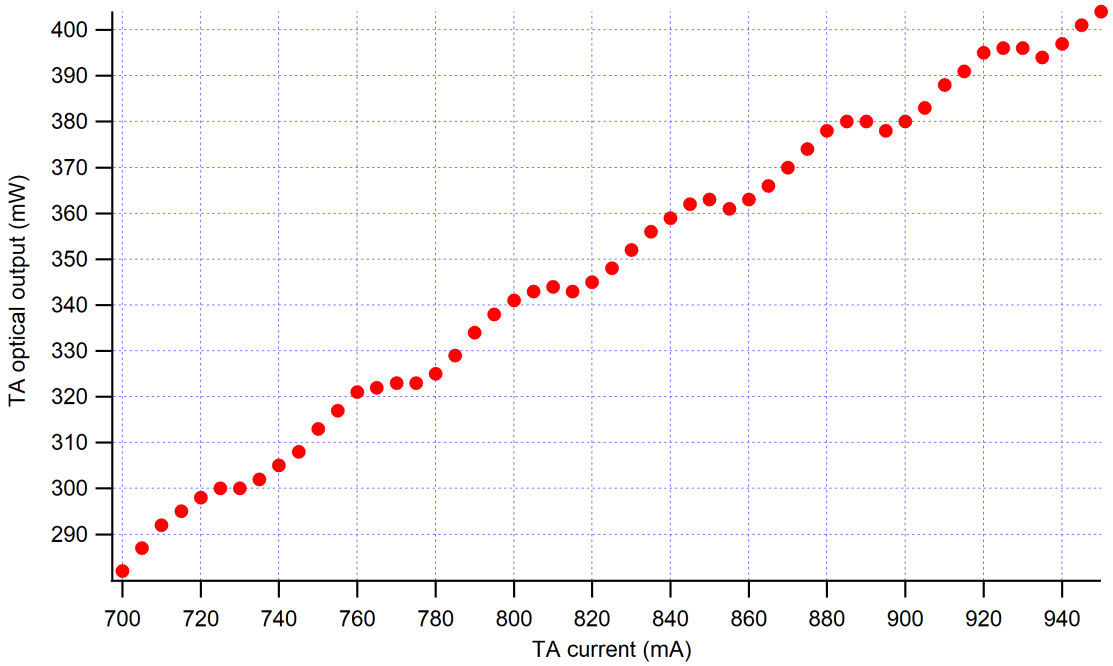


Figure 3.3: TA output power vs TA current in the new 2-tier system. Seed power from TA100 at 25mW.

due to mechanical vibrations and disturbances. The process of realigning and recalibrating these components required careful work and trained skills. With a collaborative effort and attention to detail, we were able to successfully rejuvenate the Li laser table in summer 2022, maintaining the integrity and functionality of the system without undue difficulty.

In the main Li table setup, a portion of the primary laser light is directed towards a saturated absorption spectroscopy setup, which is used to lock the laser frequency. A part of this light serves as the pump beam in the saturated absorption spectroscopy setup, undergoing a double-pass through an Acousto-Optic Modulator (AOM) setup. The light after the double-pass arrangement will have a blueshift twice the RF frequency on the AOM, and this blueshift can be controlled by external analog voltages to control the frequency of the RF signal. With the double-pass configuration, the effect of changing the RF frequency on the Bragg diffraction angle is canceled out between the first pass and the second pass, so the optical alignment downstream can remain steady.

A fraction of the power from the primary laser is utilized as a probe beam in the saturated absorption spectroscopy setup. The pump and the probe beams counterpropagate through a vapor cell of Li, and the transmitted probe beam is continuously measured by a photodiode (see Figure 3.4). We apply a modulation to the pump beam's frequency, and then feed the modulation signal to the reference port of a lock-in amplifier. This allows us to obtain the differential of the photodiode signal of the probe. The percentage of atomic absorption of the probe light (in the absence of the pump light) in Figure 3.4a is approximately 50%, and Figure 3.4b is a zoomed-in version of the same photodiode signal of the probe light in the presence of the pump light. Note that the frequency scans in these spectra follow a triangle waveform, and the same frequency range appear twice between adjacent triggers, resulting in a mirror image of the same spectrum.

In this setup, the principles of saturated absorption spectroscopy [21] are employed. Given the broad range of velocities in the thermal sample, each laser beam interacts only with a narrow class of atoms moving at a specific velocity. A saturation feature, or a local maximum in the photodiode signal of the probe beam, appears when the laser is precisely tuned to the atomic resonance. This causes both beams to interact with the same velocity class - those atoms with zero velocity. This phenomenon occurs as the stronger pump

laser transfers the atoms to another, dark hyperfine state, rendering the sample partially transparent to the probe beam.

Lithium presents a special case of inverted crossover, which distinguishes it from other alkali metals such as Rb, Cs, Na, where the crossover is positive. This distinction arises from the small ground state hyperfine splitting in lithium compared to its Doppler width, leading to an inverted crossover peak between the two hyperfine states [33, 21]. Unlike other alkalis, where the ground state hyperfine splitting is much larger than their Doppler widths, in lithium, both the pump and probe can interact with the two hyperfine levels in $2\,^2S_{1/2}$ within a single velocity class. At the crossover resonance, the interaction with the pump beam increases the population of atoms that interact with the probe, resulting in a negative crossover peak where the pump beam optically pumps the dark state atoms into the bright state, leading to more absorption of the probe beam in the crossover peak.

As illustrated in Figure 3.4b, there are two positive peaks corresponding to the resonance with the D2 transitions from $2\,^2S_{1/2}$, F=1/2 ground state to $2\,^2P_{3/2}$ excited level, and from $2\,^2S_{1/2}$, F=3/2 ground state to $2\,^2P_{3/2}$ excited level, separated by 228.2MHz. The negative peak located at the midpoint between these two positive peaks is the crossover resonance. In other alkalis, the hyperfine splitting in the ground level is very large (a few GHz), and the hyperfine splitting in the excited level is well resolved, forming a crossover regime with one ground hyperfine level and two excited hyperfine levels addressed, as described in Section 8.3.2 "Cross-over resonances in saturation spectroscopy" in [21]. However, in lithium, the unresolved excited level hyperfine splitting (smaller than natural linewidth) leads to an inverted crossover regime where two ground hyperfine levels and one excited hyperfine level are addressed.

By utilizing the lock-in amplifier, we have established a feedback circuit on the primary laser's cavity piezo-transducer and diode current locked to the zero-crossing of the differential of the photodiode signal, specifically the inverted crossover peak. This effectively stabilizes the primary laser's frequency against drifts over time, ensuring the precision and reliability of our spectroscopy setup.

Numerous parameters within this frequency stabilization setup required fine-tuning as part of our rejuvenation efforts. These included the sensitivity/gain, the integration time

constant, and the phase delay of the lock-in amplifier (Stanford Research Systems SR510). Additionally, the gain on the piezotransducer and diode current in the feedback circuit, as well as the primary laser's frequency mode, all required careful adjustment. After careful optimization, we successfully restored a stable lock.

In our routine operations, we keep a close eye on the Saturated Absorption Spectroscopy (SAS) Error signal, generated by the lock-in amplifier, and intermittently use the Highfinesse WS7 wavelength meter to monitor the frequency drift of our primary laser source. Despite maintaining a consistent lock to the crossover peak in SAS, we observed that the optical frequency of our primary laser, as measured by the wavelength meter, would still drift by several MHz per hour. This drift, comparable to the natural linewidth of the D2 transition, $\Gamma/2\pi$ =5.87MHz, initially raised concerns about its potential impact on the efficiency of MOT loading and other aspects of our experiment.

However, after a comprehensive investigation, which included scanning the resonance of our imaging beam on the atomic cloud, we concluded that this apparent drift was primarily due to a shift in the internal calibration of the wavelength meter, rather than a genuine drift in the lockpoint of the SAS frequency stabilization circuit.

With the revitalized and optimized SAS lock, we have successfully achieved a stability in the MOT atom number of better than 5%. This underscores the effectiveness of our frequency stabilization methodology.

### *3.1.3 MOT cooling and repump light*

With the frequency of the primary laser source stabilized, we have a solid foundation upon which to build the rest of our setup. A significant portion of the primary laser's power is allocated to the MOT cooling and repump lights. In both instances, a branch of the primary laser reflects off a PBS, undergoes a double-pass through an AOM setup (similar to the one used in the saturated absorption spectroscopy setup), and then passes through the PBS again. Following this, the repump light is coupled into an optical fiber, while the MOT cooling light traverses an optical isolator before being coupled into a separate optical fiber. The optical isolator is a necessary component for the MOT cooling light due to its

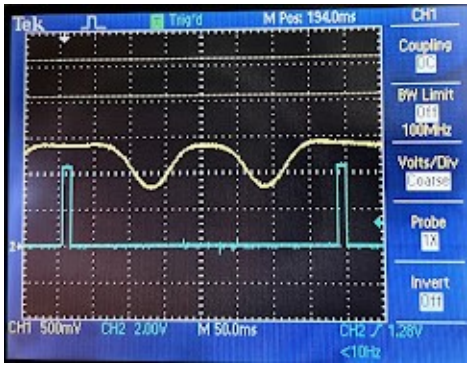


(a) Broad absorption spectrum of probe light by thermal Li vapor

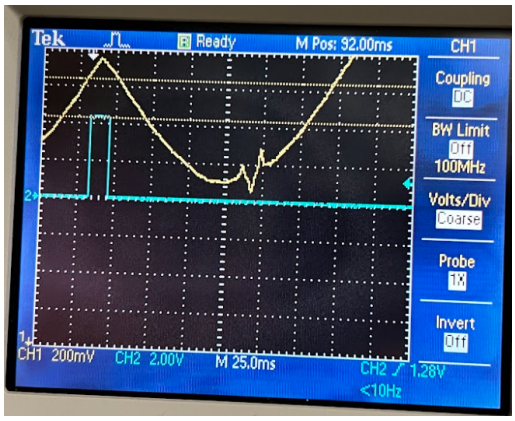


(b) Absorption spectrum of probe light in the presence of pump light

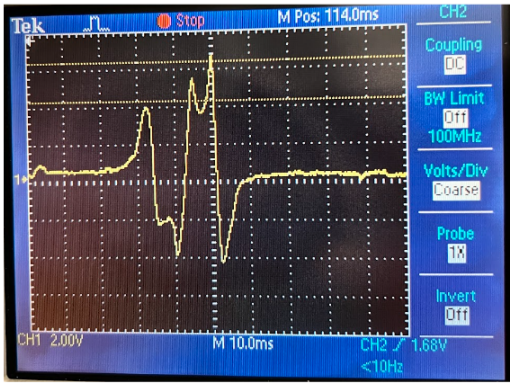


(c) Error signal output from the lock-in amplifier (differential of (b))

Figure 3.4: Absorption spectra on oscilloscope. (a) is the broad absorption spectrum of the probe light as it scans over a few GHz, showing about 50% absorption. The frequency scan follows a triangle waveform, and the same frequencies are shown twice between two triggers. (b) shows two Bennet hole in the D2 line from the hyperfine splitting (228.2MHz) in the ground state, and one inverted crossover peak. (c) is the differential signal of (b) produced by the lock-in amplifier, which is used as the Error signal for our feedback circuit to lock the laser to the central zero-crossing.

high optical power. Any backreflection of this light could potentially reach the primary laser source's laser diode, potentially causing instability and diode degradation.

At the output ends of the two fibers, the polarization of the MOT cooling light and the repump light are adjusted by half-wave plates before the two lights are combined by a PBS. This combined beam, consisting of the MOT cooling light and the repump light in perpendicular linear polarization, then passes through various polarization optics downstream and is split into three circularly polarized beams that are retro-reflected to form a MOT geometry.

A substantial part of our rejuvenation efforts was dedicated to re-optimizing the efficiency of several crucial components, such as the double-pass efficiency of the AOMs and the efficiency of the fiber couplings. Ultimately, our efforts were successful, and we managed to achieve ample power for our experiment.

### *3.1.4 Li Zeeman slower light*

The Zeeman slower necessitates a substantial amount of optical power for optimal operation, which is why it cannot be directly branched off from our primary laser source. Instead, we utilize a branch of our frequency-stabilized primary laser, which passes through a double-pass AOM setup and is then coupled into an optical fiber. This serves as the seed light for an injection lock of another high-power laser diode, with a red detuning from $\omega_{D2,F=3/2}$ by $122.88\Gamma$ as discussed in the beginning of Section 3.1.

The slave diode in the injection lock is housed in a Thorlabs diode mount. Its light is gently focused by a 250mm lens into an EOT (Electro-Optics Technology) optical isolator (4mm aperture, 650 nm wavelength), which is then collimated by another 250mm lens before being split by a PBS. This results in a low-power branch that feeds into a Fabry-Perot cavity for monitoring, and a major branch that is expanded by a telescope lens setup to become our Zeeman slower light. The EOT isolator operates based on the principle of Faraday rotation. Its design features exposed PBS cubes on both sides. The injection seed beam is directed to reflect off one of these cubes and counterpropagate with the slave diode's light, feeding into the slave diode to provide the injection lock. While most of the slave diode's

light passes through the EOT isolator, a portion of it reflects off the exposed cube and counterpropagates with the seed light, traversing through the optical fiber in the opposite direction. This optical fiber is thus termed the "two-way fiber". The coupling efficiency of the slave's light through this fiber represents the spatial overlap between the seed beam and the slave light, while the coupling efficiency of the seed beam through this fiber affects the power of the seed beam entering the slave diode.

The Thorlabs diode mount (Thorlabs LDM56) offers the functionality of receiving RF modulation to provide sidebands for the slave light. This is used to generate the sidebands (229MHz) for the repump light of the Zeeman slower light.

Achieving a successful injection lock necessitates the free-running mode of the slave diode to be within a few nanometers of the seed. It also requires meticulous adjustment of the temperature and current of the slave diode. During our rejuvenation efforts, we initially used an OpNext 0.65$\mu$m band AlGaInP laser diode with a multi-quantum well structure (HL6545MG, sold by Thorlabs), which I successfully managed to injection lock in August 2021. The characterization of this diode when injection-locked is shown in a HighFinesse Wavelength Meter spectrum (juxtaposed with the primary laser TA-100) in Figure 3.5, and a Fabry-Perot Interferometer signal in Figure 3.6. This setup provided 40 mW of slower power right at the viewport entry antipodal to our Li Zeeman slower.

After achieving a good injection lock and sufficient sideband (Figure 3.7), we also ensured that the spatial mode of the slower light was satisfactory. This entails a reasonably Gaussian profile in the transverse direction, meaning that the beam shape appears round with a sufficient diameter to envelop the atomic beam. Additionally, the beam should be mostly collimated with a gentle focus down to the nozzle of the atomic oven, so as to geometrically match the slower laser beam with the atomic beam. Of course, the optical alignment of the slower light to the direction of the atomic beam is crucial for achieving optimal slower performance.

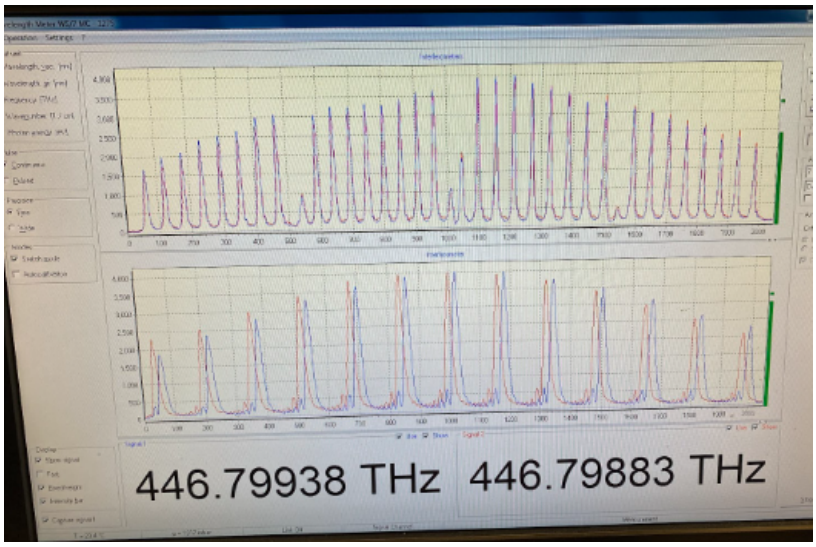


Figure 3.5: HighFinesse Wavelength Meter (WS7-30) spectrum of OpNext diode when injection-locked (blue), and the primary source laser (TA-100) before a frequency shift by the Zeeman slower AOM (red)

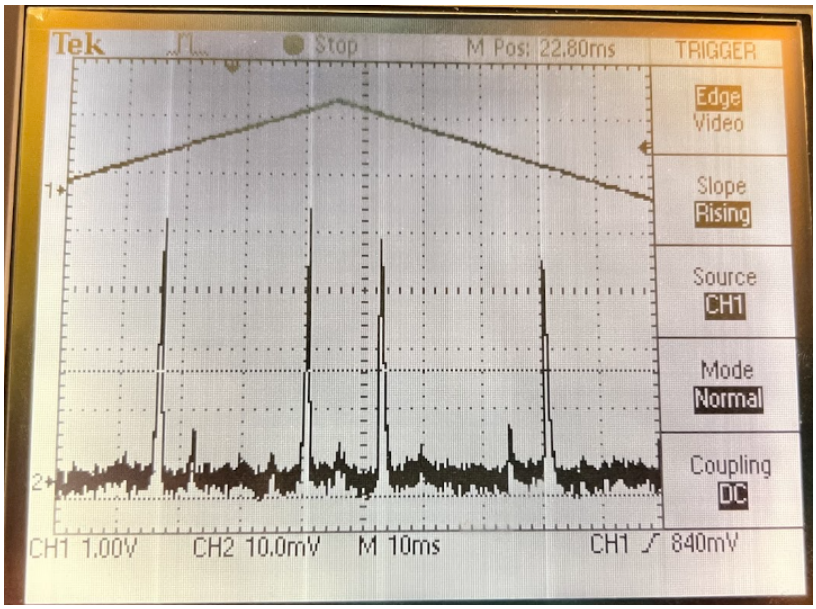


Figure 3.6: Fabry-Perot Interferometer signal of OpNext diode when injection-locked

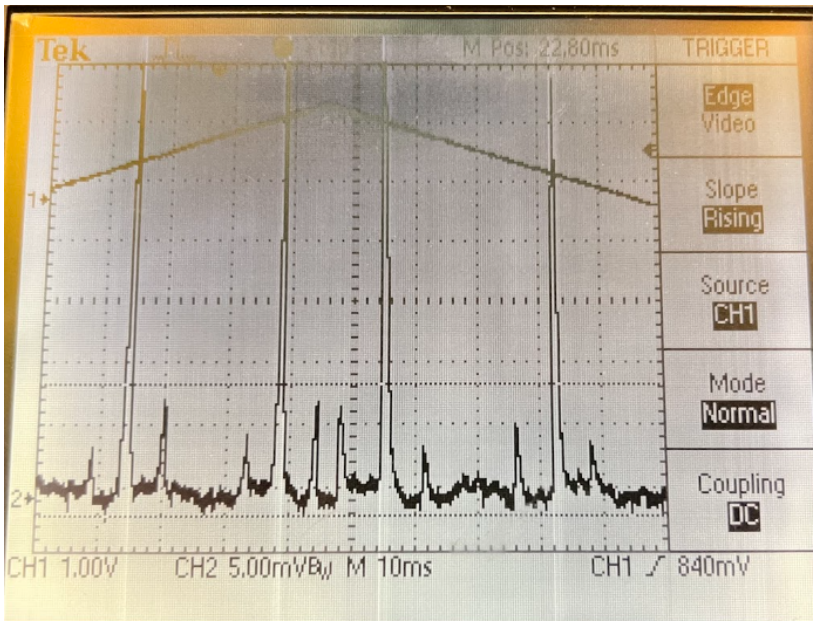


Figure 3.7: Fabry-Perot Interferometer signal of OpNext diode when injection-locked, with sidebands created from RF modulation of 229 MHz. The blue sideband has a lower power than the red sideband, which is due to the laser diode's cavity design.

*Li Zeeman slower viewport*

The Li Zeeman slower light is introduced into the vacuum system through a viewport located diametrically opposite to the Zeeman slower coils. The antipodal arrangement where photons counter-propagate with the atoms is crucial for optimal slowing of the hot Li atoms emanating from the Li oven, thereby enabling the Magneto-Optical Trap (MOT) to capture them. However, this setup has an unintended consequence - a continuous stream of Li atoms bombards the Li slower viewport. Over more than a decade, these Li atoms have accumulated on the vacuum side of the viewport, resulting in a visible layer of stain (see Figure 3.8), in spite of continuous heating of viewport at 200 degrees Celsius. This stain effectively attenuates the Li Zeeman slower light, posing a challenge for our experimental setup. Such a stain remains even after our attempt to "bake" it off by temporarily raising the viewport temperature.

Figure 3.8: Li Zeeman slower light entry viewport stain as of July 2021

Since the stain acts as an attenuation on our Li Zeeman slower light, one way to mitigate its effect would be increasing the slower light power. In 2023, we discovered a new product line of high-power (200 mW) diodes at 675 nm produced by Ushio (HL67001DG, AlGaInP laser diode with built-in monitor Photodiode). I undertook a comprehensive characteriza-

tion of this new diode, successfully achieved an injection lock, and managed to obtain more than double the optical power. The details of this characterization will be discussed in the final section of this chapter.

### *3.1.5 Li MOT loading*

In our quest to understand the cause of our struggles in Li MOT loading, we turned our attention to the polarization of our MOT light beams. For the MOT setup to function correctly, all the MOT beams need to maintain the appropriate circular polarization. However, between our previous successful Li MOT operation during the YbLi Magnetic Feshbach Resonance experiment in 2019 and our Li MOT rejuvenation efforts in 2022, several infrared (IR) optical components were added to our setup for the 1073 nm optical lattice beams used in our Yb-only bosonic dynamics experiment.

To investigate the potential impact of these changes, we conducted an optical test to determine the optimal angles for each forward quarter wave plate (QWP). The principle behind this test is that a linearly polarized light beam, after passing through a PBS and the forward QWP, should ideally return with a linear polarization perpendicular to its original orientation after being reflected back through the same QWP. This change in polarization would allow the retro-reflected light to be measured on a different side of the PBS.

However, due to the added IR optics and the birefringence of our vacuum viewports, the response of the retro-reflected light power versus the QWP angle was complex, featuring principal, secondary, and even tertiary maxima (see Table 3.1).

| | Vertical QWP | "MOT 1" QWP | "MOT 4" QWP |
|---|---|---|---|
| Principal Maxima | 8, 98, 188, 278 | 128, 308 | 170, 350 |
| Secondary Maxima | None | 75, 255 | 112, 292 |
| Tertiary Maxima | None | 32, 212 | None |

Table 3.1: Optical test result: QWP angles (in degrees) for the maxima of the power of the retro-reflected light. In all cases, adding 180 degrees to a QWP results in identical effect.

The optical test in Table 3.1 were performed with both the Li MOT and the repump lights. The results in the QWP for vertical MOT light was consistent with old records prior to 2019, showing a clear and regular 90-degree period. The results in the two horizontal MOT paths, however, were inconsistent with records before 2019, which may be due to the added IR optics such as the dichoric mirrors for optical lattices setup. In addtion, we had a slightly different MOT and repump power ratio in our current setup than the Li setup in 2019 and prior; the birefringence of the various viewport may also had an effect in the polarization of the MOT and repump lights.

After identifying the potential optimal values for the three forward MOT QWPs, we iterated through all combinations of these values. Eventually, we were successful in loading the Li MOT (with vertical QWP at 8 degrees, "MOT 1" QWP at 75 degrees and "MOT 4" QWP at 170 degrees) and visually observing the strong fluorescence of the loaded Li MOT. We then rejuvenated the double-pass AOM for Li absorption imaging, calculated the necessary RF frequency on the AOM for the imaging light to resonate with the atoms, and aligned the light to the MOT by illuminating the MOT with this light and visually observing the effect of the resonant imaging light blasting the loaded MOT atoms away. This process allowed us to rejuvenate the absorption imaging for the Li MOT.

With a quantitative measure of the atom number in our MOT from the absorption imaging, we were able to plot the MOT load number against the MOT loading time (Figure 3.9). An exponential fit to this data yielded a time constant of approximately $\gamma^{-1}$ =7 seconds. The number of atoms $N$ loaded into the MOT follows the equation $dN/dt = L - \gamma N$ with a solution of $N(t) = (L/\gamma)(1 - e^{-\gamma t})$, where $L$ is the loading rate, and the single-body loss rate $\gamma$ depends on the atom's collision with the photons in the laser beams and the detuning of the laser from the atomic transitions. Note, however, that due to the presence of various laser fields (e.g. Li Zeeman slower light), this time constant is not the same as the lifetime of the atoms when held in the MOT for a long time; the latter would be much longer than the former.

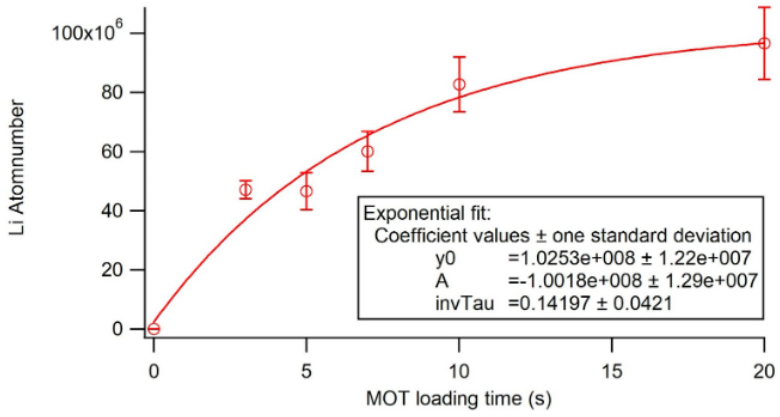


Figure 3.9: Li MOT number vs MOT loading time measurement

*Compressed MOT (CMOT)*

As mentioned in the beginning of Section 3.1, the parameters used for capturing the atomic beam (which has been slowed by the Zeeman slower) in our MOT are optimized for the maximum loading rate. This requires a large red-detuning in the light frequencies and a high intensity in the light power, but to reach a lower temperature and a higher atom number density, we need to perform a stage of compression on the MOT.

Through our investigations, we found that the optimal compression regime involves a linear continuous ramp of the magnetic fields and a two-stage ramp of the light frequencies and intensities. As seen in Figure 3.10, in the first 10 ms of the compression, the light intensities (Cicero analog channels "Li MOT amp A0" and "Li repump amp A1") quickly go down, whereas the light frequencies (Cicero analog channels "Li MOT freq 2-A2" and "Li repump freq 2-A3") remain constant; over the remainder (30ms) of the compression timestep, the intensities gradually ramp to nearly zero, while the frequencies gradually ramp to a value for lowest CMOT temperature. This regime also allows for optional optical pumping if we use the digital TTL channel to switch off the MOT repump light during the final few milliseconds of the MOT compression step, and thus allowing the MOT light to pump the Li atoms out of the dark state. This is useful for diagnostic purposes, as our imaging light is tuned to be in resonance with a specific ground state of $^6$Li.

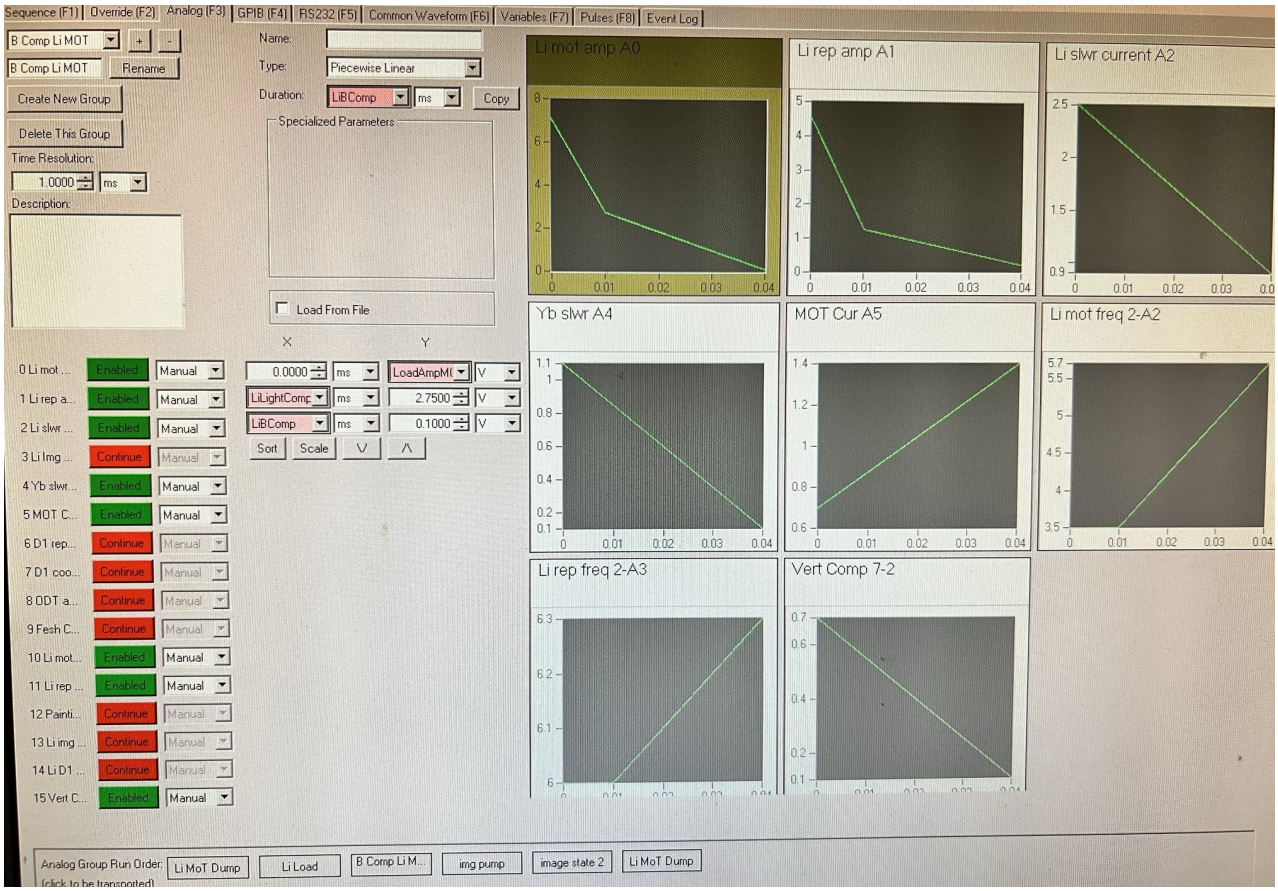


Figure 3.10: Photo of the Li MOT compression step in Cicero Word Generator software

The stabilization of the intensity of the MOT and repump light is a critical aspect of our experimental setup. Fluctuations in the MOT potential can lead to heating of the atoms, thereby posing a limitation on the Compressed Magneto-Optical Trap (CMOT) temperature. To mitigate this, we employ an intensity stabilization setup. A photodiode is used to measure a small but consistent portion of the light we aim to stabilize. The signal from the photodiode is then sent to a stabilizer circuit, where it is compared with a setpoint analog voltage. After undergoing some electronic voltage gain in the stabilizer circuit, the resultant difference signal is sent to control the amplitude of the light, typically via the RF signal amplitude for the Acousto-Optic Modulator (AOM) that controls this light. This setup forms a negative feedback loop, which achieves the desired intensity stabilization.

The DC electric currents used to generate our magnetic fields can be switched on/off using digital TTL channels. However, due to the self-inductance and mutual inductance of our magnetic coils, each coil exhibits unique and yet intertwined transient behaviors during snap-off. These transient behaviors of the magnetic fields must be carefully considered for the successful execution of our MOT compression process, as well as the D1 cooling step that follows.

We conducted a comprehensive investigation into the transient behavior of the various magnetic coils in our system. Based on our findings, we designed a set of pre-triggers to send the switch-off TTL signal to each coil's current controller at various times before the end of the compression timestep. This orchestrated transient behavior in the coils allows us to achieve optimal parameters in the compressed MOT and the atomic cloud after D1 cooling, specifically the number of atoms and the temperature of the cloud. The following sections will delve into the details of the characterizations of the transient behaviors and the eventual design of pre-triggers.

To investigate the transient behavior of each coil individually, I employed a handheld AC/DC current probe (Omega HHM72), to clamp on each cable responsible for transmitting the electric current to the corresponding coil. I then set up a "scope trigger" in the Cicero sequence, whose rising edge marks the end of the MOT compression and also signifies the start of the next timestep. The voltage signal from the current detector is fed into an oscilloscope and is compared to the aforementioned "scope trigger" signal to check for

delays, upshots, and fall time.

One of the coils we examined was the Li Zeeman slower's short coil, which provides an increasing magnetic field until the atoms exit the Zeeman slower and enter the main chamber. As shown in Figure 3.11, this coil exhibited a delay of turn-off by about 200 $\mu$s.

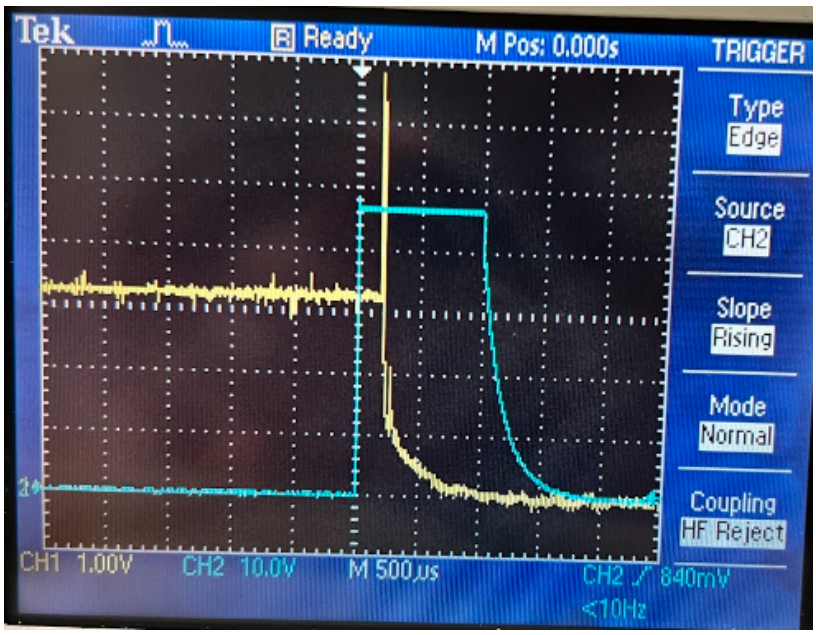


Figure 3.11: Oscilloscope trace of the Li Zeeman slower's short coil's transient behavior. Yellow trace (Channel 1) is the signal from the Hall probe (FW Bell CLN-300), and blue trace (Channel 2) is the "scope trigger" signal.

The Li Zeeman slower's long coil, responsible for providing a decreasing magnetic field from the point where the atoms enter the Zeeman slower to the point where the atoms enter the Li Zeeman slower's short coil, has a turn-off delay of approximately 300 $\mu$s, as illustrated in Figure 3.12. Since this coil is situated at a significant distance from the location of the MOT, its transient behavior does not notably influence the CMOT. However, this detail is included in this section for the sake of completeness.

The Li slower's short coil, due to its close proximity to the center of the Magneto-Optical Trap, produces some unwanted residual magnetic field, which negatively impacts the MOT

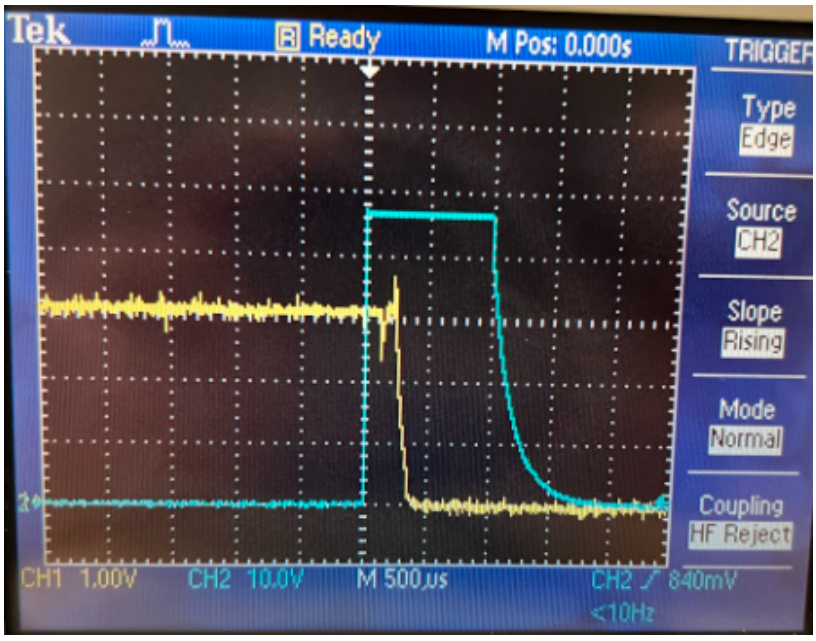


Figure 3.12: Oscilloscope trace of the transient behavior of the Li Zeeman slower's long coil. Its distance from the MOT location ensures that it does not affect the CMOT in any significant manner.

loading. Therefore, we have a compensation coil to offset this residual field. This Li slower compensation coil exhibited a delay of turn-off by about 200 $\mu$s, as shown in Figure 3.13.

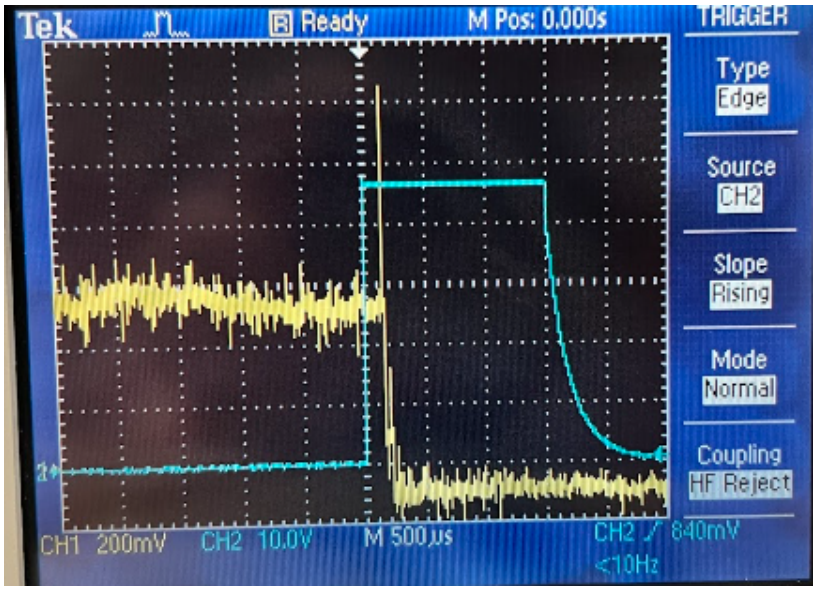


Figure 3.13: Oscilloscope trace of the Li Zeeman slower's compensation coil's transient behavior.

The geomagnetic field in Seattle has a major vertical component. Additionally, the stray magnetic fields from ion pump magnets contribute in all three directions at the MOT, including an appreciable vertical component. These factors necessitate a compensation coil in the vertical configuration. The vertical compensation coil exhibited a turn-off delay of approximately 250 $\mu$s, as shown in Figure 3.14.

Finally, the anti-Helmholtz coils used to produce magnetic field gradient for the MOT exhibited a delay of turn-off by about 250 $\mu$s, as shown in Figure 3.15.[2]

The value of DC currents through the aforementioned coils at the MOT loading step and the MOT compression endpoint are as follows:

[2]The complete magnetic coil system in our apparatus also includes Yb slower coil and its own compensation coil, but these coils were kept off in our Li-only operations and were therefore not characterized in this study.

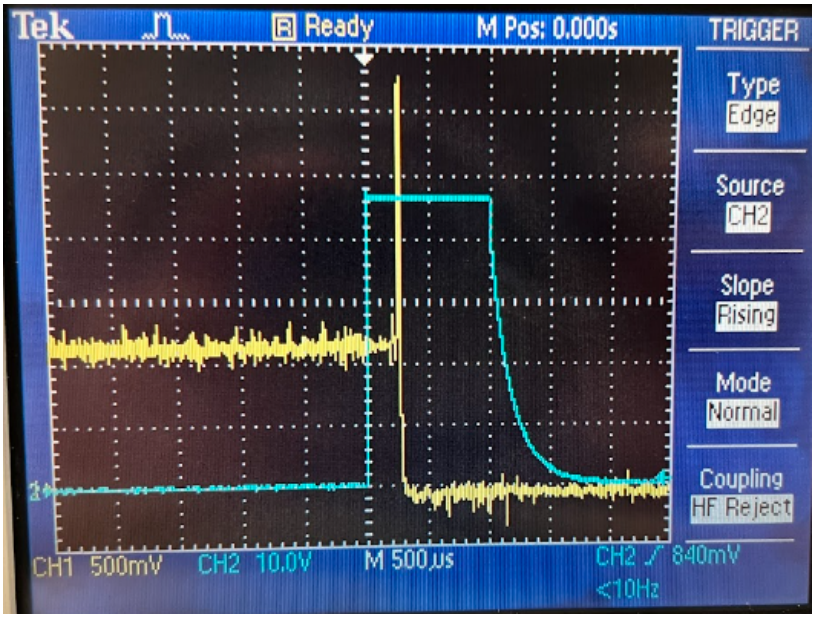


Figure 3.14: Oscilloscope trace of the vertical compensation coil's transient behavior.

1. MOT gradient coil: This coil in anti-Helmholtz configuration provides the magnetic field gradient for the MOT setup. Its DC current at MOT loading is 28A, and at compression endpoint it's 56A.

2. "Li Long" coil: This is the first coil encountered by the Li vapor after the atomic oven nozzle, which produces a decreasing magnetic field in the first section of the Li Zeeman slower. Since it's far away from the atomic cloud in MOT, the DC current is not controlled dynamically within a typical experimental sequence, and is held at 30.3A.

3. "Li Short" coil: This is the second coil encountered by the Li vapor after "Li Long" coil, and the second part of the Li Zeeman slower. Its DC current at MOT loading is 30.0A, and at compression endpoint it's 9.8A.

4. Li slower compensation coil: This coil is not controlled dynamically, and is held at 6.0A.

5. Yb slower coil: This coil is at 11.4A at MOT loading, and 0A at compression endpoint.

6. Yb slower compensation coil: This coil is used to compensate the effect of the Yb slower coil at the MOT location. It's not dynamically controlled, and is held at 7.0A. For Li-only operations, these two coils mostly provide a control on the bias field along the axis of Yb Zeeman slower to move the location of the magnetic zero point of the MOT for optimizing the MOT loading and CMOT temperature.

7. Vertical compensation coil: This coil is at 7.3A at MOT loading and 1.2A at compression endpoint.

By referring to prior theses from our lab [33], the above DC current values can be converted to the magnetic field values at the location of the MOT.

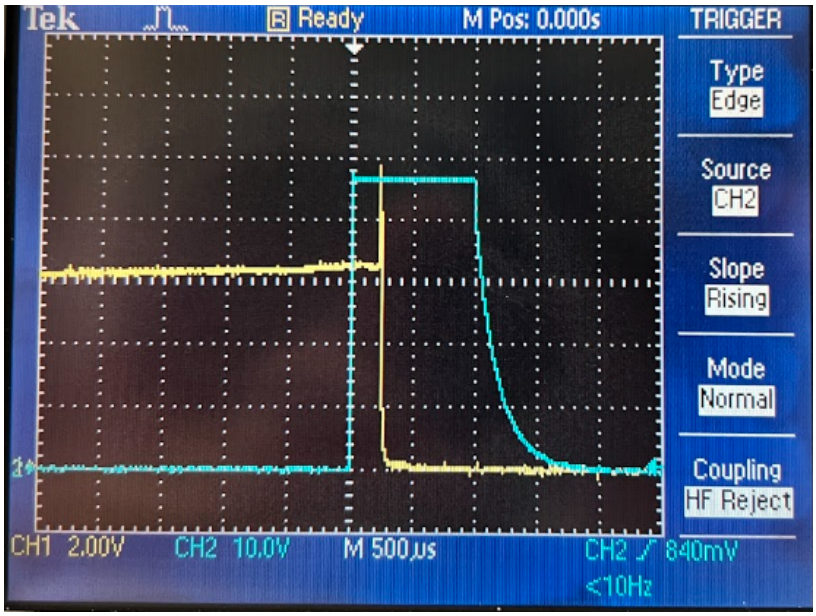


Figure 3.15: Oscilloscope trace of the MOT gradient coil's transient behavior.

Through these characterizations and some trial and error, we engineered a set of pre-triggers to optimize the temperature and the atom number of our CMOT. In late May 2023, we had about $1 \times 10^8$ atoms at 350 $\mu K$ in CMOT. As it gets closer to the Doppler cooling

limit of $T_D = 141$ $\mu$K (see Chapter 2), we will require sub-Doppler cooling for further reduction in temperature, which is conducive to efficient loading into the Optical Dipole Trap (ODT).

## *3.2 Sub-Doppler cooling with D1 transition*

The technique of sub-Doppler cooling of $^6$Li using the gray molasses mechanism and the D1 transitions was demonstrated by Burchianti et al in 2014[13], and was implemented in our lab around 2015[69]. However, by the time I joined the group in 2017, this setup had been disassembled and its components repurposed for other applications, such as photoassociation experiments. In 2022, as part of our efforts to achieve Fermi degeneracy, we undertook the task of reassembling the D1 cooling setup.

*Wavelength meter lock*

D1 cooling of $^6$Li necessitates two light beams with a frequency separation of approximately 228 MHz to address the two ground states of this alkali atom. This relative detuning between the two beams is referred to as the Raman detuning, as the effective D1 cooling mechanism involves a coherent two-photon process. Furthermore, the absolute detuning between the light frequency and the atomic transition frequency must be a blue-detuning to ensure that the Sisyphus mechanism results in cooling rather than heating.

In our reconfigured setup, we restored the employment of a HighFinesse WS7/1275 wavelength meter to continuously monitor the frequency of the Toptica DL100 laser. A branch of the laser light is fiber-coupled to the wavelength meter, and the live data is transmitted to a computer via serial communication (USB port). This data is processed by the HighFinesse software, and a LabVIEW Virtual Instrument accesses the live feed data through the HighFinesse software's API (Application Programming Interface). A PID (Proportional-Integral-Differential) feedback algorithm is then used in the LabVIEW VI to generate an output voltage that is fed into the Analog Interface module of the Toptica DL100's controller. This voltage adjusts the laser cavity's piezo voltage, acting as an actuator for the feedback loop. To ensure a sufficiently broad mode-hop-free range, we adjusted the feedforward gain between the piezo voltage and the diode current.

Due to the inherent limitations of serial communication and digital processing, the bandwidth of this feedback circuit is restricted to about 100 Hz[69]. However, the effectiveness of D1 cooling is less sensitive to the absolute detuning and more dependent on the Raman detuning, making this setup suitable for our purposes. Further details on the results of the D1 cooling process are provided in the following sections.

*D1 optical setup*

In our re-established D1 cooling setup, we've implemented an innovative upgrade that involves utilizing two orders from the same Acousto-Optic Modulator (AOM) for the D1 cooling and repump lights. This design, which is detailed in Figure 3.16, is a testament to the synergistic efforts of our team, with special acknowledgements to Cole and Carson for their major contributions. We use a Toptica DL100 Tunable Diode Laser as a single-mode seed laser at 671 nm. The output from this laser, after undergoing beam shaping by cylindrical lenses and optical isolators, is fed into a homebuilt Tapered Amplifier system with an Eagleyard TA chip. This amplified power, typically exceeding 230 mW, is then fed into an AOM at around 151 MHz frequency, after further beam shaping and telescoping (to reduce the beam diameter for better diffraction efficiency at the AOM). The -1 order from this AOM is directly designated to address the D1 cooling transition (between the ground state with F=3/2 and the first excited state), and the 0th order is fed into an AOM at about 77 MHz. We take the +1 order from this second AOM to address the D1 repump transition (between the ground state with F=1/2 and the first excited state), which is about 228 MHz higher than the D1 cooling transition. The D1 cooling and repumping beams are then combined by polarization optics (HWPs and PBS) before being fibered to the main table setup, where they join the Magneto-Optical Trap (MOT) beams and are divided by the Polarizing Beam Splitters (PBSs). The use of polarization optics to combine the D1 cooling and D1 repump beams meant that these two beams had perpendicular linear polarizations, leading to an uneven split of the D1 cooling/repump beams as they traversed the polarization optics (HWPs and PBSs) in the MOT beam setup to be split into three orthogonal dimensions. This resulted in a power imbalance in the three dimensions of the D1 cooling setup, which

posed a challenge in achieving optimal D1 cooling temperature and atom number in the cloud after D1 cooling.

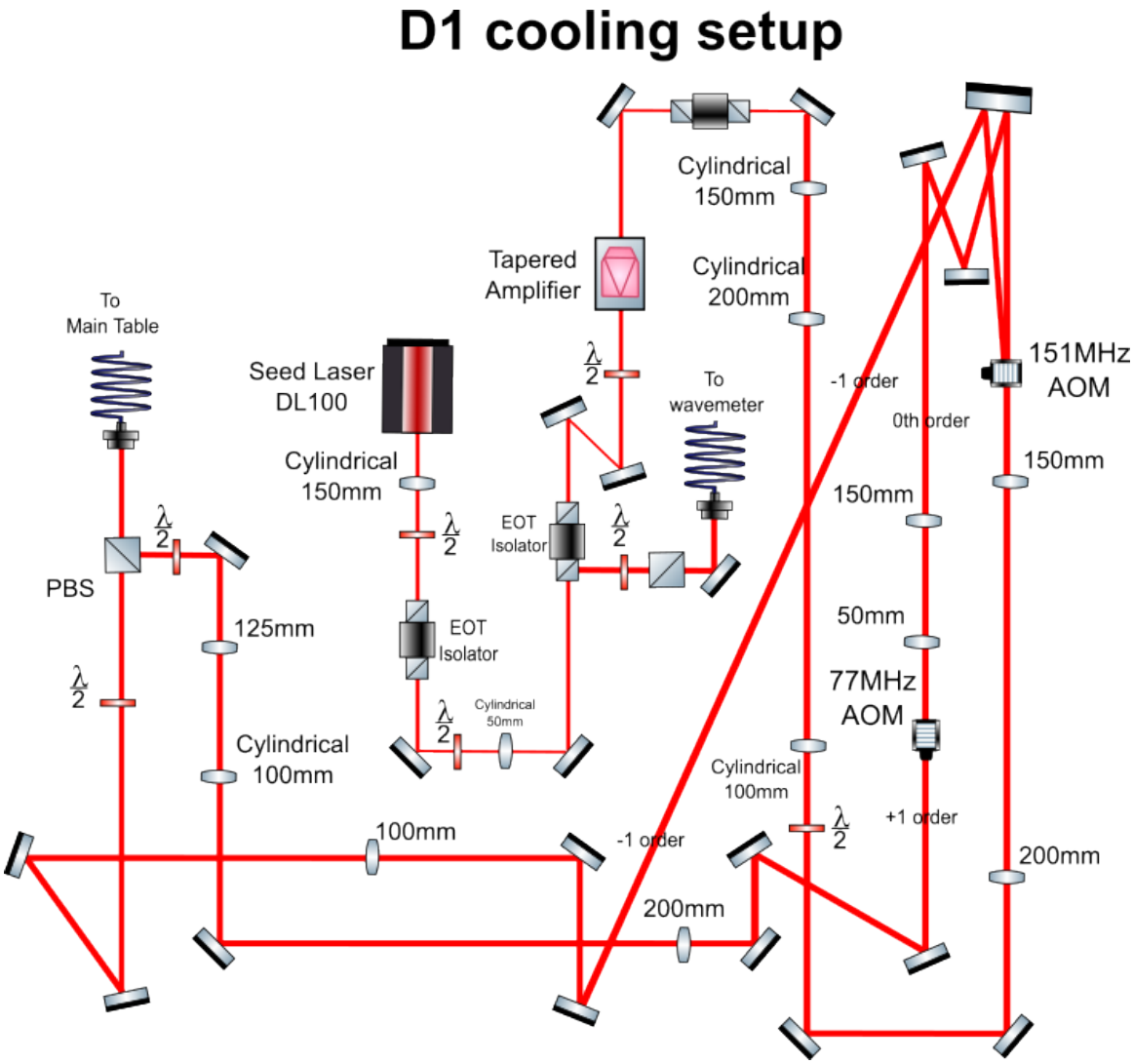


Figure 3.16: D1 cooling optical system layout

The alignment of the D1 beams onto the atomic cloud's position after MOT compression has proven to be vital to the success of D1 sub-Doppler cooling. Since the D1 cooling makes use of the polarization gradient created by the standing wave formed by the forward beam and the retro-reflected beam in each of the three dimensions, the alignment of the retro

beam to the forward beam is also crucial to its success. For the forward beam, due to its strong optical power, even with the detuning from the resonant atomic transition, we were still able to "blast" the atoms in the MOT away with its optical force; this provided us with a visual clue to align the forward D1 beams to the atomic cloud. We then attenuated the light power with the control on the RF amplitude of the relevant AOM, and then refined our optical alignment to still get blasting, until the power is so low that we can't blast the atoms away anymore. The alignment of the retro-reflected beam is performed with a paper card with a punched hole on it. The forward beam passing through the hole will traverse through the optical path, eventually reflecting off the retro-mirror (shared by MOT beams). Since we don't want to disturb the MOT beam alignment, we used a different mirror before the D1 beams are combined with the MOT beams to steer the beam's direction such that the reflected beam passes through the same hole that the forward beam passes through. After these coarse alignments are done, fine alignment is done with reference to the atomic cloud's width and height in the absorption imaging after a set amount of Time of Flight, which represents the atomic cloud's temperature after the D1 cooling step.

The alignment of the D1 beams onto the atomic cloud's position after MOT compression has proven to be vital to the success of D1 sub-Doppler cooling. Since the D1 cooling makes use of the polarization gradient created by the standing wave formed by the forward beam and the retro-reflected beam in each of the three dimensions, the alignment of the retro beam to the forward beam is also crucial to its success. For the forward beam, due to its strong optical power, even with the detuning from the resonant atomic transition, we were still able to "blast" the atoms in the MOT away with its optical force; this provided us with a visual clue to align the forward D1 beams to the atomic cloud. We then attenuated the light power with the control on the RF amplitude of the relevant AOM, and then refined our optical alignment to still get blasting, until the power is so low that we can't blast the atoms away anymore.

The alignment of the retro-reflected beam is performed with a paper card with a punched hole on it. The forward beam passing through the hole (placed at the center of the forward beam's transverse profile) will traverse through the optical path, eventually reflecting off the retro-mirror (shared by MOT beams). Since we don't want to disturb the MOT beam

alignment, we used a different mirror before the D1 beams are combined with the MOT beams to steer the beam's direction such that the reflected beam passes through the same hole that the forward beam passes through. After these coarse alignments with visual clues are done, fine alignment is done with reference to the atomic cloud's width and height in the absorption imaging after a set amount of Time of Flight, which represents the atomic cloud's temperature after the D1 cooling step.

Aside from the optical alignment, the frequencies of the D1 cooling and D1 repump beams are also vital for optimal D1 temperature and atom number. After the optical alignment is finely optimized, we varied the wavelength meter setpoint in the LabVIEW VI to change the frequency that the DL100 laser is locked to, which effectively changed the absolute blue detuning of the D1 cooling and repump beams from the resonant atomic transition frequency. In addition, we used the control on the RF frequency of the AOMs to vary the relative Raman detuning between the D1 cooling and the D1 repump beams. We found that the D1 cloud temperature and atom number are much more dependent on the Raman detuning than the absolute detuning from the atomic transitions, as we expected from literature [13, 69, 30].

In late May 2023, we had about $8 \times 10^7$ atoms at about 100 $\mu K$ after D1 sub-Doppler cooling, allowing us to proceed with further investigations and applications of the cooled atomic cloud.

### *3.3 Optical Dipole Trap, spin mixture and evaporative cooling*

An Optical Dipole Trap (ODT) is a setup utilized in atomic physics to confine neutral atoms using the dipole force, which originates from the interaction between the electric field of a light beam and the induced dipole moment of the atoms.

In an ODT, a high-powered laser beam is focused to a small spot, generating a spatially varying electric field. The atoms are drawn towards the regions of highest electric field intensity, typically at the center of the laser beam, resulting in a trapping potential for the atoms.

The efficiency of loading cold atoms into an ODT is heavily influenced by two factors: the temperature of the atoms relative to the potential depth of the ODT, and the spatial

overlap between the tightly focused ODT beam and the atomic cloud.

In our experimental setup, we employ a high-powered (typically operating at 50W) IPG fiber laser operating at 1064 nm to generate the Optical Dipole Trap (ODT) light beam. After rejuvenating our Li Magneto-Optical Trap (MOT) and subsequently re-optimizing numerous parameters, from MOT loading to MOT compression and D1 cooling, we discovered that the location of our Li atomic cloud was significantly distanced from the focus of the ODT. However, our setup enabled us to establish a secondary imaging path, allowing the imaging light to trace the path of the ODT beam, identify its position, and adjust the direction and focus of the ODT beam accordingly. The diagram of the ODT beam's optical path can be found in previous theses from our lab [79].

After the ODT beam's initial pass through the vacuum chamber, it is reflected off a high-reflectivity IR mirror. Only a small fraction of the ODT power, a few milliwatts, penetrates through the mirror and is subsequently collected by our imaging system, which comprises 2" lenses and an Andor CCD camera. This IR mirror is highly transmissive for our 671 nm imaging light, thereby enabling us to utilize this secondary imaging path to capture an image of the atomic cloud on the camera, identify the cloud's position, and then employ the camera's video mode (continuous capture) to adjust the transverse X-Y direction ("the pointing") of the ODT's first pass. Furthermore, the lens used to focus the first pass of the ODT beam at the atomic cloud is mounted on a translation stage, allowing us to adjust the focus of the ODT along the longitudinal direction (Z-direction).

Despite these efforts, we encountered difficulties in achieving high loading efficiency with the single-beam ODT. This led us to undertake a comprehensive characterization of the spatial mode of the ODT beam. We made use of the few milliwatts of ODT light leaking through the IR mirror to capture its images on our Andor camera, and used the translation stage for the lens that focuses the first pass ODT beam onto the atomic cloud to move the ODT beam in the longitudinal direction, effectively producing a series of cross sections of the ODT beam on the imaging plane of the CCD camera. The resulting conclusion was that our ODT beam has a reasonably good Gaussian mode (with a trap depth of about $k_B \times 2.15$mK, much greater than the temperature of the atomic cloud after D1 cooling; see section 2.4.1), and its measured Rayleigh range is in agreement with its beam waist ($w_0 = 30\mu$m [69, 79])

and its wavelength (1064nm).

We have achieved preliminary loading of the atomic cloud after D1 cooling into the single-beam ODT. After further improvement on the ODT loading efficiency and the single-beam ODT reaches a satisfactory atom number and temperature, the next step would be setting up the second pass of the ODT beam to form a cross-beam ODT configuration, for higher loading efficiency and higher trap depth. The establishment of the second pass ODT beam could be achieved with the aid of a tertiary imaging path that's next to one of our horizontal MOT laser beams.

After achieving satisfactory atom number and temperature in the cross-beam ODT, the next step would be to set up evaporative cooling to reach a Fermi condensate. This process necessitates the presence of a high magnetic field bias and the preparation of an even spin mixture between the two spin states of $^6$Li in the ground state (Figure 2.2). This is to ensure ample s-wave scattering for the re-equilibration of the ensemble following the "spilling" of hot atoms due to the reduction of the trapping potential during evaporative cooling.

The setup of a high magnetic field bias requires an increase in the pressure of our water cooling system for the magnetic coils. This has been achieved by activating a booster pump and upgrading the interlock system, which included deploying flow rate meters with a larger range and establishing new high-flow and low-flow thresholds for the interlock. All of these tasks have been successfully completed.

The presence of a high magnetic field bias also shifts the resonant atomic transition frequency used for absorption imaging. This necessitates some adaptation of our imaging AOM setup and some re-calibration of the RF frequencies used, tasks which have also been successfully completed. The preparation of a spin mixture has been achieved in the history of our lab using Landau-Zener pulses of RF waves of scanning frequencies, as described in a previous thesis from our lab [69].

In conclusion, we have made substantial strides in our experimental setup, paving the way for the experimental exploration of quantum dynamics and transport with Fermi condensates. Looking ahead, our focus will be on enhancing the loading efficiency of the single-beam ODT, recovering the cross-beam ODT configuration, and incorporating evaporative cooling. These advancements will propel us closer to achieving a Fermi condensate

and superfluid.

### *3.4 Magnetic field stabilization*

In 2019, following the successful execution of our YbLi Magnetic Feshbach Resonance experiment [29, 28], we turned our attention to the coherent formation and dissociation of YbLi molecules. This ambitious project necessitated a dual-pronged approach: first, the establishment of a dual-species optical lattice to ensure the presence of a single Yb atom and a single Li atom at each lattice site; second, the development of a magnetic field stabilization system capable of scanning Magnetic Feshbach Resonances as narrow as approximately 1 mG, at a field strength of around 700 G. The lattice setup [79] played a pivotal role in our investigation of $^{174}$Yb bosonic dynamics [76, 80], while the magnetic field stabilization is the primary focus of this section.

The benefits of a dynamically scannable, highly stabilized magnetic field extend beyond the exploration of narrow MFRs in YbLi. For instance, in the case of fermionic $^{6}$Li, several narrow p-wave resonances [75] and one narrow s-wave resonance can be more effectively probed with a stable magnetic field.

To achieve a high degree of stability at a few parts per million (ppm), we first needed to characterize the noise in our existing Feshbach field system (power supply plus magnetic coils), and then stabilize it to a 1 ppm level. In our previous experiment on YbLi Magnetic Feshbach Resonance [29], we found in our loss spectroscopy of spin-polarized heteronuclear mixture that the passive stability of our Feshbach field setup was about 50mG at 500G (or 100ppm). However, without the use of cold atoms as sensors, electronically detecting and stabilizing noises at the 1 ppm level required a tool with greater precision than the Hall Probe that we had in our lab (FW Bell CLN-300), which offers a precision of approximately 0.5%.

Several recent publications [57, 70] reported achieving exceptional magnetic field stability using LEM's fluxgate transducer. This technology balances the magnetic flux produced by the primary current (i.e. the current we aim to measure) with an internal secondary current. As a result, the secondary current becomes a proportional (but much smaller) replica of the primary current, which then becomes the output current signal to be converted into a

voltage signal by a load resistor. Fluxgate technology offers a non-intrusive, high-accuracy measurement of high currents. Consequently, we decided to procure the LEM 1000-S/SP1 model for this application.

Among the papers we referenced, Benjamin Merkel's design [57] achieved the highest stability at 0.29 ppm, and we chose to follow this one. However, it's important to note that our application has many technical differences from Merkel's setup, and it was therefore necessary for us to conduct our own noise analysis on our LEM 1000-S/SP1 and Feshbach field system (power supply plus magnetic coils) to determine what modifications we needed to make to Merkel's circuitry design, before committing to assembling the Bill of Materials and ordering the manufacturing of the circuit boards from fabrication companies like Screaming Circuits.

Merkel's paper mentions a 17kHz fluxgate clock noise and its harmonics (51kHz) from their LEM IT 400-S. However, we needed to determine the fluxgate clock noise from our current transducer (LEM 1000-S/SP1). Additionally, we wanted to understand the noise spectrum of our existing Feshbach field system (power supply plus magnetic coils) to assess if we needed to make further adaptations to the feedback circuitry. The challenge here was detecting a 1 ppm noise amidst a large bias current (over 100A).

Inspired by Merkel's philosophy in the overall circuit design, I prototyped a homemade tester board (Figure 3.17) using through-hole components soldered onto a breadboard. This tester board processes the output current signal from the LEM 1000-S/SP1 in the following manner: it first converts the output current signal to a voltage signal via a load resistor. This voltage signal is then compared with a DC setpoint, which is generated by a potentiometer and a stable DC voltage reference chip. The difference between these two signals, referred to as the Error signal, is then amplified.

It's important to note that the current signal output from the LEM 1000-S/SP1 undergoes a total gain of 200V/A in the process of contributing to the amplified Error signal. This amplified Error signal is then sent to an SR780 Network Signal Analyzer from Stanford Research Systems for spectrum analysis.

Using this prototype tester board and the network signal analyzer, we discovered that in the absence of any primary current running through its detection aperture, our LEM

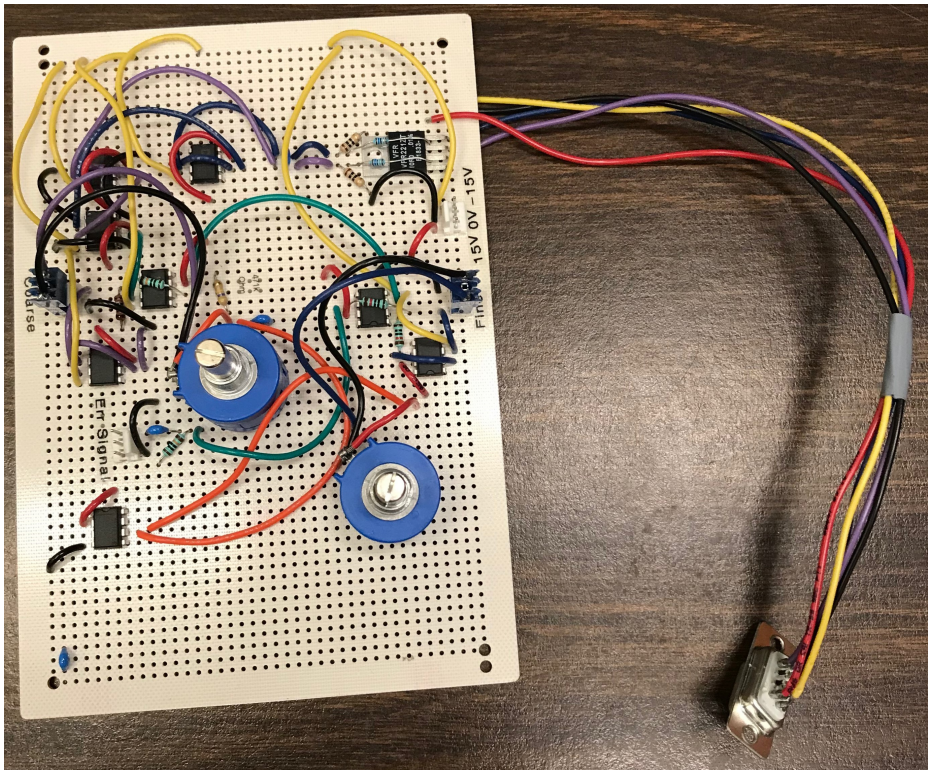


Figure 3.17: Prototype tester board for initial current noise characterization in the Magnetic Field Stabilization project. The two POTs are used for coarse and fine control of the setpoint, and the remainder mostly follows the differential amplifier design from Figure 3.23.

1000-S/SP1 still produces fluxgate noises in its current signal output (i.e. the secondary current) at 14kHz and harmonics (42kHz). In Figure 3.18, the noise spectrum with zero primary current in our Feshbach magnetic coil is characterized, showing the 14kHz and harmonics from the fluxgate clock noise. The purple spectrum shows the noise with the wire for the primary current still inside the detection aperture of LEM 1000-S/SP1, and yellow spectrum shows the noise with the wire on (although with zero primary current). The SR780 Network Signal Analyzer is set to collect 800 frequency lines for each data set, which is the maximum sampling limit. Due to this sampling limit, a complete spectrum from 1Hz to $10^5$Hz requires the collection of two spectra in two different frequency ranges, but with careful data processing we were able to parse out the complete noise spectrum. This zero-primary spectrum informs us that we need to adapt the narrow notch filter to act at 14kHz (Figure 3.19) instead of 17kHz in Merkel's design, and the low-pass notch filter to have a double-zero at 42kHz (Figure 3.20) instead of 51kHz in Merkel's design.

We then obtained the noise spectrum of our Feshbach field system (power supply plus magnetic coils) for low primary current (34.4A running in our magnetic coils), shown in Figure 3.21, as well as for higher primary current (103.1A running in our magnetic coils), shown in Figure 3.22. We can clearly see in Figure 3.22a the presence of 60Hz and harmonics from our Feshbach field system, and in Figure 3.22b the 14kHz and harmonics from the fluxgate clock noise.

During our preliminary noise analysis, we anticipated that in order to minimize the effect of the fluxgate sensor noise and other electronic processing noise in our feedback loop, we would want to loop the primary current around the LEM 1000-S/SP1 sensor multiple times (Merkel's design winded their primary current 6 turns around the sensor), so that the "real" noise from the primary current (running in our magnetic coils) can be the prominent component in the Error signal for the feedback loop. As our operating current is much higher than the 60A in Merkel's setup, this winding regime required that the load resistance of 10Ω in Merkel's design be accordingly reduced to 2Ω, as shown in our adapted design of the differential amplifier (Figure 3.23).

With these adaptations confirmed, I proceeded to find the necessary part numbers, assemble the Bill of Materials, and ordered the manufacturing of the finalized circuit boards

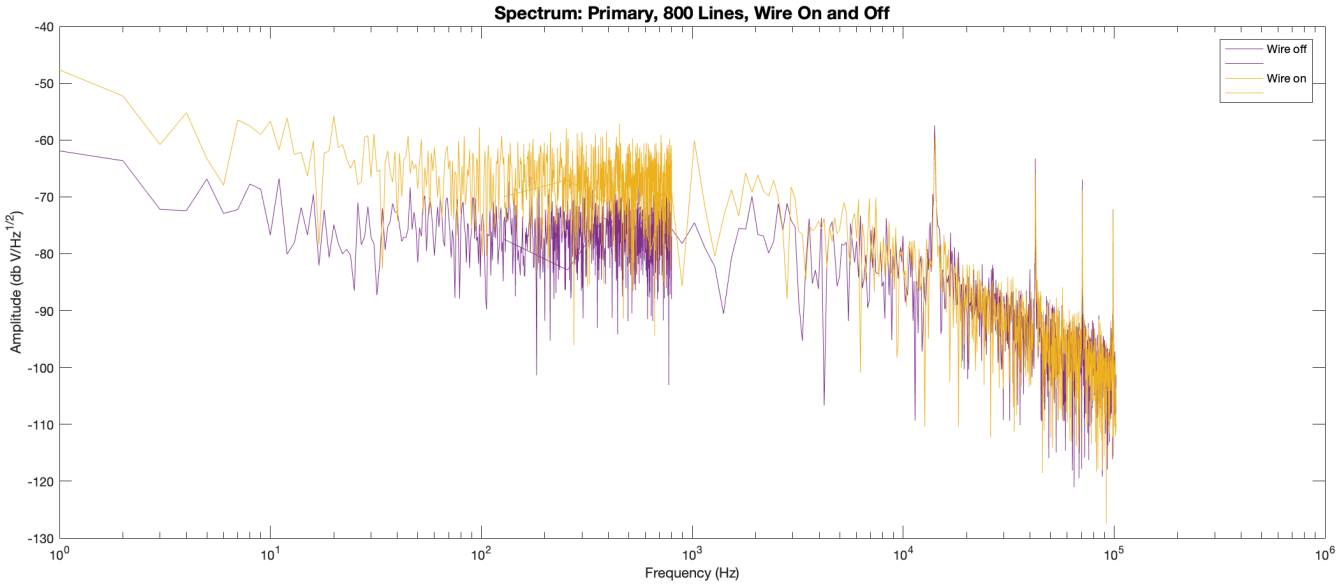


Figure 3.18: Zero primary current noise spectrum, showing the 14kHz and harmonics from the fluxgate clock noise. Purple spectrum shows the noise with the wire for the primary current still inside the detection aperture of LEM 1000-S/SP1 (although the wire has zero current in it), and yellow spectrum shows the noise with the wire on. SR780 Network Signal Analyzer is set to collect 800 frequency lines for each data set.

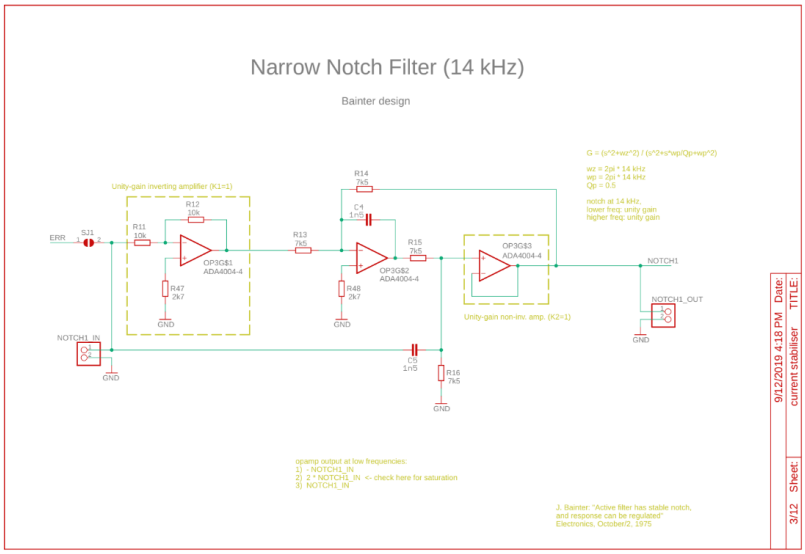


Figure 3.19: Our adaptation of the narrow notch filter from Merkel's design, which is a Bainter notch filter [7]. The deep, narrow notch in the transfer function is adapted to 14kHz.

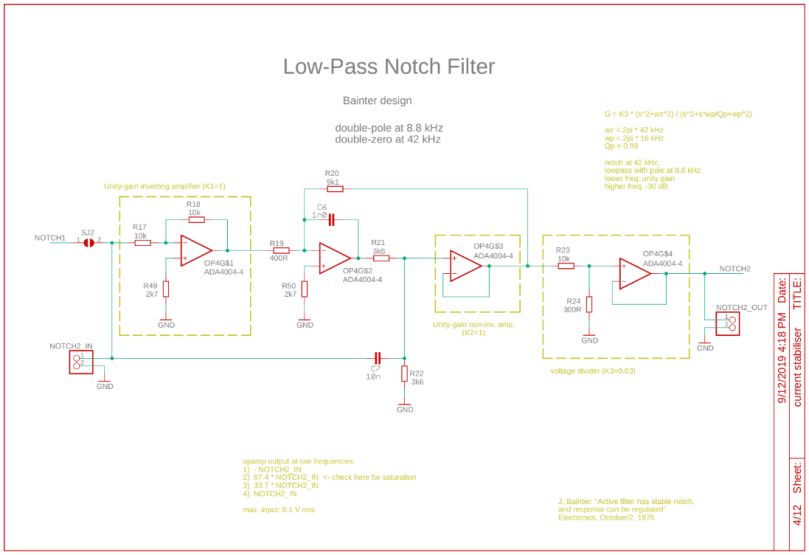


Figure 3.20: Our adaptation of the low-pass notch filter from Merkel's design, which is a Bainter notch filter [7]. The notch from the double-zero in the transfer function is adapted to 42kHz.

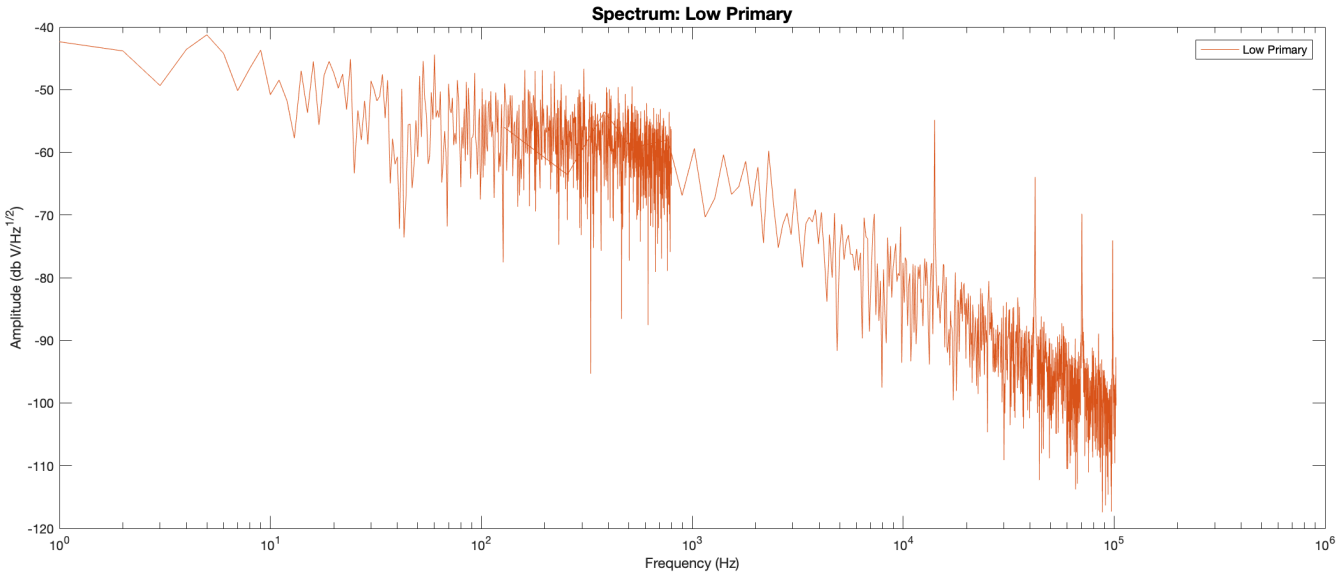


Figure 3.21: Low primary current (34.4A) noise spectrum.

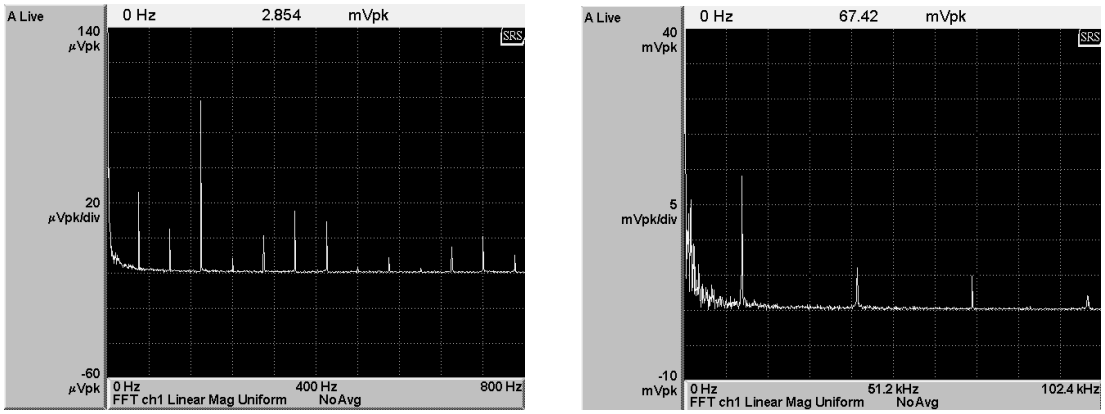


(a) Noise spectrum from DC to 800Hz

(b) Noise spectrum from DC to 102.4kHz

Figure 3.22: High primary current (103.1A) noise spectra in two different frequency ranges, directly from the network signal analyzer.

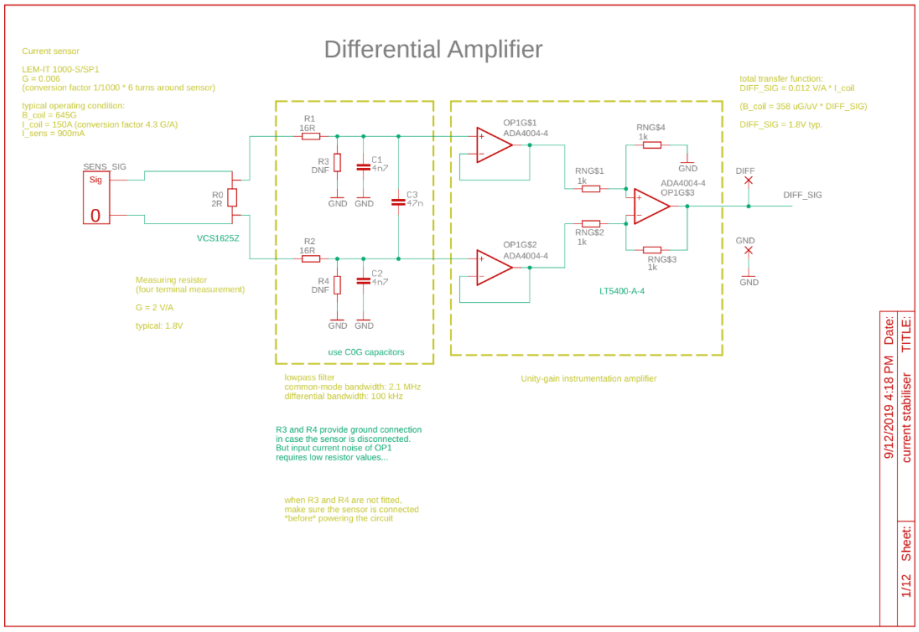


Figure 3.23: Our adaptation of the differential amplifier from Merkel's design [57]. The load resistor is reduced to 2Ω.

with industrial quality Surface-Mount Technology (SMT). Additionally, we employed a PID controller (SRS SIM960) as a tunable component in our feedback loop, as shown in Figure 3.24. We also procured a BeagleBone Black (BBB) single-board computer as a development platform to control the feedback circuit and provide serial communications for setpoint, among other functions, and I wrote python scripts to facilitate these functionalities on BeagleBone Black's Linux system[3]. Eventually, even without winding multiple loops of the primary current around the LEM sensor, we achieved successful active noise cancellation with our feedback engaged for 103.1A primary current, as shown in Figure 3.25. The Root Mean Square noise amplitude analysis with a Region of Interest (ROI) from 4Hz to 3kHz for the magnetic field is shown in Table 3.2, where a conversion factor of 4.335G/A is used; this conversion factor was obtained from our calibration using $^6Li_2$ Magnetic Feshbach Resonance in 2019.

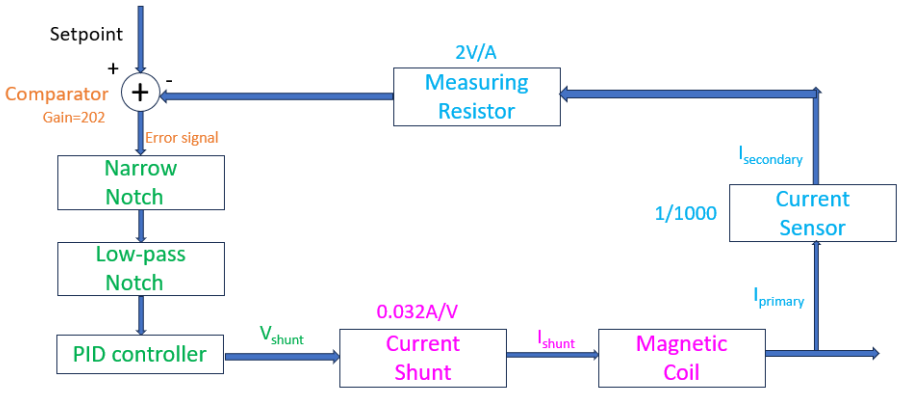


Figure 3.24: Diagram of our feedback circuit setup, with the signal flows and the gains of components labeled.

As demonstrated in Table 3.2, this feedback circuit alone significantly reduced noise from 109 ppm to 9 ppm. The RMS noise with feedback stabilization is a mere 0.6ppm above the noise floor, in stark contrast to the RMS noise with no stabilization, which is 100.6ppm

[3]Thanks to Jarek Kaspar from UW CENPA (Center for Experimental Nuclear Physics and Astrophysics) for helping me learn BBB Linux.

above the noise floor.

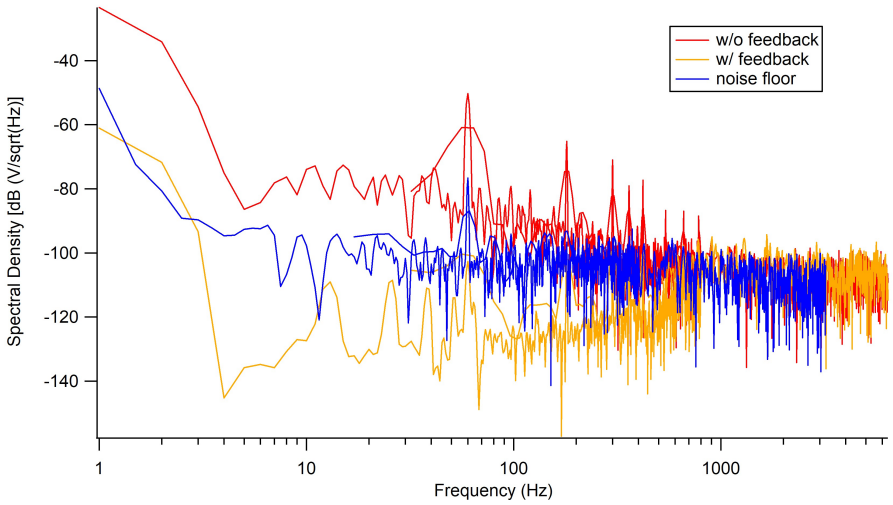


Figure 3.25: Noise spectra showing successful feedback for 103.1A primary current. Red is the noise spectrum without feedback, showing prominent 60Hz and harmonics noise, yellow is the noise spectrum with feedback (the primary current is wound only once through the LEM sensor), and blue is the open-loop noise floor with the primary current set to zero and the feedback disengaged, but the wire is still in the detection aperture of the current sensor. Part of the (yellow) noise spectrum with feedback appears to be below the noise floor (blue) because we are measuring the in-loop error signal; the actual magnetic field noise will not be below the noise floor.

Looking ahead, there is potential [11] to further decrease the RMS noise with feedback to even below 9ppm. Achieving this will necessitate mitigating the effect of the noise floor, which includes contributions from the LEM current sensor and other electronics in the feedback setup, such as amplifiers. A promising approach is the implementation of multi-turn winding [57] of the primary current around the current sensor, which effectively reduces the contribution of the noise. However, this will necessitate a reconfiguration of our water cooling system in the future when the experimental requirements demand B field fluctuation below the noise floor, as discussed below.

The existing electrical connection (Figure 3.26a) of our Feshbach coil begins with a power

| | RMS noise | Dominant noise source |
|---|---|---|
| No stabilization | 48.62mG (109ppm) | Feshbach power supply |
| Feedback stabilization | 4.04mG (9ppm) | Feedback circuitry (filters etc.) |
| Noise floor | 3.76mG (8.4ppm) | Current sensor and amplifiers |

Table 3.2: Table of Root Mean Square (RMS) noise in 103.1A primary current, or 446.9G bias field. The RMS noise with Feedback stabilization is only 0.6ppm above the Noise floor.

supply (current source). A thick solid cable (Cable 1) connects from the positive terminal of the power supply to a custom connector designed by a previous PhD student Anders Hansen [33]. This connector enables the current to flow into a 1/8" square copper cable with a hollow core. This square cable is connected to our water cooling system at both of its ends, with the coolant water flowing through its hollow core to dissipate heat. The length of the square cable is wound around our vacuum chamber in a Helmholtz configuration, forming our magnetic coil for the Feshbach bias field. After the Helmholtz coil section, the square cable connects to another thick cable (Cable 2) via a similar custom connector. This cable (Cable 2) then connects to the negative terminal of the power supply. In this setup, the custom connector, designed by Anders, serves as the electrical junction connecting the thick solid cables to the 1/8" square cable.

To accommodate the multi-turn winding, in 2020, we developed a new design (Figure 3.26b) to add an addition segment of 1/4" round hollow copper pipe to the existing electrical circuit of the coil. Compared to the old design in Figure 3.26a, the connection of Cable 2 to the negative terminal of the power supply will be disconnected. Instead, this end of Cable 2 will be connected to a metallic lug, which is then bolted down the large through-hole on the electrical interface block I designed in Figure 3.27. A 1/4" round hollow copper pipe would be clamped down the trench in the base piece of the interface block by the top piece of the interface block, with 4 screws going through the 4 through-holes; the conductivity of the lug, the electrical interface block and the outer surface of the 1/4" round copper pipe establishes the electrical connection between Cable 2 and the 1/4" round

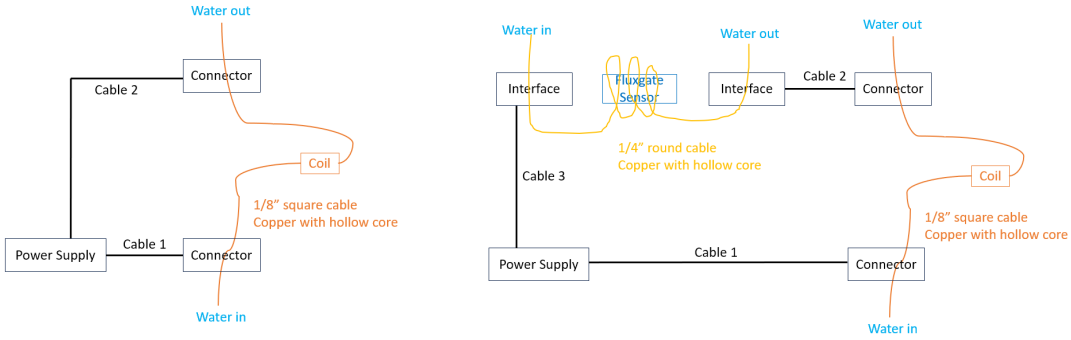


(a) Existing circuit connections for our Feshbach bias magnetic coil

(b) Redesigned circuit connections for multi-turn winding around the fluxgate current sensor.

Figure 3.26: Figure 3.26a shows the existing circuit connections for our Feshbach bias magnetic coil. Cable 1 and Cable 2 are thick solid cables (e.g. 00 AWG or 300MCM), while the coil is made of 1/8" square copper cable with a hollow core, allowing coolant water to flow through. Figure 3.26b shows the redesigned circuit connections for accommodating multi-turn winding around the LEM fluxgate sensor. An additional segment of round cable with hollow core is introduced to allow extra length for winding around the fluxgate sensor. Cable 3 is a thick solid cable, similar to Cable 1 and Cable 2.

pipe. The round cross-section of the hollow copper pipe makes it convenient to join both of its ends to our existing water cooling system using Swagelok or NPT tube fittings. The length of the 1/4" round copper pipe will wind several turns on the LEM fluxgate current sensor, and then be connected to another thick solid cable (Cable 3) using another electrical interface block, and the other end of Cable 3 will then be connected to the negative terminal of the power supply.

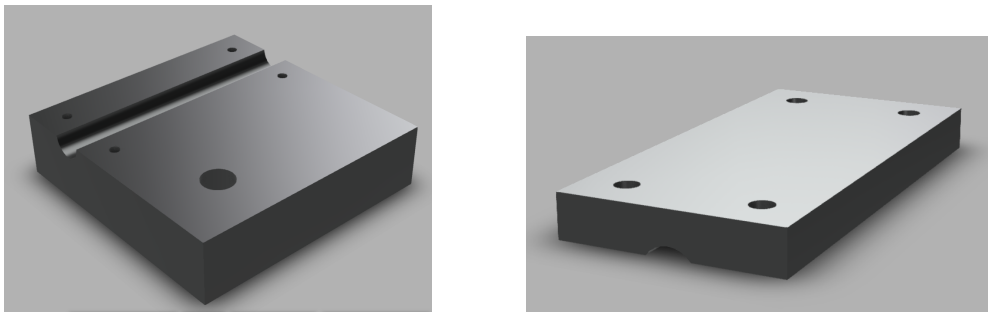

(a) Base piece of watercooling pipe interface in March 2020 redesign

(b) Top piece of watercooling pipe interface in March 2020 redesign

Figure 3.27: Watercooling pipe interface in the March 2020 redesign, facilitating multi-turn winding of the electric current-carrying pipe around the LEM current sensor's detection area. The material is copper. In (a), the base piece measures 2"x0.5"x2" and features four holes designed to mate with corresponding holes in (b), as well as a large hole for attaching the electrical lug to connect the cable. The top piece in (b) has dimensions of 1"x0.2"x2".

*Water cooling system*

During our experiments, our magnetic coils often operate at relatively high currents (over 100A) for extended periods, necessitating water cooling. Our water cooling system [33] includes an inlet from the Physics/Astronomy Building's coolant water supply, which branches off at the entry manifold into several capillary channels. These channels feed into the hollow center of each copper wire that makes up the magnetic coils. After running through the coils, the capillary channels recombine at the exit manifold and exit to the building's

coolant water outlet. For many years, we have struggled with sediment build-up in our system, which damages the flow rate meters, triggers the interlock, and causes experiment downtime due to the replacement of damaged flow rate meters.

On January 30, 2020, while working on the Magnetic Field Stabilization project, I observed that the water manifolds used in our system were made of aluminum and were in physical contact with the brass Swagelok connectors in our system. This configuration immediately reminded me of the galvanic cell reaction in electrochemistry. Upon further research, I discovered that when two metals with different electrode potentials are in physical (and hence electrical) contact and both submerged in the same body of electrolyte (like coolant water without deionization), a process known as galvanic corrosion occurs. This process greatly accelerates the corrosion (rusting) of the more active metal (anode metal). In this case, the inside of the aluminum manifold experienced accelerated corrosion from the ionic attacks in the coolant water driven by the electropotential difference between aluminum and brass, forming the sediments that damaged our flow rate meters.

Armed with this knowledge, I persuaded our team to replace our water manifold with brass ones (Figure 3.28). This change effectively eliminated the sediment issue in our system, and we have not experienced a recurrence since. In addition, the flow rate in our capillary channels have appreciably increased, likely due to the reduction of sediments and hydraulic resistance.

### *3.5 Short pulses for $^6$Li*

In our prior research involving $^{174}$Yb-only bosonic quantum dynamics, the substantial atomic mass resulted in relatively long timescales (e.g. $\omega_{rec}^{-1} = 159.80\mu$s for 1073nm light) for the kicking pulse's width, ranging from 2 to 4 $\mu$s. However, with $^6$Li, which has an atomic mass 29 times lighter than $^{174}$Yb, the timescales (e.g. $\omega_{rec}^{-1} = 2.15\mu$s for 671nm light) are correspondingly shorter, necessitating the need for shorter kicking pulses. The molecular BEC of $^6$Li$_2$ has $\omega_{rec}^{-1} = 4.3\mu$s for 671nm light.

In our previous work with Yb, I developed a method for generating short pulses (2 $\mu$s) separated by long periods (105 $\mu$s) using a combination of National Instruments DAQ cards (controlled by our Cicero time sequence software) and an SRS DS345 function generator.

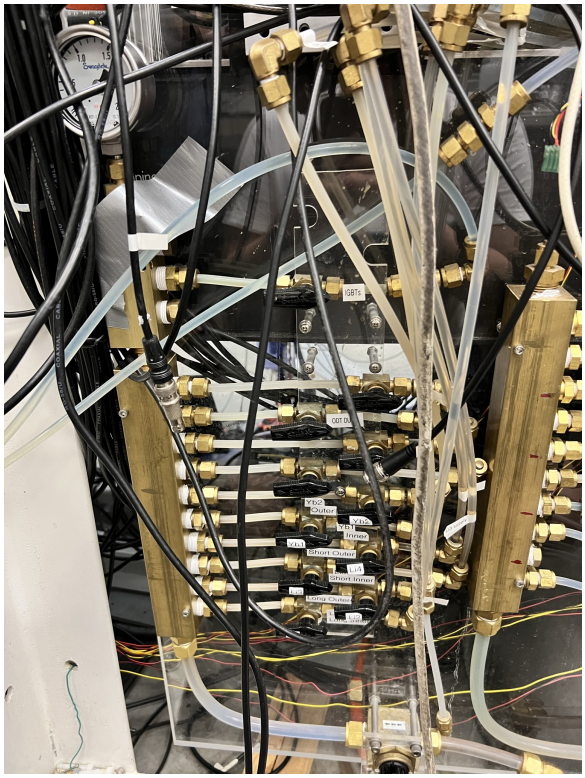

Figure 3.28: Updated Water Cooling System: Transition to an all-brass construction effectively halted the issue of galvanic corrosion that caused sediments often visibly collected at the bends of the plastic tube near the bottom, among other places.

The maximum clock rate for our NI DAQ cards is 200 kHz, which implies that the shortest pulse we can directly generate is 5 $\mu$s. However, since our NI DAQ card is not a variable timebase device, generating hundreds of repetitions of 5-$\mu$s pulses separated by 105-$\mu$s periods would require an impractically long buffer time.

To overcome this challenge and achieve shorter pulses, thereby expanding our scannable parameter space, I utilized the SRS DS345 in "single-cycle burst" mode, with a pre-programmed single pulse stored in its memory, and triggered that pulse with a common square waveform from the NI DAQ card. By programming the SRS DS345 to produce a 2-$\mu$s square pulse upon each rising edge trigger, and setting up the NI DAQ card to produce a continuous square wave at a 105-$\mu$s period (using existing functions in Cicero, like the sign function of a sine function of time), I was able to generate the desired waveform output (Figure 3.29 from [76]). This waveform was then used to control the on/off switch for the RF signal that drives the AOM, which in turn caused the standing wave light potential to flash on/off in a pulsed manner. This is how the pulses were applied for the Many-body Dynamical Delocalization data.

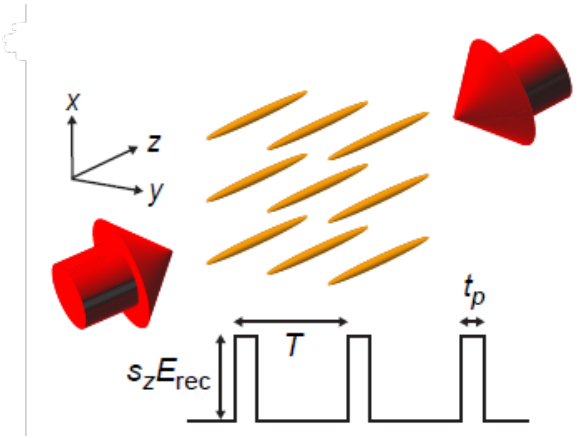


Figure 3.29: Experimental setup for kicked 1D ultracold Yb gas, with $t_p$ ranging from 2 to 4 $\mu$s, and $T$ at 105 $\mu$s. Image adapted from Fig. 1a of [76].

For $^6$Li, however, we require even shorter pulses due to its lighter mass. For a kicking pulse detuned a few nm away from 671nm, $\omega_{rec}^{-1} \approx 2.1\mu$s, in contrast with the 1073 nm

kicking pulse on $^{174}$Yb with $\omega_{rec}^{-1} = 159.2\mu$s. This comparison illustrates the need for a shorter kicking pulse to match the lighter atomic mass of $^{6}$Li, for the kicks to be considered in the "delta kicks" regime.

In our homemade RF drivers, we have traditionally utilized an RF switch (Mini-Circuits ZX80-DR230-S+) to control the on/off of the RF signal, which in turn controls the on/off of the Acousto-Optic Modulator (AOM), and therefore the on/off of the laser lights. This setup was sufficient for our $^{174}$Yb-only bosonic quantum dynamics experiments. However, this switch has a switching time of $2\mu$s, which is insufficient for our current experimental requirements with $^{6}$Li fermions. To induce similar dynamics in paired $^{6}$Li fermions, we needed to upgrade to a faster RF switch, specifically Mini-Circuits ZYSW-2-50DR+ or ZASW-2-50DRA+ (Reflective SPDT, Solid State Switch, DC - 5000 MHz, 50Ω, SMA connector), both having a rise/fall time of 5 ns.

However, these faster RF switches both require a -5V DC power supply, which our existing RF driver box design (from Katie McAlpine) cannot provide. This necessitated a redesign of the RF driver box to accommodate the power requirements of the new RF switch. The following sections detail the modifications and improvements made to the RF driver box to support our experimental needs.

*Redesign of RF driver box*

Throughout the first five years of my work in Prof. Gupta's lab, I gained extensive experience in building and troubleshooting the older design (by Katie McAlpine) of the RF driver box. However, I also identified several issues with the older design, including the unconventional use of a -12V DC power supply as DC ground, which allowed the +12V output of the same power supply to provide an effective +24V. This setup was not ideal, and when the need arose to adapt the older design to accommodate a -5V DC power supply, it presented a great opportunity to address these issues and improve the design.

In this project, Cole and I collaborated to revamp our RF driver design. Our combined efforts led to the successful completion of the project, which improved the functionality of our RF driver box and provided valuable learning experiences for our team. The core

functionality of the RF driver box includes continuous control of the frequency and the amplitude of the RF signal generated, as well as a switch to turn the signal on/off. For all these three controls, we require the flexibility of both a manual control (via a potentiometer for the frequency and the amplitude, and a toggle for the switching) and an external control (via BNC connections). In addition, we require a BNC connector for output RF signal, and an addition auxiliary output for monitoring the RF frequency. Through our revamp efforts, we were able to replace the original (+/-12V) DC power supply to (+/-15V) DC power supply, and set up a -5V voltage regulator on our PCB design (powered by the -15V supply) to accommodate the faster model of RF switch with a rise/fall time of 5 ns, as well as a +12V voltage regulator on our PCB design (powered by the +15V supply) to accommodate the requirements of the Voltage Controlled Oscillators (VCOs), in addition to the existing +5V voltage regulator on our PCB design (powered by the +15V supply) for Voltage Controlled Alternators (VCAs) and the RF switch. We were also able to eliminate the need for +24V DC power supplies, and were therefore able to ground the PCB and the outer aluminum casing to the 0V ground of the (+/-15V) DC power supply.

With the generation of short pulses of RF signals resolved, we now come to addressing the optical engineering aspect of pulse beam generation. Our objective was to achieve a high optical power that could be controlled via an Acousto-Optic Modulator (AOM). A common approach in our lab involved using a diode laser with an output of approximately 20 to 30 milliwatts as a seed, which would then be coupled into a Tapered Amplifier (TA). However, the lifespan of TAs can be unpredictable, with some lasting only a few months. Moreover, in 2022, we faced a global supply shortage of TAs in the 670 nm range.

As mentioned early in this chapter, in 2023, we discovered a new product line of high-power diodes at 675 nm by Ushio (HL67001DG, AlGaInP laser diode with built-in monitor Photodiode)). These diodes offered an impressive output of 200 mW, which was significantly higher than what we had been using, which enabled the pulse beam setup without the use of a Tapered Amplifier, and also helped to more than doubled our Li Zeeman slower light power. The following sections detail my experience with characterizing this high-power diode and setting up an injection lock in the pulse beam setup.

*Ushio diode characterization*

I successfully established the initial injection lock and testing for the high-power laser diode from Ushio as an integral part of the optical system for generating the Li pulse beam (Figure 3.30), with special acknowledgements to Olivia Peek and Cole Williams for their invaluable contributions to the optical layout and alignment in this system. The Li pulse beam setup shares certain similarities with the setup for the Li Zeeman slower light, demonstrating the synergies of our experimental systems. The seed light for the injection lock of the Ushio diode is sourced from a custom-built laser, affectionately named "Neville Longlaser". By manually adjusting the cavity length using a mechanical screw, I was able to identify a combination of diode temperature, diode current, and piezo voltage that provided several GHz of mode-hop-free range while emitting light at 673.3 nm. This light is then elevated using a periscope setup (omitted in Figure 3.30). A pair of cylindrical lenses are employed to adjust the ellipticity of the transverse spatial mode, essentially modifying the beam shape. A compact optical isolator (Thorlabs IO-3D-660-VLP) is used to prevent back-reflection, which could degrade the laser diode. Polarization optics, including a half-wave plate (HWP) and a polarizing beam splitter (PBS), are used to divert a small portion of the optical power, which is then transmitted through a single-mode fiber to a HighFinesse wavelength meter for monitoring the seed's frequency mode. The majority of the seed's power passes through the PBS and enters a single-mode fiber, referred to as the "two-way fiber", as a portion of the slave laser would counter-propagate with this seed beam inside this fiber. After this fiber, the seed passes through a HWP and then reflects off an exposed cube of an Electro-Optic Technology (EOT) isolator, where the seed beam encounters the Ushio diode laser (slave laser). The slave laser light originates from an Ushio diode mounted in a Thorlabs diode mount (Thorlabs LDM56), and travels straight through a HWP and into the EOT isolator. The HWP is optimized to allow maximum slave power through the EOT isolator, but a small portion of the slave light reflects off an exposed PBS cube, and counter-propagates with the seed beam even in the two-way fiber. The majority of the slave diode power, after passing through the EOT isolator, travels through a set of polarization optics, which diverts a small portion of it to be fibered to a Fabry-Perot cavity

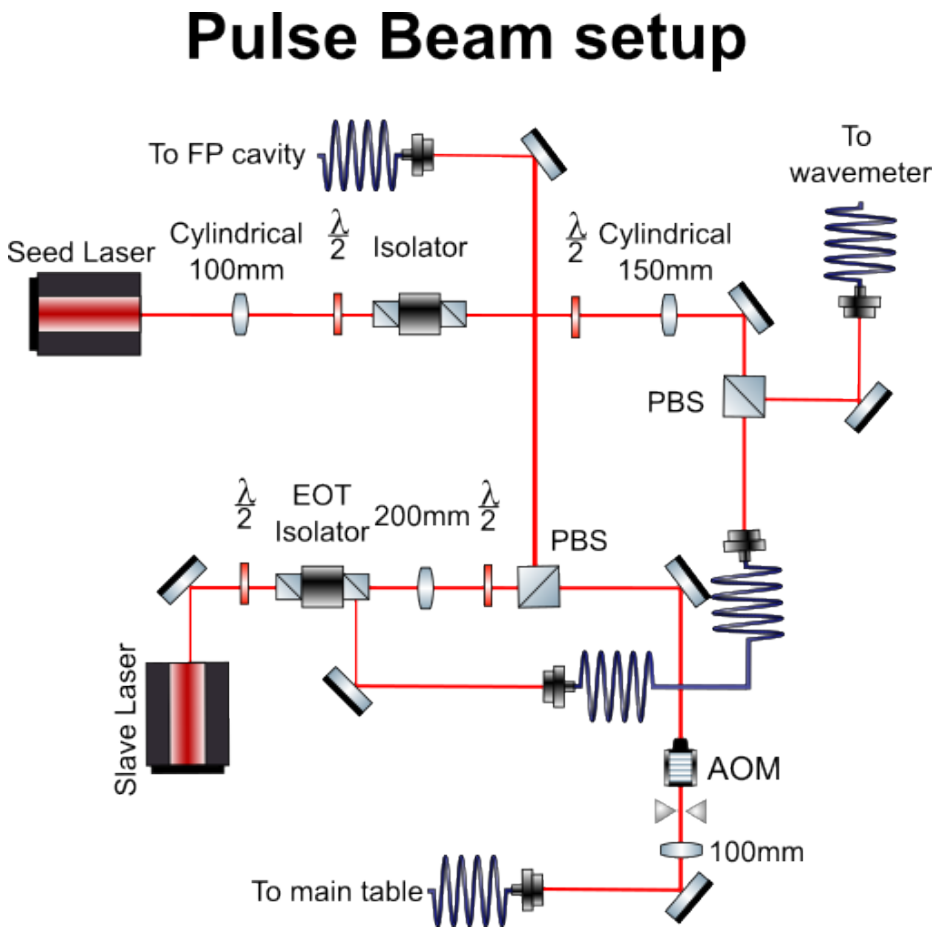


Figure 3.30: Pulse beam optical setup

for monitoring the quality of the injection lock. The remainder of the slave laser, typically exceeding 150 mW of optical power, passes through a single-pass Acousto-Optic Modulator (AOM) setup before being fibered to the main table setup. Note that the use of lens(es) is crucial to reduce the beam diameter at the AOM, not only for the diffraction efficiency of the AOM, but also for the rise/fall time of the optical pulse caused by the on/off of the accoustic wave in the crystal. For $TeO_2$, the rise/fall time comes to approximately 155ns per each millimeter in beam diameter [53].

During my testing and characterization phase, I achieved a slave laser retro-coupling efficiency of 44.7% for the two-way fiber coupling used for injection lock, which is indicative of the spatial mode overlap between the seed and the slave. I also managed to get 4.4 mW seed power at a wavelength of 673.3nm into the slave diode post-isolator.

The Fabry-Perot (FP) cavity transmission signals, represented by oscilloscope traces, near injection locking were observed with a decreasing slave diode current from 219.21mA to 217.57mA to 216.85mA, while the diode temperature remained constant at 13.779kΩ (or 18 °C), as shown in Figure 3.31.

The diode temperature was determined from the resistance of the thermistor (Thorlabs TH10k) used in the diode mount (Thorlabs LDM56), which can be converted to temperature using the following formula: $\mathrm{T(°C)}=(3.354\times10^{-3}+2.514\times10^{-4}\times ln(R/10))^{-1}-273.15$; conversely, to achieve a certain desired temperature, we can use the following formula to calculate the necessary resistance of the thermistor: $\mathrm{R(k\Omega)}=10\times Exp[3977/(T+273.15)-13.339]$. The user manual for this thermistor also provides a plot for this thermistor as shown in Figure 3.32.

The peak heights in the FP scope traces (Figure 3.31) indicate the quality of the lock, with 217.57mA having the highest peak. At this peak, while injected, the slave diode outputs 160mW after the isolator. After this, the polarization optics set diverts about 5mW into a long fiber for reaching FP and providing monitoring for the injection lock. The EOT isolator, after optimizing the preceding HWP, allows about 80% of the slave diode laser power to pass through.

The Ushio diode injection lock hysteresis plot (Figure 3.33) was obtained by monotonically decreasing the diode current from about 225mA down to about 215mA and then raising

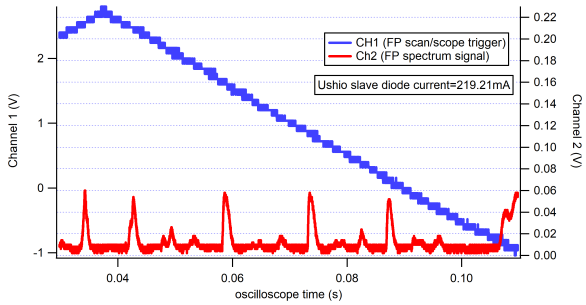


(a) FP cavity transmission signal of the slave diode at 219.21 mA

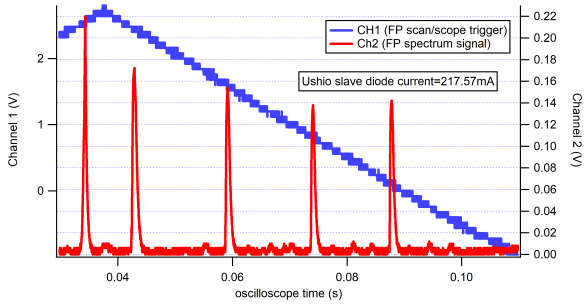


(b) FP cavity transmission signal of the slave diode at 217.57 mA

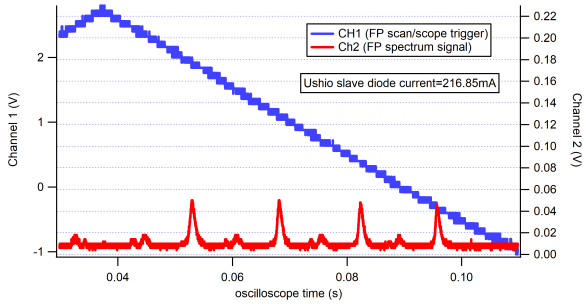


(c) FP cavity transmission signal of the slave diode at 216.85 mA

Figure 3.31: Fabry-Perot cavity transmission signals on oscilloscope of the Ushio slave diode at 18°C case temperature and 4.4mW seed power, with various slave diode currents. Optimal injection lock at 217.57mA with maximum height of the peaks.

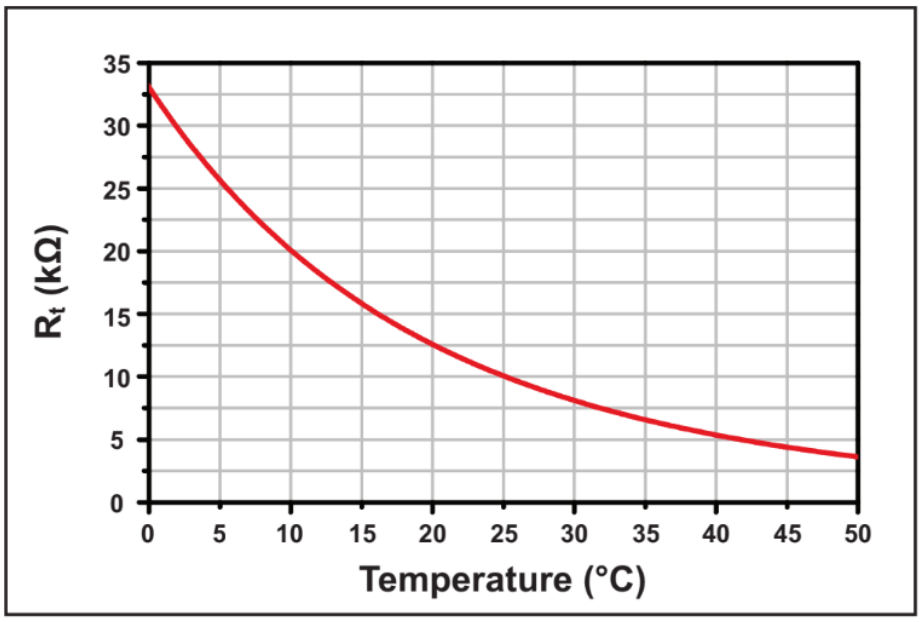


Figure 3.32: Thermistor (Thorlabs TH10k) resistance curve for each temperature, from Thorlabs user manual

it back up, marking each current value at each whole milliwatt power output (measured after the aforementioned polarization optics set). In Figure 3.33, each local minimum point (e.g. 223.01 mA for decreasing current) is a point for good injection lock. Figure 3.34 shows FP signals while decreasing the Ushio slave diode current from 223.47mA to 223.01mA and then 222.89mA. The optimal injection lock at 223.01mA has a maximum height of the peaks, which coincides with the local minimum of slave power output in Figure 3.33.

The injection of seed beam into the slave diode has an overall effect on the slave diode's output power vs diode current relation. For a seed of 4.7mW at 673.4nm, and a slave laser retro-coupling efficiency through the "two-way fiber" of 33%, Figure 3.35 shows the Ushio slave diode's output power for each diode current at a diode case temperature of 18°C.

For lower seed powers, the lasing threshold of the slave diode is characterized in Figure 3.36, with a seed at 673.3nm, and a slave laser retro-coupling efficiency through the "two-way fiber" of 44.7%, and a diode case temperature of 18°C. If we identify the lasing threshold as the slave diode current that produces 0.5mW slave power, then Table 3.3

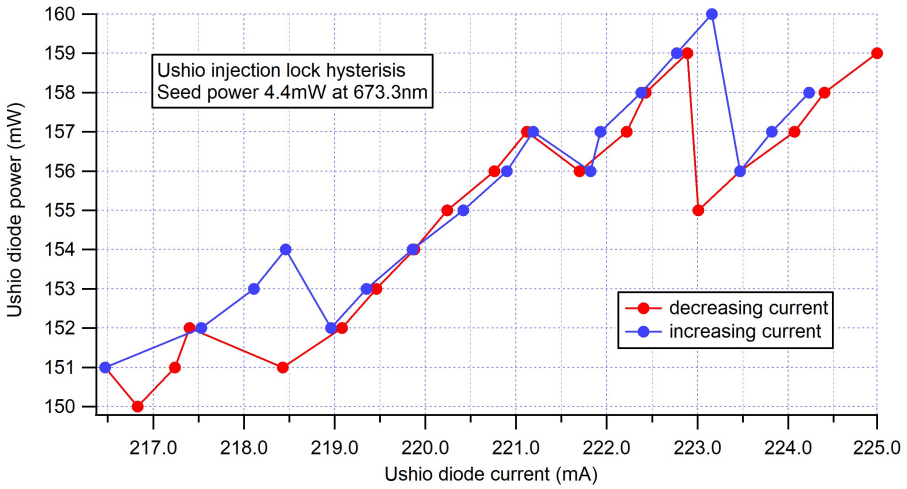


Figure 3.33: The hysteresis plot of the Ushio diode injection lock, depicting the output power of the Ushio slave diode as a function of diode current. The diode was injected with a 4.4mW seed beam at a wavelength of 673.3nm. The measurements were taken after several optical components, including an optical isolator and a Polarizing Beam Splitter (PBS), which result in power loss. Therefore, the actual power output directly from the Ushio slave diode is expected to be higher than the values measured here.

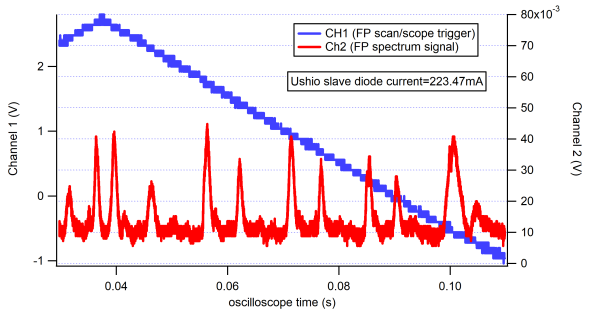


(a) FP cavity transmission signal of the slave diode at 223.47 mA

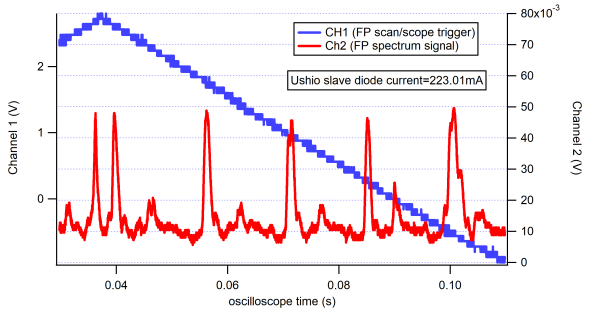


(b) FP cavity transmission signal of the slave diode at 223.01 mA

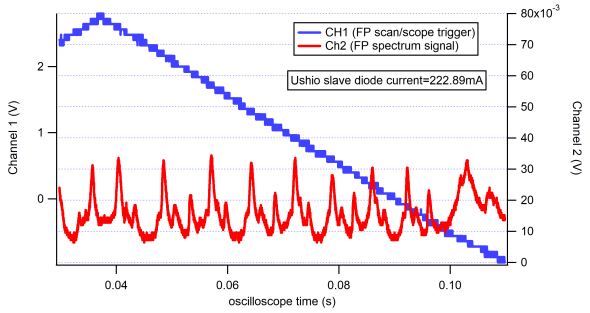


(c) FP cavity transmission signal of the slave diode at 222.89 mA

Figure 3.34: FP signals while decreasing the Ushio slave diode current from 223.47mA to 222.89mA. Optimal injection lock at 223.01mA with maximum height of the peaks, which coincides with the local minimum of slave power output in Figure 3.33.

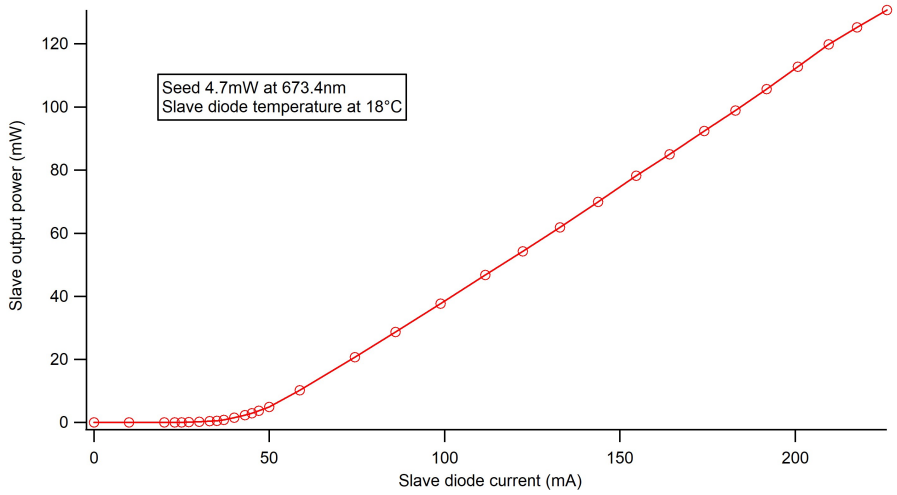


Figure 3.35: The power output of the Ushio diode as a function of diode current. The measurements were taken after several optical components, which result in power loss; the actual power output directly from the Ushio slave diode is expected to be higher than the values measured here. The diode was operating under conditions of strong injection seeding at 4.7mW and 673.4nm, with a slave diode case temperature of 18°C and a retro-coupling efficiency at the "two-way fiber" of 33%.

describes the effect of the different seed power on the lasing threshold for the Ushio slave diode.

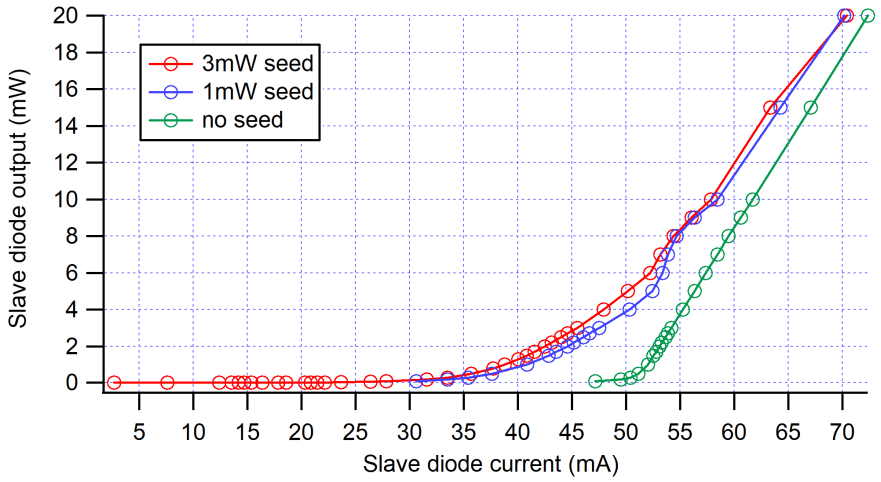


Figure 3.36: Lasing threshold study of Ushio slave diode with different seed injection powers

| Seed Power (mW) | Lasing Threshold (mA) |
|---|---|
| 0 | 51.16 |
| 1 | 37.59 |
| 3 | 35.69 |

Table 3.3: Table of lasing threshold for each seed power. All data sets were taken with a slave diode case temperature of 18°C, a seed at 673.3nm, and a slave laser retro-coupling efficiency through the "two-way fiber" of 44.7%

The slave laser's retro-coupling efficiency through the "two-way fiber" is a crucial indicator of the spatial overlap between the injection seed beam with the slave laser beam, which is vital to a successful injection lock. Figure 3.37 shows this retro-coupling efficiency versus the Ushio diode's current in a free-running mode, i.e. with no seed beam injected at all, at different case temperatures for the Ushio laser diode.

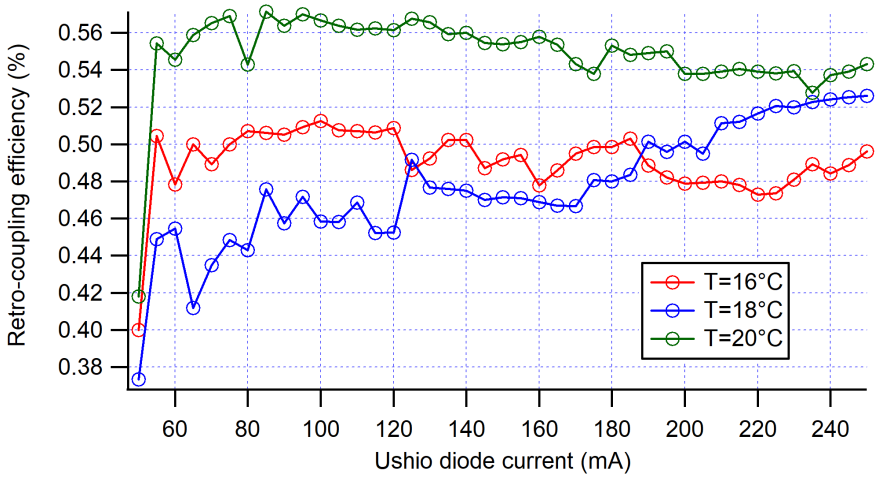


Figure 3.37: Retro-coupling efficiency vs slave current at each case temperature for the Ushio diode

Armed with a thorough understanding of this powerful diode and its capacity for injection locking, we can leverage it in various applications within our experiment. These include its use in the Li Zeeman slower light and the pulse beam. This knowledge allows us to optimize our experimental setup and achieve our research objectives more effectively.

*Optical pulse testing*

In the beginning section discussing short pulses, we referenced the use of the SRS DS345 function generator in "single-cycle burst" mode. This mode allowed us to generate short pulses in response to periodic triggers, a method we employed in our experiments on the bosonic dynamics of $^{174}$Yb. We also discussed how the light mass of $^{6}$Li necessitates even shorter pulses. The DS345's burst mode can produce pulses with a minimum duration of 500ns. An oscilloscope trace of a 500 ns wide, short negative pulse generated by the SRS DS345 function generator is depicted in Figure 3.38.

In this figure, Channel 1 (yellow) represents the single-cycle burst (a negative pulse down to -1V in this figure), while Channel 2 (blue) corresponds to the DS345's internal trigger, used as the trigger source in this case. The width of this internal trigger can vary depending

on the pulse width, but the interval between triggers is manually set on the DS345. This interval also determines the separation period between the single-cycle burst pulses.

The pulse phase can be manually adjusted to generate a positive pulse. Additionally, the amplitude and offset can be configured to comply with the TTL (Transistor-Transistor Logic) standard.

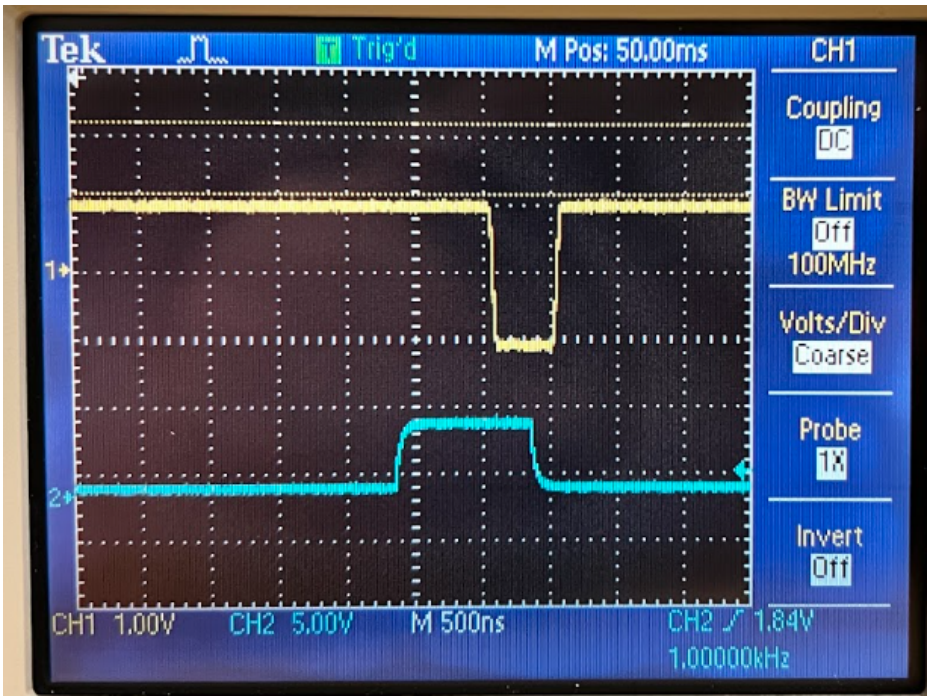


Figure 3.38: Oscilloscope trace of a short negative pulse of 500 ns width, generated by SRS DS345 function generator. Channel 1 (yellow) is the single-cycle burst, and Channel 2 (blue) is the internal trigger of DS345.

With the generation of 500ns electronic pulses and the upgraded RF driver with fast (5ns) RF switches, it is now possible to generate such short optical pulses. However, characterizing extremely short optical pulses, such as those of 500ns duration, requires equipment with ample bandwidth, especially the photodetector. After investigation, I found that a battery-powered, free-space biased detector like the Thorlabs DET36A was not sufficient for our needs. This detector provides a current signal that requires a large load resistance

for sufficient gain. This large resistance, in combination with the junction capacitance, results in a large time constant, slowing the rise/fall time of the photodetector's electronic output signal. However, due to the limited electric power from the battery, reducing the load resistance using sideline terminator resistors significantly reduces the signal amplitude, despite improving the rise/fall time.

In this characterization, I opted for the Thorlabs PDA36A, a cord-powered free-space amplified detector available in our lab's inventory. This detector features a built-in transimpedance amplifier (TIA), which converts the current generated by the photodiode into a voltage. It also includes a switch that allows us to select the gain factor applied in the amplification. However, there is a trade-off: the higher the gain in the TIA, the lower its bandwidth. This is because the amplifier's ability to accurately reproduce the signal decreases as the gain increases, limited by the amplifier's gain-bandwidth product (GBP). At a 40dB gain, according to its User Manual, the detector's bandwidth is a mere 150kHz. Consequently, the detected optical pulse signal is greatly distorted, as shown in Figure 3.39. At 0dB gain, this photodetector has a 10MHz bandwidth, allowing us to more accurately capture the temporal behavior of the optical pulses, as demonstrated in Figure 3.40.

The 500ns limit for square wave pulses in burst mode, imposed by the DS345 function generator, presents a constraint in our experimental setup. Other waveforms, such as the triangle wave, impose even stricter limitations, requiring pulse widths as long as 5 $\mu$s.

However, the DS345 function generator in burst mode can generate 500ns sine wave pulses. By judiciously selecting the amplitude and offset, it is possible to create optical pulses shorter than 500ns. This can be achieved if the portion of the electronic pulse that exceeds the TTL "high" voltage threshold has a reduced duration.

Figure 3.41, Figure 3.42, and Figure 3.43 demonstrate the results of this method. The positive sine wave pulse remains mostly below the TTL "high" voltage threshold, resulting in an optical pulse shorter than 500ns, as measured by the photodiode. It is vital to prevent the electronic pulse from lingering too long in the "indeterminate" voltage region of the TTL standard, as it could impact the waveform stability of the optical pulse, affecting both pulse width and pulse area.

In the three pulse widths achieved with this method, a set of 50 pulses is examined to

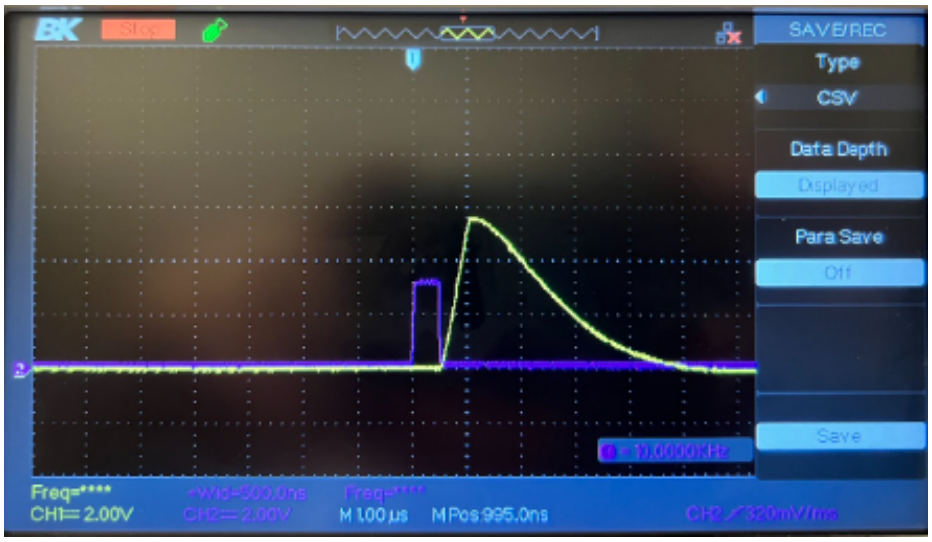


Figure 3.39: 500ns short optical pulse distorted by the photodetector's bandwidth limit of 150kHz. Channel 1 of the oscilloscope (yellow) is the photodiode signal, and Channel 2 (purple) is the 500ns electronic signal from DS345 function generator for the RF switch of the AOM RF driver.

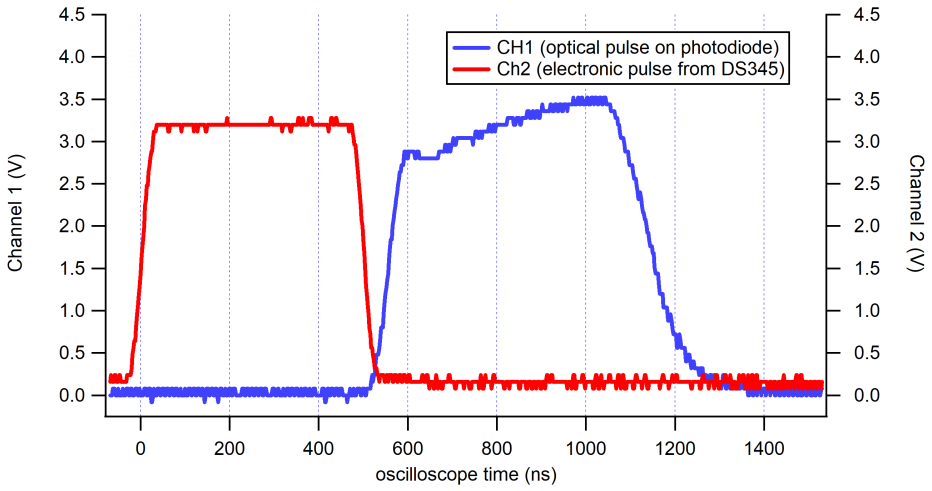


Figure 3.40: 500ns short optical pulse captured by the photodetector with a bandwidth of 10MHz. Channel 1 of the oscilloscope (blue) is the photodiode signal, and Channel 2 (red) is the 500ns electronic signal from DS345 function generator for the RF switch of the AOM RF driver.

measure the fluctuation of the waveforms. This fluctuation is represented by the ratio of the standard deviation over the mean of the pulse width (Full Width at Half Maximum, FWHM) and the pulse area (integrated over the waveform). A trend of decreased waveform stability is observed for progressively shorter pulses.

The fluctuation in the pulse area arises from two factors: the pulse width and the pulse height. The pulse width fluctuation, as characterized by the percentage fluctuation in the FWHM, is attributable to the factors of the pulse generation in the time domain, such as the waveform from the function generator, its duration in the TTL indeterminate region, as well as the photodiode's detection rise/fall time. The pulse height fluctuation, on the other hand, is attributable to signal intensity factors such as the laser beam's intensity fluctuation and photodetector's gain fluctuation (related to its electronic and mechanical stability).

Concerning the pulse center fluctuation, it is negligible and contributes minimally to the kicking period fluctuation. As a fluctuation in the time domain, the pulse center fluctuation measures out to be on the order of the pulse width fluctuation, a few percent of the pulse width itself. Since the kicking period is at least ten times larger than the pulse width (for the delta-kicks regime), the resulting kicking period fluctuation is less than one percent.

For comparison, the 500ns optical pulse in Figure 3.40, produced with the 500ns square-wave electronic signal, exhibits an average FWHM of 497ns with a pulse width fluctuation of 0.38% and pulse area fluctuation of 1.55%. These stability metrics are representative of our successfully concluded Yb 1D QKR experiment and provide a reference for what is considered tolerable within the context of this research.

Looking ahead, given that the RF switch in the redesigned RF box has a rise/fall time as short as 5ns, and the rise/fall time of the optical pulse at the AOM can be further reduced by decreasing the laser beam's diameter, it may be feasible to generate even shorter optical pulses, if required. A promising technology for such applications is Arbitrary Waveform Generators (AWGs), which offer the additional advantage of modulating the amplitude of the optical pulses.

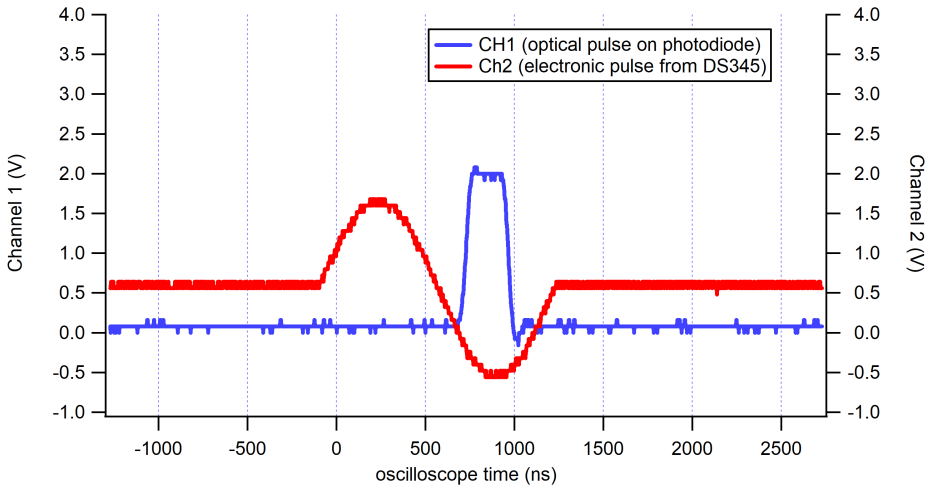


Figure 3.41: 230ns short optical pulse generated by engineering a sine wave from DS345 that spends most of its duration below the TTL "high" voltage threshold, effectively reducing the time duration when the AOM is turned on. Among 50 such pulses, pulse width (FWHM) averages to be 228.02ns, with a fluctuation of 1.47%, and the pulse area fluctuates by 3.06%.

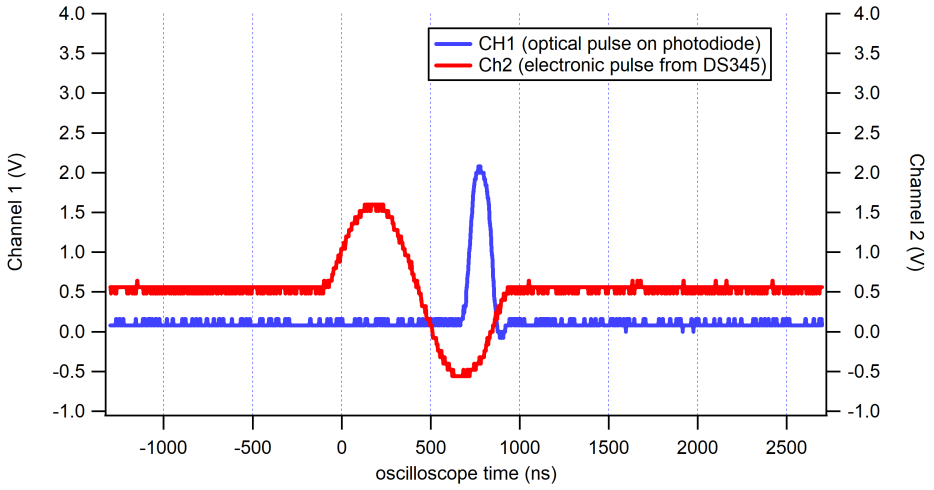


Figure 3.42: 130ns short optical pulse generated by engineering a sine wave from DS345 that spends most of its duration below the TTL "high" voltage threshold, effectively reducing the time duration when the AOM is turned on. Among 50 such pulses, pulse width (FWHM) averages to be 126.68ns, with a fluctuation of 2.50%, and the pulse area fluctuates by 5.38%.

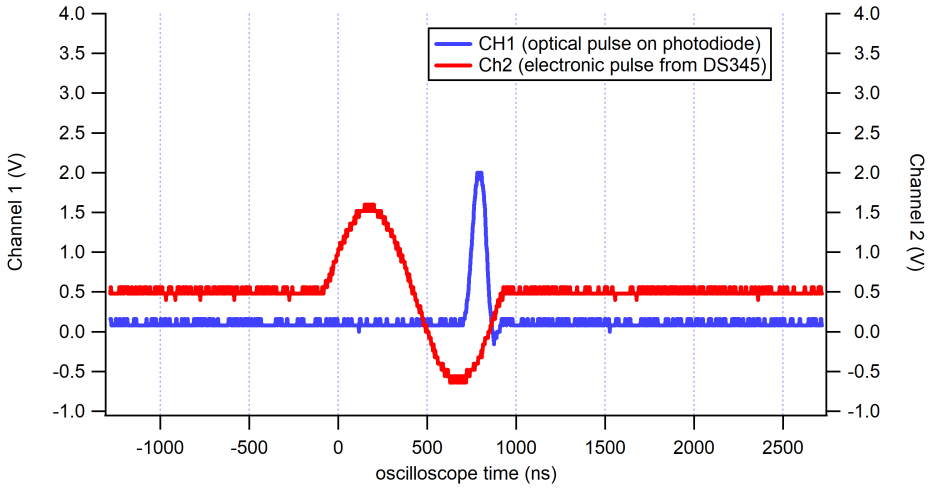


Figure 3.43: 85ns short optical pulse generated by engineering a sine wave from DS345 that spends most of its duration below the TTL "high" voltage threshold, effectively reducing the time duration when the AOM is turned on. Among 50 such pulses, pulse width (FWHM) averages to be 85.12ns, with a fluctuation of 3.49%, and the pulse area fluctuates by 8.25%.

# Chapter 4

# QUANTUM KICKED ROTOR WITH PAIRED FERMIONS

In the preceding chapter, we detailed the technical development of experimental tools for achieving quantum degeneracy with paired $^6$Li fermions and generating short optical pulses to induce system dynamics. Now, we shift our focus to the planned study of Quantum Kicked Rotor (QKR) with Paired fermions. This chapter begins by discussing the motivation behind such a study, linking it to the enduring enigma of many-body transport in quantum systems and its potential applications across various fields. We then delve into the theoretical aspects of how fermion Pairing in quantum degeneracy could influence the dynamical evolution of the system. Lastly, we outline potential future research directions based on our established technical progress.

## *4.1 Motivation for QKR with Paired fermions*

The study of Quantum Kicked Rotor (QKR) with paired fermions holds significant potential for advancing our understanding of many-body physics. The unique properties of fermion pairs, such as their spin statistics and adherence to the Pauli exclusion principle, can greatly influence the dynamics of the QKR. This research has potential applications in various fields including condensed matter physics, quantum information, and quantum simulation. In this section, we delve into these unique properties and discuss the potential implications of our research.

As mentioned in Chapter 2 of this thesis, a spin-mixture of ultracold $^6$Li in State 1 and State 2, depending on their s-wave scattering length, could condense into a molecular BEC of dimers or a BCS superfluid. The behavior of an interacting BEC in an Atom-Optics Kicked Rotor Hamiltonian has recently been actively studied in theory [74] and in experiment with, for example, $^{174}$Yb [76] and $^7$Li [14]. This behavior has been linked to Anderson localization as its quantum simulation in synthetic momentum space [80]. With the aid of optical lattice

potentials, both as static confinement and dynamic kicking pulses for imparting momentum into the BECs, new phenomena such as the Quantum Boomerang Effect (QBE) have been explored as a manifestation of Anderson Localization. The Quantum Boomerang Effect (QBE) [64, 72] occurs for wave packets launched with a finite average velocity when, after an initial ballistic motion, the center of mass of the wave packet experiences a retroreflection and slowly returns to its initial position. In the case of weakly interacting bosons, Janarek et al [43, 42] constructed a universal model with a single parameter of break time for the destruction of the quantum boomerang effect for 1D bosonic gas, independent of the details of the interaction between particles. However, the complexity of fermionic dynamics and fermion Pairing in 1D or higher dimensions has yet not been explored in the context of quantum kicked rotors, and open questions remain regarding the localization condition and the existence of pre-thermal states in fermionic superfluids with strong many-body interactions.

Moreover, in 2022, by engineering the amplitude modulation of the kicking pulses, our team has achieved the quantum simulation of the 3D Anderson model using $^{174}$Yb bosons in a 1D gas [80]. We have observed the effect of many-body interaction shifting the Metal-Insulator Transition boundary in the phase diagram. This raises the question: what would the amplitude-modulated kicks do to $^{6}$Li fermions in a 3D gas? As we will discuss in the next section, the fermion Pairing Energy is likely to play a significant role. Given that we can have either negative or arbitrary positive s-wave scattering length between State 1 and State 2 $^{6}$Li atoms (Figure 2.3), we have a vast parameter space to explore.

The Atom-Optics Kicked Rotor provides a fertile ground for studying quantum chaos, the interplay between chaos and quantum interference effects. With the experimental methods of optical pulse engineering and interaction tuning via an external magnetic field, we can delve deep into the study of quantum transport in the presence of fermion Pairing and mBEC-BCS crossover. This could potentially shed light on the enduring enigma of fermionic superconductivity and strongly correlated fermionic systems.

### *4.2 Pairing mechanism of fermions and Quantum Kicked Gas*

This section delves into the theoretical underpinnings of how fermion Pairing in Quantum Degeneracy can influence the dynamics of a quantum kicked gas. Initially, we explore the physics of fermion Pairing in superfluids and the continuous spectrum of the BCS-BEC crossover. We then probe into the mechanisms of excitation in fermionic superfluids, specifically focusing on the prerequisites to remain beneath the threshold of pair-breaking. Finally, we address the experimental parameters that need to be meticulously considered to ensure we stay below the pair-breaking limit for our Quantum Kicked Gas composed of paired fermions.

The review study by Ketterle and Zwierlein in 2008 [46] clarifies that in a three-dimensional environment, two isolated fermions can form a molecule given a sufficiently strong attractive interaction. The system's ground state is expected to be a Bose-Einstein condensate composed of these tightly bound pairs. However, as the density of particles in the system increases, the Pauli pressure of the fermionic constituents becomes significant, thereby altering the system's properties. When the Fermi energy surpasses the molecules' binding energy, the system's equation of state is expected to exhibit fermionic characteristics, meaning the chemical potential will be directly proportional to the density raised to the power of 2/3. The fermionic nature of the constituents becomes inconsequential only when the molecules' size is considerably smaller than the spacing between particles, that is, when the binding energy greatly surpasses the Fermi energy. In such a scenario, the tightly bound fermions are broadly dispersed in momentum space, thereby avoiding the Pauli restriction of one occupation per momentum state.

In the case of a weak attraction, no bound state exists for two isolated fermions. However, Cooper pairs can form in the presence of a Fermi sea, as previously mentioned in Chapter 2. The system's ground state is found to be a condensate of Cooper pairs, as outlined by BCS theory. Unlike the physics of molecular condensates, the binding energy of these pairs is significantly lower than the Fermi energy, making Pauli pressure a key factor.

As mentioned in Chapter 2, the BEC-BCS crossover is a smooth transition, and we can use the s-wave scattering length $a_s$ between State 1 and State 2 Li atoms as the tuning

parameter for our discussion in this section. For positive $a_s > 0$, a two-body bound state exists at $E_B = -\frac{\hbar^2}{ma_s^2}$; for small and negative $a_s < 0$, the weak attraction lead to Cooper pair formation. In both cases, the orbital component of the pair's wave function will be symmetric under exchange of the paired particle's coordinates. If we define the Fermi wave vector $k_F = (3\pi^2 n)^{1/3}$ and the Fermi energy $E_F = \hbar^2 k_F^2/2m$, where $n$ is the number density of the fermions and $m$ the mass of each fermion, then following the variational method in [46] and neglecting interactions between pairs at finite momentum, we arrive at the following results:

1. In the BCS limit, characterized by a weak attractive interaction ($k_F a_s \to 0_-$), the chemical potential $\mu$ is approximately equal to the Fermi energy $E_F$. The superfluid gap in the energy spectrum, denoted by $\Delta$, is given by $\Delta \approx \frac{8E_F}{e^2} e^{-\pi/2k_F|a_s|}$. In this scenario, Pauli blocking takes precedence over interactions, and new particle pairs can only be added at the Fermi surface. The superfluid gap $\Delta$ exceeds the bound-state energy for a single Cooper pair atop a non-interacting Fermi sea, as the entire particle ensemble participates in the pairing. However, the gap remains exponentially smaller than the Fermi energy, signifying the vulnerability of this Cooper pairing.

2. In the BEC limit, characterized by tightly bound pairs ($k_F a_s \to 0_+$), the chemical potential $\mu$ is given by $\mu = -\frac{\hbar^2}{2ma_s^2} + \frac{\pi\hbar^2 a_s n}{m}$, and the quantity $\Delta$ is approximated by $\Delta \approx \sqrt{\frac{16}{3\pi}} \frac{E_F}{\sqrt{k_F a_s}}$. The first term in the chemical potential represents the binding energy per fermion in a tightly bound molecule, while the second term signifies a mean-field repulsive interaction between the molecules in the gas. In the BEC regime, the single-fermion excitation spectrum loses its gap as soon as $\mu < 0$. Instead, $\Delta^2/2|\mu| = 4\pi\hbar^2 n a_s/m$ embodies the mean field energy experienced by a single fermion in a gas of molecules.

3. In the BCS-BEC crossover continuum, the occupation of momentum states transitions smoothly from the step-function of a degenerate Fermi gas (broadened over a width $\Delta \ll E_F$ due to pairing), to the state where all bosonic molecules occupy the identical momentum distribution.

When kicked by pulsed optical lattice beams, fermionic superfluids can be excited in two ways: Fermi-type excitations of single atoms or Bose-like excitations of fermion pairs. The first is related to pair breaking, the second to density fluctuations — sound waves. For QKR with paired fermions, we primarily want to stay in the Bose-like excitation of fermion pairs to study the quantum transport of such pairs in the long-time limit, so we should ensure that the kinetic energy imparted is below the gap to excitation. As we tune the s-wave scattering length from a large negative value to nearly zero (Feshbach resonance), the superfluid gap to excitation $\Delta$ reduces in an exponential manner, which makes it harder and harder to stay below pair-breaking.

In our completed Quantum Kicked Rotor (QKR) experiments with $^{174}$Yb bosons [76], we modeled the interacting bosons using the nonlinear Gross-Pitaevskii Equation for Atom-Optics Kicked Rotor:

$$i\bar{k}\partial_\tau \Phi(\theta,\tau) = \left( -\frac{\bar{k}^2}{2}\partial_\theta^2 - K\cos\theta \sum_{n_p} \delta(\tau - n_p) + \frac{1}{2}\omega_\theta^2\theta^2 + g|\Phi(\theta,\tau)|^2 \right) \Phi(\theta,\tau) \qquad (4.1)$$

where $\theta = 2k_L z$ and $\tau = t/T$ are dimensionless variables of the QKR wavefunction $\Phi$, and the experimental parameters were incorporated by introducing dimensionless parameters such as the kicking strength $K = 4s_z\omega_{rec}^2 t_p T$, and the effective reduced Planck constant $\bar{k} = 8\omega_{rec}T$, parameters that are conventionally used in the Atom-Optics Kicked Rotor Hamiltonian, and the interaction constant $g = \bar{k}^2 \frac{k_L a_s}{(k_L a_\perp)^2}$, where $a_\perp = \sqrt{\hbar/m\omega_\perp}$ is the transverse harmonic oscillator length and $\omega_\perp = 2\sqrt{s_\perp}\omega_{rec}$ is the transverse trap frequency, and a typical $s_\perp$=106 was used. These dimensionless parameters in the theoretical model are adjustable by modifying the experimental parameters such as kick period T, pulse width $t_p$, and the depth of the kicking lattice potential $V_{lat} = s_z E_{rec}$. The recoil frequency for $^{174}$Yb for the 1073nm kicking pulse beam was at $\omega_{rec} = 2\pi\times$0.996kHz, resulting in a Talbot time of $\pi/(2\omega_{rec}) = 251\mu$s. For our study, since the clock rate of the National Instruments DAQ card we used was 200kHz, we chose a kicking period of T=105$\mu$s to be incommensurate with the Talbot time, which corresponds to $\bar{k}$ =5.26. We studied a range of kicking strengths, from K=1.3 to 5.3, and adjusted the dimensionless interaction strength $gn_{1D}$ from 3.9 to 18.7, where $n_{1D} = \bar{n}_{1D}/2k_L$ is the intial 1D peak density of atoms parametrized by the

laser's wavevector. The variation in interaction strength was achieved by manipulating the transverse confinement of two orthogonal static optical lattice beams, thereby demonstrating the influence of many-body interaction on the dynamical localization/delocalization of the kicked 1D boson gas.

This formalism and experimental setup is equally applicable to a molecular Bose-Einstein Condensate (BEC) of $^6Li_2$ dimers, and parameters like the kicking strength $K$ and effective Planck constant $\bar{k}$ remain pertinent when analyzing the behavior of superfluids even in the BCS regime. Assuming a kicking pulse beam at 673nm, noting that the dimer has a mass of m=12 a.m.u. (atomic mass unit), the recoil frequency for $^6Li_2$ would be $\omega_{rec} = 2\pi\times$36.7kHz, resulting in a Talbot time of $\pi/(2\omega_{rec}) = 6.81\mu$s. Assuming a pulse width of $t_p$=200ns ($\ll \omega_{rec}^{-1} = 4.34\mu$s), we can plan to use a kicking period of T=2.85$\mu$s ($\bar{k}$ =5.26) that is incommensurate with the Talbot time and also satisfies "delta-kicks" regime. As discussed in Chapter 2, since the red detuning of 673nm kicking pulse beam is $\Delta$=1.328THz ($\ll$446.8THz=$\frac{c}{671nm}$), the Rotating Wave Approximation applies, and therefore $V_{lat} = \frac{\hbar\Gamma^2}{8\Delta}[I_0/I_{sat}] = \frac{\alpha(\lambda_L)}{2\varepsilon_0 c}I_0$. With large detuning, $I_{sat}$ =2.54mW/cm$^2$, and therefore $\frac{\alpha(\lambda_L=673nm)}{2\varepsilon_0 c} = 8.46\times10^{-35}$m$^2$s for a single $^6$Li atom; for the dimer $^6Li_2$, this will be $1.692\times10^{-34}$m$^2$s, or $2.554\times10^{-3}\,h\times$kHz per mW/cm$^2$. A kicking strength K from 1.3 to 5.3 would then require $s_z$ to range from 10.72 to 43.72, and therefore requires the kicking pulse beam's peak intensity $I_0$ to range from $1.54\times10^5$mW/cm$^2$ to $6.28\times10^5$mW/cm$^2$. If we have Gaussian beam waist of 100$\mu$m, we would need an optical power ranging from 24.2mW to 98.6mW in our kicking pulse beam.

With the use of two orthogonal static optical lattice beams for transverse confinement, the $^6Li_2$ dimers could form 1D tubes. To compare, for $^{174}$Yb, the large detuning of 1073nm lattice light invalidates the Rotating Wave Approximation; therefore, the contribution from counter-rotating term of the $^1S_0 \rightarrow {}^1P_1$ transition (398.9nm, $\Gamma = 2\pi\times$27.9MHz, $I_{sat}$ =57mW/cm$^2$) has to be included. As a result, for $^{174}$Yb, $\frac{\alpha(\lambda_L=1073nm)}{2\varepsilon_0 c} = 3.59\times10^{-37}$m$^2$s, or $5.42\times10^{-6}\,h\times$kHz per mW/cm$^2$ of laser beam peak intensity. A similar calculation for a single $^6$Li atom, accounting for counter rotating terms, results in $\frac{\alpha(\lambda_L=1073nm)}{2\varepsilon_0 c} = 8.26\times10^{-37}$m$^2$s, 2.30 times that of the $^{174}$Yb. Within the dimer $^6Li_2$ as a very weakly bound molecule (Feshbach molecules being the least vibrationally bound state), the atoms

are almost free, approximately retaining their atomic electronic structure. As a result, the optical dipole potential experienced by the dimer $^6Li_2$ can be approximated as twice that of each $^6$Li atom[89, 32, 45, 44], leading to a total value 4.60 times that of $^{174}$Yb. Consequently, the recoil frequency of the dimer molecule for 1073 nm light is given by $\omega_{\text{rec}} = 2\pi \times 14.44$ kHz. Assuming the same parameters of the 1073nm optical lattice beams used in our $^{174}$Yb experiments, the typical $s_\perp$=106 for $^{174}$Yb would be $s_\perp$=33.6 for the dimer $^6Li_2$, with $\omega_\perp = 2\pi\times$167kHz and $a_\perp$ =71.0nm [35, 48, 47]. As calculated in [63], the s-wave scattering length between $^6Li_2$ dimer molecules is simply $a_{DD} = 0.6a_{12}$, where $a_{12}$ is the scattering length between individual fermion atoms in State 1 and State 2, as plotted in Figure 2.3 for different external magnetic fields. The capability of controlling dimer-dimer interactions with an external magnetic bias field presents a unique opportunity to broaden our reach in the parameter space of the 1D Quantum Kicked Rotor. This is especially pertinent for exploration in the Tonks-Girardeau (TG) gas where $\gamma = E_{int}/E_{kin} = (l_c\bar{n}_{1D})^{-2} \gg 1$, since the correlation length $l_c = \hbar/\sqrt{m\bar{g}\bar{n}_{1D}}$ and the mean-field interaction constant $\bar{g} = 2\hbar^2 a_s/(ma_\perp^2)$ both depend on the s-wave scattering length. Depending on the 1D number density $\bar{n}_{1D}$ experimentally achieved and measured in the system, with careful preparation of the external magnetic field, strong attractive interactions can be achieved to potentially access the TG gas regime. The influence of external magnetic fields on these interactions further expands the possibilities for experimental control and exploration.

In the BCS region, a crucial technical consideration is the need to maintain moderate laser power to ensure that the imparted kinetic energy stays below the pair-breaking threshold, thereby preserving the integrity of the fermionic pairs. This approach allows us to explore the rich dynamics of fermionic superfluids under the influence of external perturbations, contributing to our understanding of quantum many-body systems.

### *4.3 Progress and Future Pathways*

The path to achieving a Fermi degenerate gas is intricate and filled with challenges. However, our progress thus far has established a solid groundwork for reaching this goal and unlocking its full potential. As detailed in Chapter 3, we have successfully implemented laser trapping

and cooling, sub-Doppler cooling, and Optical Dipole Trapping of $^6$Li. Furthermore, we have set up the necessary electronic and optical systems for pulsing standing waves. These pivotal achievements pave the way for our exploration of Quantum Kicked Rotor (QKR) dynamics with paired fermions.

Building on the progress we have made in developing experimental tools for many-body fermionic dynamics, our immediate focus is on the evaporative cooling of the spin mixture. This is a critical step towards achieving a Fermi degenerate gas. Once a sufficient number of atoms are captured in the Optical Dipole Trap, we will prepare an even mixture of State 1 and State 2 $^6$Li atoms using Landau-Zener pulses to address the transition in the RF range, as detailed in Chapter 3. Following the preparation of the spin mixture, we will initiate the evaporative process. This involves "spilling" hot atoms by lowering the ODT potential depth, accompanied by rethermalization due to sufficient s-wave scattering. After the evaporative cooling process, we will measure the temperature of the resulting atomic cloud through absorption imaging after a Time-of-Flight. The spatial distribution of the atom number density will be fitted to determine the population of atoms in the degenerate Fermi gas and the fraction in the surrounding residual thermal cloud.

Upon achieving and characterizing the degenerate Fermi gas, we will apply magnetic bias field to control the s-wave scattering length (and therefore the interaction) between State 1 and State 2 $^6$Li atoms, as well as pulsed standing waves of far-detuned laser (as detailed in the final section of Chapter 3) to induce quantum dynamics in the ensemble and observe the evolution of its kinetic energy distribution. This will set the stage for Quantum Kicked Rotor with Paired fermions.

By employing static optical lattice beams for two-dimensional confinement, we aim to explore QKR dynamics with paired fermions in 1D. This approach mirrors our completed research with $^{174}$Yb bosons. With the capability of amplitude modulation on the optical pulses, we can also simulate long-range interacting fermions in the synthetic momentum lattice, providing insights into strongly correlated fermionic systems.

Leveraging the development of Spatial Light Modulation (SLM) using Digital Micromirror Devices (DMDs), we have achieved ring-shaped laser beams. The flexibility of DMDs also allows us to engineer a box trap by cancelling out the harmonic confinement from Gaus-

sian beams. We plan to use the non-trivial topology of a ring trap to study dual-superfluid phenomena like entrainment, and the absence of harmonic confinement in a box trap to study the behavior of QKRs in the extremely long-term limit, and extract key parameters like the diffusion exponent of the kinetic energy growth. The progress and future directions of these developments will be the focus of the following chapter.

In conclusion, this chapter has provided a detailed account of our ongoing efforts and future plans in the study of Fermi degenerate gas and Quantum Kicked Rotor dynamics with paired fermions. Our research, while a small part of the vast field of many-body fermionic dynamics in quantum degeneracy, is a testament to the collective efforts of the scientific community. The progress we have made and the paths we aim to tread not only add to our specific area of study but also contribute to the broader field of ultracold atomic physics. As we continue our research, we humbly acknowledge the vastness of the unknown and remain dedicated to incrementally expanding our understanding within this complex and rapidly evolving field.

# Chapter 5

# DMD AND RING TRAP

## *5.1 Complex Patterned Traps: Boundless Opportunities*

Our laboratory has been a nurturing environment for innovative discoveries and unique contributions within the field of ultracold atoms, largely enabled by the Gaussian beams of our various laser systems. As we look towards the future, we find ourselves drawn to explore beyond the confines of Gaussian laser beams, motivated by the vast possibilities that complex patterned traps offer. The application of Spatial Light Modulation (SLM) described in this chapter supports a solid and versatile technical foundation for future explorations.

The necessity for non-trivial topologies, such as ring traps, stems from the need to sustain superfluid flow in our group's proposed examination of entrainment in dual-superfluid systems; a subject we will explore in depth in the subsequent section. However, the opportunities offered by spatially engineered trap geometries are virtually boundless.

Ring traps, in particular, provide a unique platform for studying single-superfluid effects. The Josephson effect, a quantum mechanical phenomenon that allows supercurrent to tunnel between two weakly linked superconductors or superfluids, is a fundamental aspect of superfluid physics. In the context of ultracold atoms, this effect can be observed in ring-shaped traps, where a weak link or barrier is introduced to create two interconnected superfluids, and achieve an atom SQUID (superconducting quantum interference device) [71]. The supercurrent that flows across this barrier is a direct manifestation of the Josephson effect.

Moreover, the ring trap geometry allows for the observation of phase slips [85], topological defects that occur when the phase of the superfluid order parameter changes by $2\pi$, causing a discontinuity in the supercurrent with respect to the changes in the driving parameter (e.g. stirring speed of the barrier [85]). Phase slips can occur when the supercurrent

exceeds a critical value, leading to a sudden change in the superfluid's momentum. This phenomenon is closely related to the concept of vorticity in superfluids and plays a crucial role in the dynamics of superfluids in ring traps. Additionally, ring traps provide a unique platform for observing matter wave interference, such as the quantization of orbital angular momentum around the ring [49]. Furthermore, when a barrier is introduced in a ring trap, the superfluid is effectively split into two separate superfluids. When the barrier is removed, the two superfluids can interfere, creating an interference pattern that can be observed in the density profile of the superfluid. This matter wave interference is a direct consequence of the wave-like nature of particles in quantum mechanics and provides a powerful tool for studying the phase coherence and dynamics of superfluids.

In our completed experimental exploration of the many-body Anderson Metal-Insulator Transition using kicked quantum gases [80], we examined the effect of the inhomogeneous harmonic trap on the long-term behavior of the kicked quantum gases of ytterbium. This complexity affected the diffusion exponent $\alpha$ of the long-term kinetic energy growth. Recent studies have shown [59] that a carefully designed repulsive potential can counterbalance the harmonic potential produced by a Gaussian laser beam, thereby creating an optical box trap. This allows for precise extraction of many-body quantum transport coefficients, exponents, and other parameters even in the long-term limit. This is particularly advantageous for comprehensive studies involving Quantum Kicked Rotors for Bose-Einstein Condensates (BECs), Tonks gas, and paired Fermions, as well as for enhancing momentum-space lattices experiments.

As we continue to develop and refine our experimental techniques, we look forward to uncovering new insights into the behavior of ultracold atoms in these novel trap geometries.

### *5.2 Investigating Entrainment in Dual-Superfluid Systems*

The phenomenon of superfluid entrainment, also known as the Andreev-Bashkin effect, was first hypothesized by Andreev and Bashkin for mixtures of superfluid $^3$He and $^4$He. This intriguing concept, where one superfluid induces flow in another superfluid without any viscous drag or dissipation, has been a subject of scientific curiosity for nearly five decades [3, 82]. Superfluid entrainment plays a pivotal role in the dynamics of superfluid

mixtures, finding relevance in diverse fields such as neutron stars (as a potential explanation for Pulsar Frequency Glitches) [15, 4], nuclear physics [12], and cold atoms [60, 62]. This effect is attributed to the current-current coupling between the two superfluids (in contrast with the density-density interactions), and extends beyond the scope of mean-field theory. Despite the wealth of research dedicated to this topic, the direct experimental observation of this effect remains a challenging endeavor.

The experimental protocol proposed by our Principal Investigator Prof. Gupta and theory collaborators in [35] is focused on the direct detection of this effect. The proposal employs a ring geometry, which provides a unique advantage in the study of entrainment, in that a persistent flow can be induced in a ring-trap without any variation of the density distribution, effectively inhibiting the density-density interaction to allow the current-current interaction to manifest as entrainment signal. Cold-atom systems, such as a two-species mixture of superfluid $^6$Li and $^{174}$Yb, serve as an ideal platform for this investigation, offering unparalleled control over both geometry and interactions. The adoption of a ring geometry specifically allows for the induction of persistent flow in a superfluid without causing any density fluctuations. This approach effectively eliminates variations in the stronger mean-field interaction, which often obstructs the detection of entrainment in other geometrical configurations.

The proposed experiment plans to use an optical ring trap to hold both superfluids with the ring oriented horizontally. A circular flow around the ring will then be generated in the fermionic superfluid, for example, by using the procedure of optical stirring with a laser beam which acts as a species-selective potential for Li. A species-selective repulsive barrier seen only by the bosons can be inserted to prevent flow in the bosonic superfluid. After letting the two superfluids equilibrate, the bosonic superfluid will acquire a phase difference across the barrier due to the entrainment terms. This can subsequently be measured by observing the interference pattern after expansion.

The entrainment signal is maximized at lower magnetic fields (BEC limit) where the fermionic superfluid density increases. However, this can cause two undesirable effects: the immiscibility of the fluids and increased three-body loss. To mitigate these issues, the proposed plan is to generate the flow at B = 832 G Unitary Fermi Gas (UFG) resonance

and then slowly reducing B to maximize the signal once the flow is established.

While the proposed experimental design in [35] is primarily centered around the $^6$Li-$^{174}$Yb system, it's worth considering the potential of other dual-superfluid systems, such as a $^6$Li-$^7$Li mixture. The isotope $^7$Li is a boson that can form a Bose-Fermi superfluid mixture with $^6$Li [20], and this mixture has the potential to exhibit entrainment phenomena. The prospect of studying a $^6$Li-$^7$Li mixture is intriguing, especially given the potential for adjustable interspecies interaction, and the convenient fact that they will have similar polarizabilities in the optical dipole potential from the ring trap, resulting in a better spatial overlap than the $^6$Li-$^{174}$Yb system. However, $^6$Li-$^7$Li mixture comes with its own set of technical challenges that cannot be overlooked. The closeness of resonant transition frequencies of the two isotopes, with $^7$Li transitions being 10.6GHz higher than $^6$Li [22, 37] (with the same natural linewidth $\Gamma = 2\pi\times5.8724$MHz), present difficulties in constructing a barrier potential capable of optically stirring the $^6$Li fermionic superfluid without influencing the $^7$Li bosonic superfluid, and vice versa. This obstacle could potentially be overcome by meticulously engineering a pair of laser beams that, while separated by several GHz in frequency, are fully spatially combined.

As per Equation (19) in [31], for alkali atoms, when a linearly polarized laser's detuning from atomic transition resonance is similar to the fine-structure splitting but significantly larger than the hyperfine splitting, the dipole potential and scattering rate from the D2 line is twice that of the D1 line. In our discussion here, all laser detunings to relevant transition resonances greatly exceed any hyperfine splittings, including the 228MHz ground state splitting, but are on the order of GHz, allowing the Rotating Wave Approximation to apply. We denote the laser beam frequency as its detuning from the $^6$Li D2 line, $\Delta = \omega_{\text{Laser}} - \omega_{D2,^6\text{Li}}$. Consequently, its detuning from the $^6$Li D1 line is $\Delta + 2\pi\times10.0$GHz, from the $^7$Li D2 line is $\Delta - 2\pi\times10.6$GHz, and from the $^7$Li D1 line is $\Delta - 2\pi\times0.6$GHz. We adopt the notion $I_{sat}$ =2.54mW/cm$^2$, and the notion $\Delta_0 = 2\pi\times10$GHz. The dipole potential and the scattering rate of this laser beam on $^6$Li are therefore $U_{^6\text{Li}}(\mathbf{r}) = \frac{\hbar\Gamma^2}{24}[I(\mathbf{r})/I_{sat}][\frac{2}{\Delta} + \frac{1}{\Delta+\Delta_0}]$ and $R_{sc,^6\text{Li}}(\mathbf{r}) = \frac{\Gamma^3}{24}[I(\mathbf{r})/I_{sat}][\frac{2}{\Delta^2} + \frac{1}{(\Delta+\Delta_0)^2}]$, and its dipole potential and scattering rate on $^7$Li are therefore $U_{^7\text{Li}}(\mathbf{r}) = \frac{\hbar\Gamma^2}{24}[I(\mathbf{r})/I_{sat}][\frac{2}{\Delta-1.06\Delta_0} + \frac{1}{\Delta-0.06\Delta_0}]$ and $R_{sc,^7\text{Li}}(\mathbf{r}) =$

$\frac{\Gamma^3}{24}[I(\mathbf{r})/I_{sat}][\frac{2}{(\Delta-1.06\Delta_0)^2}+\frac{1}{(\Delta-0.06\Delta_0)^2}]$. To avoid excessive scattering and heating, $\Delta$ should be sufficiently away from the following values: $-\Delta_0$, 0, $0.06\Delta_0$, $1.06\Delta_0$.

The net potential on $^6$Li and $^7$Li, produced by the combination of two laser beams with detunings $\Delta_x = x\Delta_0$, $\Delta_y = y\Delta_0$ and intensities $I_x$, $I_y = zI_x$, is given by:

$$U_{^6\mathrm{Li}} = \frac{\hbar\Gamma^2}{24\Delta_0}[I_x/I_{sat}][\frac{2}{x}+\frac{1}{x+1}+z(\frac{2}{y}+\frac{1}{y+1})] \tag{5.1}$$

$$U_{^7\mathrm{Li}} = \frac{\hbar\Gamma^2}{24\Delta_0}[I_x/I_{sat}][\frac{2}{x-1.06}+\frac{1}{x-0.06}+z(\frac{2}{y-1.06}+\frac{1}{y-0.06})] \tag{5.2}$$

and the total scattering rate on $^6$Li and $^7$Li is given by:

$$R_{sc,^6\mathrm{Li}} = \frac{\Gamma^3}{24\Delta_0^2}[I_x/I_{sat}][\frac{2}{x^2}+\frac{1}{(x+1)^2}+z(\frac{2}{y^2}+\frac{1}{(y+1)^2})] \tag{5.3}$$

$$R_{sc,^7\mathrm{Li}} = \frac{\Gamma^3}{24\Delta_0^2}[I_x/I_{sat}][\frac{2}{(x-1.06)^2}+\frac{1}{(x-0.06)^2}+z(\frac{2}{(y-1.06)^2}+\frac{1}{(y-0.06)^2})] \tag{5.4}$$

To minimize scattering, x and y should be sufficiently distant from -1, 0, 0.06, and 1.06.

To create a repulsive potential that exclusively addresses $^6$Li (e.g., for stirring the fermionic superfluid), the following conditions must be met:

$$\begin{aligned} \frac{2}{x}+\frac{1}{x+1}+z(\frac{2}{y}+\frac{1}{y+1}) &> 0 \\ \frac{2}{x-1.06}+\frac{1}{x-0.06}+z(\frac{2}{y-1.06}+\frac{1}{y-0.06}) &= 0 \end{aligned} \tag{5.5}$$

Setting y=0.5 to minimize scattering and z=1 for balanced laser power, we obtain x=0.311 or x=3.12. Choosing x=3.12 provides a larger distance from resonance frequencies to have less scattering. Thus, a laser beam (x=3.12) 20.6GHz blue-detuned from the $^7$Li D2 line and another (y=0.5) 5GHz blue-detuned from the $^6$Li D2 line, both with equal intensity (z=1), can stir the fermionic superfluid without affecting the bosonic superfluid. In this

specific configuration, the net potential for $^6$Li is $U_{^6\mathrm{Li}}(\mathbf{r}) = 5.55 \times \frac{\hbar\Gamma^2}{24\Delta_0}\left[\frac{I_x(\mathbf{r})}{I_{sat}}\right]$, and the total scattering rates for $^6$Li and $^7$Li are given by $R_{sc,^6\mathrm{Li}}(\mathbf{r}) = 8.71 \times \frac{\Gamma^3}{24\Delta_0^2}\left[\frac{I_x(\mathbf{r})}{I_{sat}}\right] = 1.57 \times \frac{U_{^6\mathrm{Li}}(\mathbf{r})}{\hbar\Delta_0/\Gamma}$ and $R_{sc,^7\mathrm{Li}}(\mathbf{r}) = 12.1 \times \frac{\Gamma^3}{24\Delta_0^2}\left[\frac{I_x(\mathbf{r})}{I_{sat}}\right] = 2.18 \times \frac{U_{^6\mathrm{Li}}(\mathbf{r})}{\hbar\Delta_0/\Gamma}$, respectively. By considering the inverse of the higher total scattering rate on $^7$Li, we can derive a timescale that represents the duration for which the stirring session can be maintained. This timescale is crucial, as it defines the period before significant scattering begins to heat the bosonic superfluid of $^7$Li, potentially affecting the desired experimental conditions. For example, if we want a stirrer potential height of $U_{^6\mathrm{Li}} = k_B \times 50\mathrm{nK}$, then the total scattering rates are $R_{sc,^6\mathrm{Li}}$ =6.04s$^{-1}$ and $R_{sc,^7\mathrm{Li}}$ =8.38s$^{-1}$; therefore, the duration for which the stirring session can be maintained should be much less than 119ms, which is easy to satisfy for the proposed entrainment experimental protocol.

Similarly, to create a repulsive potential that exclusively addresses $^7$Li (e.g., for inhibiting flow in the bosonic superfluid), the following conditions must be met:

$$\begin{aligned} \frac{2}{x} + \frac{1}{x+1} + z\left(\frac{2}{y} + \frac{1}{y+1}\right) &= 0 \\ \frac{2}{x-1.06} + \frac{1}{x-0.06} + z\left(\frac{2}{y-1.06} + \frac{1}{y-0.06}\right) &> 0 \end{aligned} \tag{5.6}$$

Setting y=1.5 to provide a strong repulsive potential for $^7$Li while avoiding strong scattering, and z=1 for balanced laser power, we obtain x=-0.522 or x=-2.21. Choosing x=-2.21, which is further from resonances and provides a stronger repulsive potential for $^7$Li, we can use a laser beam (x=-2.21) 12.1GHz red-detuned from the $^6$Li D1 line and another (y=1.5) 4.4GHz blue-detuned from the $^7$Li D2 line, both with equal intensity (z=1), to inhibit the flow in the bosonic superfluid without affecting the fermionic superfluid. In this specific configuration, the net potential for $^7$Li is $U_{^7\mathrm{Li}}(\mathbf{r}) = 4.19 \times \frac{\hbar\Gamma^2}{24\Delta_0}\left[\frac{I_x(\mathbf{r})}{I_{sat}}\right]$, and the total scattering rates for $^6$Li and $^7$Li are given by $R_{sc,^6\mathrm{Li}}(\mathbf{r}) = 2.14 \times \frac{\Gamma^3}{24\Delta_0^2}\left[\frac{I_x(\mathbf{r})}{I_{sat}}\right] = 0.511 \times \frac{U_{^7\mathrm{Li}}(\mathbf{r})}{\hbar\Delta_0/\Gamma}$ and $R_{sc,^7\mathrm{Li}}(\mathbf{r}) = 11.2 \times \frac{\Gamma^3}{24\Delta_0^2}\left[\frac{I_x(\mathbf{r})}{I_{sat}}\right] = 2.67 \times \frac{U_{^7\mathrm{Li}}(\mathbf{r})}{\hbar\Delta_0/\Gamma}$, respectively. By considering the inverse of the higher total scattering rate on $^7$Li, we can derive a timescale that represents the duration for which the barrier session can be maintained to inhibit the flow in the bosonic $^7$Li superfluid. This timescale is crucial, as it defines the period before significant scattering begins to heat the bosonic superfluid of $^7$Li, potentially affecting the desired experimental

conditions. For example, if we want a barrier potential height of $U_{^7\mathrm{Li}} = k_B \times 50\mathrm{nK}$, then the total scattering rates are $R_{sc,^6\mathrm{Li}}$ =1.96s$^{-1}$ and $R_{sc,^7\mathrm{Li}}$ =10.26s$^{-1}$; therefore, the duration for which the barrier session can be maintained should be much less than 97.46ms, which is easy to satisfy for the proposed entrainment experimental protocol.

This proposed exploration of entrainment in dual-superfluid systems is a humble yet meaningful stride in the broader journey of understanding superfluid dynamics. The knowledge we acquire from this research may potentially contribute to the field of ultracold atoms and possibly extend to areas beyond our immediate focus. For instance, our findings could provide valuable insights into the study of celestial bodies like neutron stars and pulsars, which, due to their remote locations, present significant challenges for direct measurement and observation.

In summary, the proposed experimental protocol directly measures the bulk three-dimensional entrainment, the Andreev-Bashkin effect, in a fermionic and bosonic superfluid mixture. By using a ring geometry with a common trap for both species, the simulation for this proposed experiment demonstrated that atom interferometry techniques can produce measurable phase shifts with reasonable experimental parameters, and their dependence is characterized. With current technologies and assuming mean-field values for the dimer-boson scattering length $a_{Db}$ in $^6$Li-$^{174}$Yb mixture, a 6% phase shift should be reliable. With reasonable improvements in experimental techniques, this may be as large as 67%. The potential to extend this research to other dual-superfluid systems, such as a $^6$Li-$^7$Li mixture, opens up exciting avenues for future exploration and discovery.

### *5.3 DMD and Ring Beam Configuration*

The advent of full-complex spatial light modulation, first developed in the 1960s during the progression of computer-generated holography [67, 54, 68], has led to significant advancements in both its technology and applications. Within the realm of ultracold atoms experiments, Spatial Light Modulators (SLMs) provide the ability to generate complex light patterns, thereby facilitating the creation of nearly arbitrary spatial profiles of potentials for cold atoms [16]. They have been applied for atom-by-atom assembly of defect-free 2D atomic arrays [9].

In 1983, Larry J. Hornbeck, at Texas Instruments Inc., invented the world's first deformable mirror device, a 2D array of deformable mirror elements constructed from a single piece of reflective metalized polymer membrane addressed by an underlying MOS transistor matrix. This innovation marked the beginning of a new era of precise and rapid spatial light modulations [34, 61]. In 1994, Jeffrey B Sampsell, also at Texas Instruments Inc., further refined the technology to Digital Micromirror Devices (DMDs)[73], featuring individual two-state aluminum-sputter-on-wafer mirrors for each pixel, with the primary application being projection displays. In recent years, while the DMD product line at Texas Instruments continues to be heavily geared towards projector applications with internal LED light sources, there has been a growing application base for its use as an ultrahigh-speed spatial light modulator. This includes use in Multi-Object Spectrometers (MOS) on space missions [81], real-time biomedical image sensing [88], and various applications in AMO experiments, such as addressing multiple individual spins in an optical lattice using the same laser beam [23], producing arbitrarily patterned Bose-Einstein Condensates (BECs) through direct imaging of the DMD [25], and providing stable confinement potentials like ring traps [85] and box traps (homogeneous optical boxes) [59].

### *5.3.1 Operating principle of a DMD pixel*

A Digital Micromirror Device (DMD) pixel [52] operates using a bi-stable mechanism, with two fixed states (+12° and -12° for most contemporary DMDs) that are determined by the pixel's structural design and electrostatics during operation. These positions control the direction in which light is deflected, making the DMD a spatial light modulator. The positive (+) state, which is tilted towards the light source, is known as the "on" state, while the negative (-) state, tilted away from the light source, is the "off" state. The axis of tilt is along the diagonal of the pixel square.

From a mechanical perspective, a DMD pixel is composed of a micromirror connected to a concealed torsional hinge. The bottom side of the micromirrors comes into contact with spring tips. There are two electrodes at two corners of the pixel square that are used to maintain the micromirror in the two operational positions (commonly +12° and -12°).

Each micromirror in a Digital Micromirror Device (DMD) is electrically supported by a dual-element Complementary Metal-Oxide-Semiconductor (CMOS) memory cell, where the two elements consistently maintain opposite states. The role of the CMOS memory cell is to store the forthcoming adjustment in the micromirror's mechanical position. However, any modification to the micromirror's position will not transpire until a "mirror clocking pulse" is received.

To put it simply, once the micromirror is secured in its position, any alterations made to the state of the memory cells will not instigate the micromirror to flip. The "mirror clocking pulse" briefly disengages the mechanical lock of the micromirror, thereby allowing it to reposition according to the state of the underlying CMOS memory.

The memory of pixel groups can be preloaded, and their mechanical positions can be altered simultaneously with a single mirror clocking pulse. Each DMD model possesses unique operating modes for loading CMOS memory into the 2D pixel array and for the frequency of the mirror clocking pulse. These factors should be taken into account during the design and application stages.

When powering up and down a DMD, certain operations are necessary to ensure the proper functioning of the micromirrors. These operations position the micromirrors during power up and release them during power down. Specific details are outlined in the various DLP controller and DMD data sheets.

### *5.3.2 Pilot Development of Ring Beam with DLP2000*

In 2020, our research team launched a project to develop a ring-shaped laser beam for the purpose of trapping ultracold atoms. This initiative was undertaken during the height of the COVID-19 pandemic, a period characterized by stringent lockdown measures and limited access to resources. To navigate these challenges, we initiated a pilot study using a cost-effective approach for prototyping. We utilized the DLP LightCrafter Display 2000 Evaluation Module (DLPM2000EVM) from Texas Instruments for this purpose. This device, equipped with a .2nHD (0.2" diagonal, 640 $\times$ 360 resolution) Digital Micromirror Device (DMD), is primarily designed to function as a projector, which can be interfaced with

a BeagleBone Black (BBB) as a daughter board for external display, making it a versatile tool for our project.

The EVM is energized through an onboard DC power jack. To adapt it for our Spatial Light Modulator (SLM) needs, we executed the "export DISPLAY=:0" command on the BBB, designating the daughter board as the default display. Subsequently, we employed the "feh –F –Y" command, followed by the file name, to display the image in fullscreen (-F) on the daughterboard, while suppressing the mouse cursor (-Y).

To convert the EVM from a projector to a Spatial Light Modulator (SLM), we replaced the internal light source with a laser beam. This required substantial modifications to the EVM's Optical Engine, developed and manufactured by Young Optics Incorporated [39]. We began by carefully disassembling the black plastic enclosure with cutters, ensuring no damage was inflicted on the optical components. We then disconnected the LEDs from the internal heat sink and removed them to prevent light pollution and potential overheating.

The optical configuration for this pilot study is illustrated in Figure 5.1. A beam from a laser pointer is expanded using a 50mm to 75mm telescope, then adjusted for incident angle with two mirrors before illuminating the DMD. The DLP2000 data sheet specifies that the tilt axis (for the $\pm 12^{\circ}$ on/off flipping) runs along the diagonal of each square pixel, and it also indicates a preferred direction of illumination from the pixel at coordinates (0,0) to the pixel at coordinates (639, 359) at the opposite corner. Our pilot study confirmed that if the illumination laser enters from the pixel at coordinates (639, 359) towards the pixel at coordinates (0,0), the resulting display will be a negative image.

When the DMD is illuminated with a coherent light source, optical diffraction will occur, as the 2D array of tilted micromirrors forms a blazed grating. The output after the DMD in Figure 5.1 is a 2D matrix of diffraction orders, with the first order being our target. To achieve the blazing condition and optimize the fraction of laser power in the first order, we performed an optimization of the incident angle of the input beam using the two steering mirrors before the DMD. We also carefully aligned the DMD plane to ensure that the outgoing first order beam is in the horizontal plane for downstream optics.

The DLP LightCrafter Display 2000 Evaluation Module is designed to project an 8-bit color image by combining the capabilities of Field Sequential Color (FSC) and Pulse Width

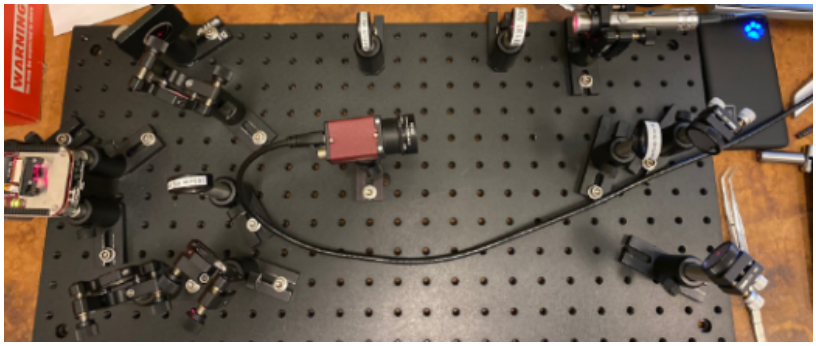

Figure 5.1: Optical setup for the DMD pilot study. The coherent light from the laser pointer on the top right passes through an expanding telescope of lenses, reflects off a pair of steering mirrors, and then illuminates the DMD (middle left) from the bottom left corner of this picture. The outcoming first order from the DMD's diffraction reflects off a mirror, passes through a lens plus three more mirrors, before passing through the final lens and onto the Mako camera in the center of this picture.

Modulation (PWM) technologies.

Field Sequential Color (FSC) operates by rapidly flashing the internal red, green, and blue LEDs in sync with the image being displayed. This rapid sequence of flashes is integrated into a single color image by the human eye due to the phenomenon known as persistence of vision. This implies that the RGB subpixels are realized in the time domain, as opposed to the spatial domain, which is the method typically employed by other technologies like LCD and OLED. While FSC is not relevant to our application with our own coherent laser source, the default synchronization between the RGB LEDs and the DMD had to be disabled via software, even after the LEDs were physically removed. We then utilized the "i2cset" command from the i2c-tools on the BBB to disable the RGB LEDs. This allowed us to modify the LED register on the DLPC2607, the digital display controller chip for both the DMD and RGB LEDs (through DLPA1000 for power management and LED driver).

Pulse-Width Modulation (PWM) is a technique employed to regulate the brightness of each subpixel by modulating the duty cycle of the pulse wave. In the context of the DLP

LightCrafter Display 2000 Evaluation Module, PWM is used to achieve an 8-bit (0 to 255) brightness level by varying the duration each subpixel remains in the "on" state during each frame. The DLPC2607 display controller on the DLP LightCrafter Display 2000 Evaluation Module supports a Pixel Clock of up to 33.5MHz, equating to a minimum pulse duration of 29.8ns, which may be sufficiently short compared to the relevant timescales of the atoms' motion (determined by the trap frequencies at large detunings), such that the atoms have sufficient time to integrate over multiple optical pulses to "perceive" a smooth potential through time-averaging.

An alternative approach for achieving different brightness level is the method of spatial error diffusion [55]. In our pilot study, we developed a python script to generate an 8-bit grayscale ring image (Figure 5.2a) with the desired parameters (e.g., outer/inner diameters, spatial intensity distribution), and then dithered this image to a 1-bit black-and-white halftone using the Floyd-Steinberg algorithm (Figure 5.2b). This 1-bit halftone image was then displayed on the DMD without the need for PWM in the display.

In the optical setup of our pilot study, the first order light output (part of the 2D diffraction pattern) from the DMD passes through an optical imaging system of lenses and subsequently imaged onto a Mako GigE camera for evaluation. It's important to note that the imaging system is subject to its optical resolution limit, meaning any details smaller than this limit will be spatially averaged. Essentially, a resolution-limited imaging system acts as an optical low-pass filter in the spatial domain. When the resolution limit of the imaging system encompasses multiple pixels of the digital image displayed the DMD, the spatially dithered black-and-white halftone digital image effectively reproduces the original grayscale display at the imaging plane on the camera's optical sensor, which is the underlying principle of our design's success.

Our pilot study successfully produced a ring-shaped beam (Figure 5.3), and we characterized its optical properties through direct imaging of the laser beams. Note that the tilt of the image captured on Mako camera is due to the tilt of the DMD to level the first order beam, as well as the tilt of various steering mirrors after the DMD in our optical setup. The comprehensive analysis of these properties is discussed in the subsequent sections. We also observed that with a well-collimated input Gaussian beam on the DMD, the resulting

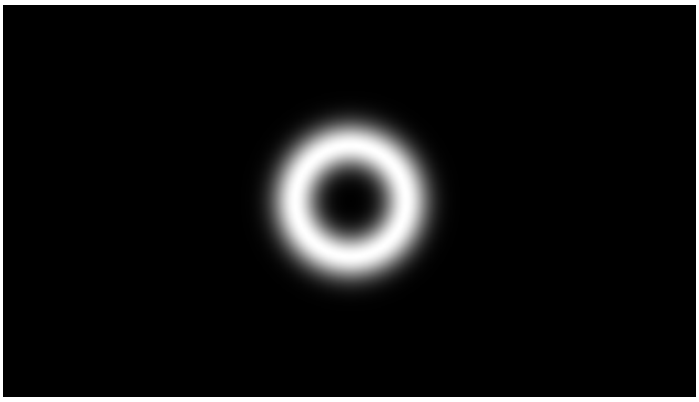

(a) 8-bit Grayscale ring image generated by python

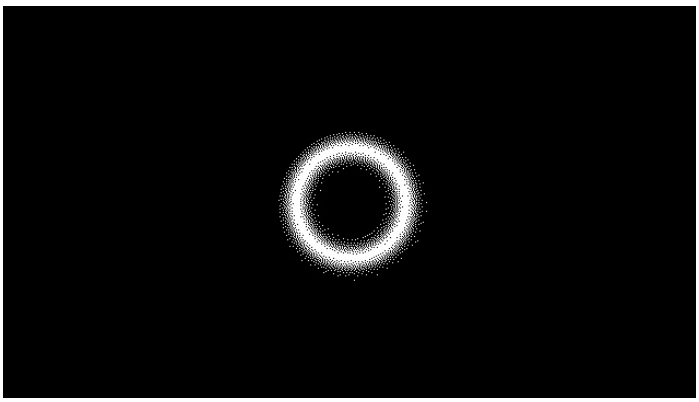

(b) 1-bit Black and White halftone image

Figure 5.2: 8-bit Grayscale ring image and its 1-bit Black and White halftone, dithered with Floyd-Steinberg algorithm. Both images are generated with a python script we developed.

ring beam maintained its collimation and ring shape over a distance of approximately 2 meters. Beyond this longitudinal distance, physical diffraction effects, attributable to the DMD-modified spatial mode of the ring beam and the Rayleigh length of the input Gaussian beam onto the DMD, began to emerge, leading to undesirable complex patterns.

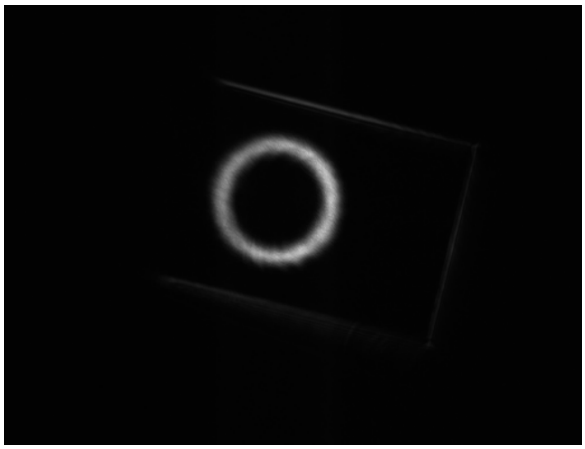

Figure 5.3: Ring beam produced (August 16, 2020) in our pilot study at the image plane when the DMD is illuminated with a laser pointer's light. The imaging system consists of a singlet lens and a Mako GigE camera. Edges of the DMD rectangular chip are visible in the shot.

### *5.4 Assessment of Ring Beam Characteristics*

In the framework of our proposed entrainment experiment with $^{174}$Yb and $^{6}$Li [35], we expect the radius of the ring trap to be between 30 to 200 $\mu$m. Although a larger radius could potentially amplify the detectable entrainment signal, it also presents challenges in maintaining the uniformity of the trap. This uniformity (or smoothness) pertains to the consistency of the ring trap potential depth as it varies along the azimuthal axis. For instance, even slight variations in the trapping potential along the torus could lead to an exponential localization of the density distribution of a Bose-Einstein Condensate (BEC) in a toroidal trap [41]. This could result in the formation of a "puddle" in the ring trap, which in turn could generate a higher level of mean-field density fluctuation that the ring geometry

is set up to mitigate [35]. This fluctuation may not fully die out within the lifespan of the metastable superfluid state. In 2013, Wright et al. [85] conducted a study on phase slips phenomena using a rotating weak link in a toroidal BEC of $^{23}$Na. In their experiment, the radius of the toroidal BEC was measured by absorption imaging to be 19.2(3)$\mu$m, and the variation in the depth of the trap along the azimuthal axis was less than 5% of the chemical potential, which provides a reference point for these technical requirements of a ring trap for toroidal BEC.

The evaluation of the ring beam generated in our pilot study was primarily conducted in the summer of 2020, during the Research Experiences for Undergraduates (REU) program. This work was carried out by our visiting undergraduate researcher, April Reisenfeld from Carleton College. Under the guidance of our postdoctoral researcher, Katie McCormick, and utilizing data from my experimental measurements, April developed a software tool using Mathematica. This tool was designed to analyze and optimize the characteristics of the trap to facilitate effective entrainment detection. The software primarily focuses on analyzing the optical dipole trapping potential derived from the ring beam, based on the AC Stark shift. It evaluates the shape of the trap in terms of the width and radius of the toroidal trap, the radial harmonic oscillator frequency of the trap, and the smoothness of the trap along the azimuthal axis.

The software accomplishes this by identifying the brightest point of the ring beam's radial cross-section at every azimuthal angle, and then assessing the optical intensity of the ring beam at that pixel. Subsequently, a Gaussian fit is generated along the radial cross-section around each of these points, which results in the determination of the width of the ring trap at every azimuthal angle. The overall beam intensity is characterized by the following equation:

$$I(r,\theta) = \frac{2P}{\pi w_0(\theta)^2}\mathrm{Exp}\left(\frac{-2(r-r_0(\theta))^2}{w_0(\theta)^2}\right) \tag{5.7}$$

In this equation, P represents the optical power of the laser, $w_0(\theta)$ is the beam waist (or ring width), and $r_0(\theta)$ is the ring radius for each azimuthal angle $\theta$. At each azimuthal angle, the Gaussian profile of the intensity distribution near the peak intensity point can

be expanded to the second order in radial distance. This provides the harmonic oscillator frequency in the radial trap, which is particularly relevant for BECs as they predominantly occupy the lowest energy levels in such potential wells, where a harmonic oscillator approximation applies.

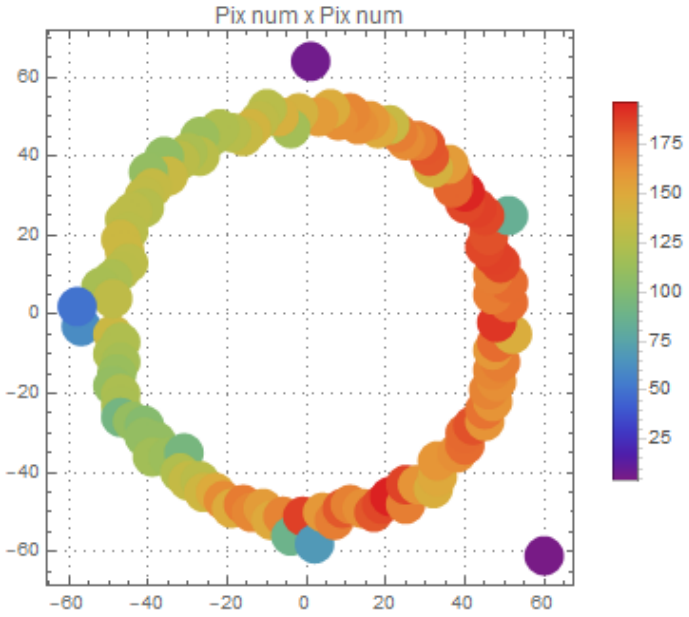


Figure 5.4: This diagram shows the peak intensity pixels within the radial slices at every azimuthal angle of the ring image, which corresponds to the trap potential's lowest point (for red-detuned laser light). The axes are denoted by pixel counts (1 pixel=3.75$\mu$m for Mako GigE camera), with the origin point (0,0) indicating the center of the ring. The legend on the right side interprets the pixel intensity values, which are depicted through the use of false color variations. The changes in intensity at the base of the trap potential along the azimuthal direction are visually represented in this plot.

April's analysis revealed that the ring in Figure 5.3 has an average radius of about 187.5 $\mu$m (see Figure 5.4), and the standard deviation in the width $w_0(\theta)$ of our ring beam calculates to be about 7.6% of the mean Figure 5.5a. April's analysis revealed that the standard deviation in peak intensity along the azimuthal axis is approximately 24.3% of the

mean (see Figure 5.5b).

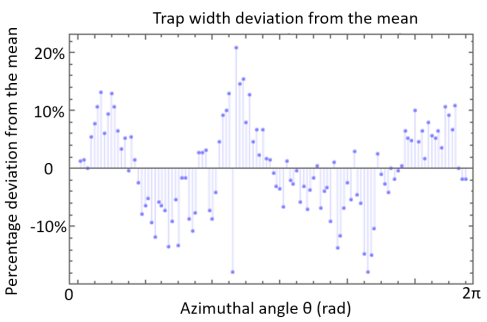


(a) Azimuthal fluctuations in ring width

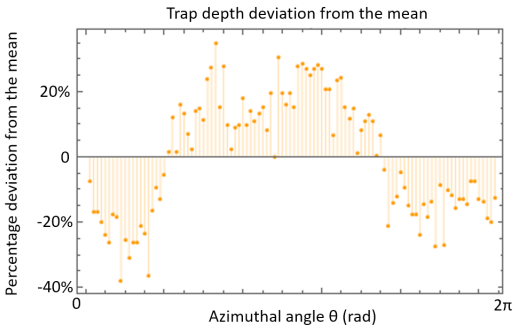


(b) Azimuthal fluctuations in peak intensity

Figure 5.5: Plots showing azimuthal fluctuations of the ring beam. The horizontal axes in both plots span the entire ring of $2\pi$ radians in azimuthal angle. Figure 5.5a shows the relative deviation of each radial slice's width from the average, which predominantly remain within 20% of the mean, with a standard deviation of approximately 7.6% of the mean. Figure 5.5b shows the relative deviation of each radial slice's peak intensity from the average peak intensity, which predominantly remain within 40% of the mean, with a standard deviation of approximately 24.3% of the mean.

The smoothness of the trap is best characterized by the variation in trap depth (at peak light intensity) along the azimuthal axis, relative to the chemical potential of the Bose-Einstein Condensate (BEC) in the ring trap. The chemical potential of a toroidal BEC is given by the following equation [66]:

$$\mu = \sqrt{\frac{Ngm\omega_r\omega_z}{2\pi^2 r_0}} \tag{5.8}$$

In this equation, $N$ represents the number of atoms in the trap, $g = 4\pi\hbar^2 a_s/m$ is the coupling constant, and $\omega_r$ and $\omega_z$ are the radial and vertical trap frequencies, respectively. The actual trap frequencies experienced by the atoms depend on many practical factors, such as laser intensity at the atoms, beam size, and shape after the optical systems. These factors are usually measured experimentally. Similarly, the number of atoms in the toroidal

superfluid is another parameter to be measured. For Li, it is possible to tune the s-wave scattering length through an external magnetic field as well. However, in an effective confinement of the superfluid (or degenerate quantum gas), the total atom number captured in the trap should result in a chemical potential that is not significantly larger than the potential depth of the ring trap.

While the current standard deviation requires further refinement to achieve a target variation of less than 5% fluctuation in trap depth relative to the toroidal superfluid's chemical potential, this pilot study has laid a solid foundation. It has provided valuable insights and data that will undoubtedly contribute to the ongoing development and exploration of toroidal superfluids.

### *5.5 Optical System Limitations and Mitigation Methods*

The creation of a well-defined ring beam at the atomic cloud's location within our vacuum chamber requires not only the formation of a high-quality ring beam, but also the management of resolution limits and aberrations in our optical system. The spherical aberrations from the 2" diameter lens and the 1.5" diameter glass viewport window are particularly significant.

In terms of resolution limits, given the typical healing length for a Bose-Einstein Condensate (BEC) is on the order of microns [24], it is desirable to design an optical system with a resolution limit close to, or better than, a few microns. This would enable a finely resolved light intensity distribution and a smooth trap potential as intended. The diffraction-limited resolution of an optical system, denoted by $R = 0.61\lambda/\mathrm{NA}$, suggests the advantage of achieving as large a Numerical Aperture (NA) as possible within the system.

However, the experimental setup presents challenges due to the substantial working distance between the glass viewport window and the atomic cloud inside the vacuum. In our setup, this vertical distance, from the center of our upper viewport window to our atomic cloud, is typically 63mm. The 1.5-inch diameter of the stainless steel tube that houses this upper viewport window imposes an upper limit of 0.3 for the NA of this optical system, a constraint dictated by the geometry.

Furthermore, as the wavelengths of our lasers are comparable to the desired resolution,

wavefront aberrations from various optical surfaces within our system become significant performance limiters as we increase the effective aperture illuminated by the enlarged laser beam. Figure 5.6 displays such a prescription of our optical system with a maximum aperture semi-diameter at the glass viewport surface (the optical stop surface). The distance between the lens and the viewport window is already optimized using the default merit function in Zemax OpticStudio to minimize the Root-Mean-Square sum of the Gaussian Quadrature of wavefront errors. The cross-section of this layout is depicted in Figure 5.7a. The Seidel diagram of this optical system, shown in Figure 5.7b, reveals a significant sum of spherical aberrations, preventing the formation of a focus at the imaging plane in Figure 5.7a. The spherical aberrations in Seidel diagrams (Figure 5.7b and Figure 5.9b) from Zemax OpticStudio are measured by the physical distance in focus points of rays passing through the outer parts of a lens and rays passing through the center of the lens, and the units are in millimeters. The effect of spherical aberration for such large apertures is much more pronounced than in most other applications where the laser beams in this optical system have a semi-diameter smaller than 10mm, and resulting from the lack of a focus, Zemax OpticStudio is unable to analyze the Point Spread Function (PSF) or Modulation Transfer Function (MTF) for such a system.

As seen in Figure 5.7b, the singlet 2" spherical lens, located above the viewport window, contributes the majority of these spherical aberrations. However, it can be easily replaced as it is outside the vacuum system. Generally, larger 2" diameter lenses are more susceptible to manufacturing variations than smaller 1" diameter lenses, and even in the perfect spherical shape, the intrinsic optical aberration of the spherical surface becomes more profound as we move towards the edge of the lens and away from the optical axis (compared to the radius of curvature of the surface), as is the case for larger effective apertures from larger diameter beams.

On the other hand, the two surfaces of the viewport window (air-glass and glass-vacuum), despite being optically flat, still generate spherical aberrations that must be mitigated to successfully achieve a ring trap.

One potential method to increase the Numerical Aperture of the system is the use of in-vacuo optics [78]. This approach could reduce the working distance and bypass the geometric

Lens Data

Update: All Windows

Surface 5 Properties | Configuration 1/1

| | Surface Type | | Comment | Radius | Thickness | Material | Coating | Clear Semi-Dia | Chip Zone | Mech Semi-Dia | Conic | TCE x 1E-6 |
|---|---|---|---|---|---|---|---|---|---|---|---|---|
| 0 | OBJECT | Standard | | Infinity | Infinity | | | 0.000 | 0.000 | 0.000 | 0.0... | 0.000 |
| 1 | (aper) | Standard | LA1050-A | 51.500 | 9.690 | N-BK7 | THORA | 25.400 U | 0.000 | 25.400 | 0.0... | - |
| 2 | (aper) | Standard | | Infinity | 23.103 V | | THORA | 25.400 U | 0.000 | 25.400 | 0.0... | 0.000 |
| 3 | STOP (aper) | Standard | | Infinity | 2.667 | N-BK7 | | 19.050 U | 0.000 | 19.050 | 0.0... | - |
| 4 | (aper) | Standard | | Infinity | 63.000 | VACUUM | | 19.050 U | 0.000 | 19.050 | 0.0... | - |
| 5 | IMAGE | Standard | | Infinity | - | | | 0.844 | 0.000 | 19.050 | 0.0... | 0.000 |

Figure 5.6: Prescription for a 2-inch diameter, 100mm focal length lens (Thorlabs A-coat), a 0.105-inch thick BK7 glass viewport window, and a 63mm back focal length in vacuum.

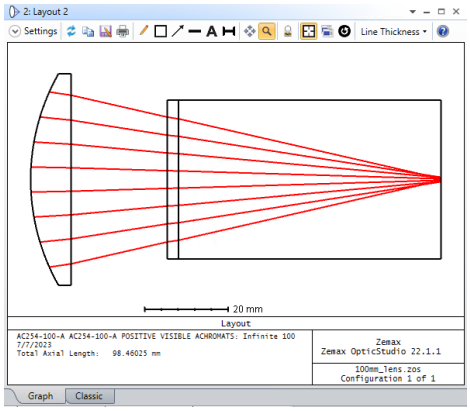


(a) Cross-section layout diagram of Figure 5.6.

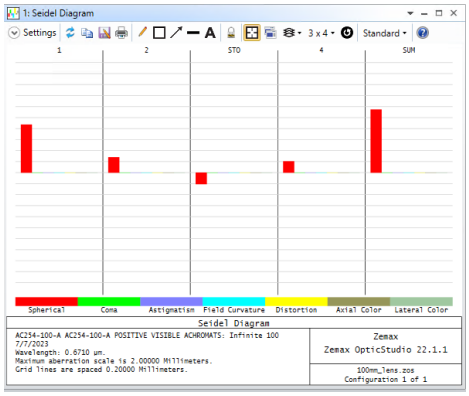


(b) Seidel diagram of the prescription in Figure 5.6

Figure 5.7: Cross-section layout and Seidel diagram of Figure 5.6. Even after optimization, no perfect focus can be formed at the imaging plane due to the large aberrations (Figure 5.7b) in the system.

limitations imposed by the viewport window diameter. However, this method necessitates the use of bakable and vacuum-compatible lenses. Furthermore, in-vacuo optics cannot be realigned once the vacuum chamber is sealed, and they may potentially limit optical access to atoms. For an established vacuum system like ours, implementing in-vacuo optics would require significant work and downtime due to the need to break and reseal the vacuum.

An alternative solution, first demonstrated by Wolfgang Alt [2], involves designing a four-lens assembly that incorporates the vacuum window as the final optical component. This design aims to minimize the total spherical aberration in the optical system, including the glass window, and achieve a high Numerical Aperture. The principle behind this method is to balance the positive spherical aberrations from convex surfaces with the negative spherical aberrations from concave surfaces. Adaptations of this design have been successfully implemented for long working distances, such as 49.2mm and 98.0mm in vacuum [65].

Building on the prescription in [65] for a 98.0mm vacuum, I adjusted the lens spacing and some lens surface curvature radii to design a lens assembly suitable for our optical system with 63.0mm in vacuum (Figure 5.8, Figure 5.9a). This prescription has an effective focal length of EFFL=81.149mm and a working f-number of WFNO=2.675 (and hence NA=0.187); an entrance pupil diameter of ENPD=29.962mm is used for design and analysis, where the optical stop surface is at the front surface of the second lens (surface 3 in Figure 5.8), and a clear semi-diameter of 22.86mm (90% of the mechanical semi-diameter 25.4mm) is assumed for this 2" lens. If a lens with a larger clear semi-diamter is used, the Numerical Aperture of this optical system will increase accordingly.

The performance of this design is evaluated in the Seidel Diagram Figure 5.9b, Point Spread Function (PSF) Figure 5.10a, and Modulation Transfer Function (MTF) Figure 5.10b. The results indicate performance very close to the diffraction limit, and effectively alleviates the aberrations while maintaining a reasonable NA=0.187.

Lastly, while the operational design of the Digital Micromirror Device (DMD) assumes each pixel merely geometrically reflects a portion of the illumination light towards one direction in each of the on/off states, in practice, the non-paraxial diffraction from each pixel can introduce its own aberration in the final ring beam. This is particularly true for coherent light sources like narrow-linewidth laser beams [19, 87].

Lens Data

Update: All Windows

Surface 11 Properties | Configuration 1/1

| | Surface Type | | Comment | Radius | | Thickness | | Material | Coating | Clear Semi-Dia | | Chip Zone | Mech Semi-Dia | | Conic | TCE x 1E-6 |
|---|---|---|---|---|---|---|---|---|---|---|---|---|---|---|---|---|
| 0 | OBJECT | Standard | | Infinity | | Infinity | | | | 0.000 | | 0.000 | 0.000 | | 0.0... | 0.000 |
| 1 | (aper) | Standard | Custom | Infinity | | 2.500 | | BK7 | | 22.860 | U | 0.000 | 25.400 | U | 0.0... | - |
| 2 | (aper) | Standard | | 64.308 | V | 65.813 | | | | 22.860 | U | 0.000 | 25.400 | | 0.0... | 0.000 |
| 3 | STOP (aper) | Standard | LB1199-A | 204.980 | | 6.160 | | N-BK7 | THORA | 22.860 | U | 0.000 | 25.400 | U | 0.0... | - |
| 4 | (aper) | Standard | | -204.980 | | 30.000 | | | THORA | 22.860 | U | 0.000 | 25.400 | | 0.0... | 0.000 |
| 5 | (aper) | Standard | Custom | 102.422 | V | 5.100 | | N-BK7 | THORA | 22.860 | U | 0.000 | 25.400 | U | 0.0... | - |
| 6 | (aper) | Standard | | Infinity | | 11.563 | V | | THORA | 22.860 | U | 0.000 | 25.400 | | 0.0... | 0.000 |
| 7 | (aper) | Standard | LE1985-A | 100.080 | | 5.100 | | N-BK7 | THORA | 22.860 | U | 0.000 | 25.400 | U | 0.0... | - |
| 8 | (aper) | Standard | | 279.120 | | 48.000 | | | THORA | 22.860 | U | 0.000 | 25.400 | | 0.0... | 0.000 |
| 9 | (aper) | Standard | | Infinity | | 2.667 | | N-BK7 | | 19.050 | U | 0.000 | 19.050 | | 0.0... | - |
| 10 | (aper) | Standard | | Infinity | | 63.000 | | VACUU... | | 19.050 | U | 0.000 | 19.050 | | 0.0... | - |
| 11 | IMAGE | Standard | | Infinity | | - | | | | 6.347E-03 | | 0.000 | 19.050 | | 0.0... | 0.000 |

Figure 5.8: Prescription for 4-lens assembly with a custom lens, Thorlabs LB1199-A, another custom lens and Thorlabs LE1985-A, which minimizes the spherical aberration from our glass viewport window.

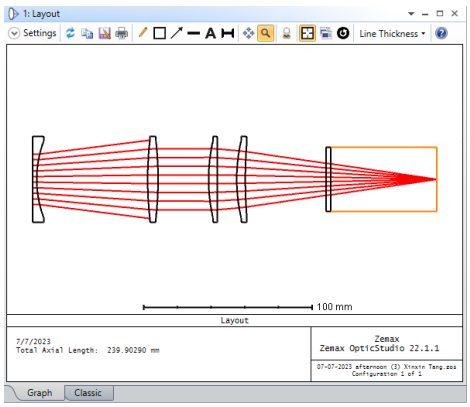


(a) Layout of my design

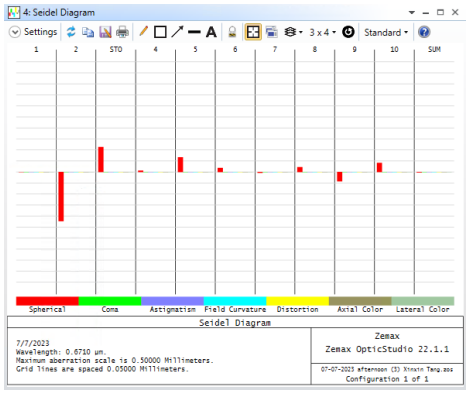


(b) Seidel diagram of my design

Figure 5.9: Cross-section layout and Seidel diagram of my 4-lens design for our optical system to mitigate the aberrations.

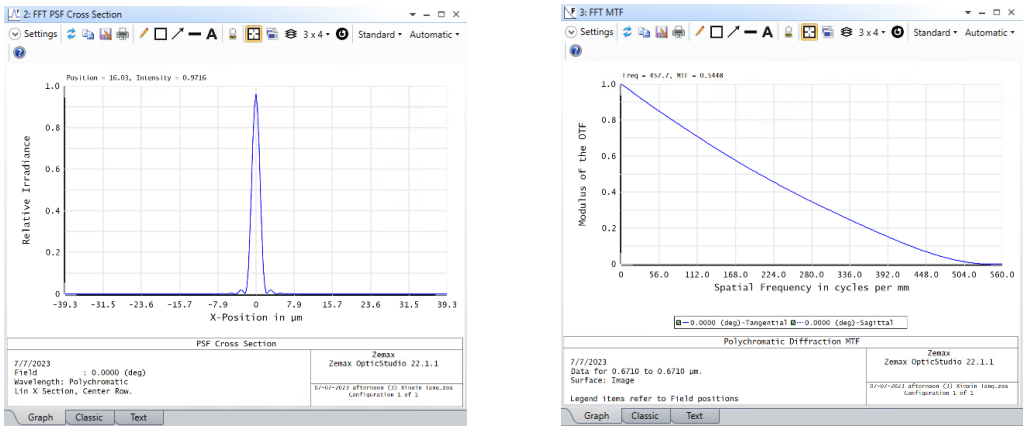


(a) PSF of my design

(b) MTF of my design

Figure 5.10: PSF and MTF of my 4-lens design for our optical system, showing performance close to the diffraction limit.

In the field of Computational Adaptive Optics, Deep Learning techniques have been employed for wavefront sensing and aberration correction. These techniques have been applied in various domains such as atmospheric science [83] and biomedical imaging [36, 77]. Pertaining to our ring beam application, this Computational Adaptive Optics approach holds the potential to rectify all aberrations present throughout the entire system, including those in the DMD itself, the lens systems, and the vacuum glass window. A well-trained model could be utilized to engineer the image displayed on the DMD.

The exploration of this method would require extensive data derived from experimental operations of the actual apparatus in our lab. Despite this, it holds the promise of delivering highly effective ring trap results.

## *5.6 Summary and Future Directions*

In this chapter, we have discussed the motivation for creating complex patterned traps, such as ring traps, for ultracold atoms experiments and the myriad opportunities they present, which include the study of entrainment (or the Andreev-Bashkin effect) in Dual-Superfluid systems. We reviewed the advent of Spatial Light Modulation and the development of

Digital Micromirror Devices (DMDs), as well as their originally intended applications in projection display. We detailed the operating principles of DMDs and our pilot study of generating a ring beam using the cost-effective evaluation module DLPM2000EVM.

The assessment of the ring beam generated in our pilot study revealed that we achieved a ring of radius 1.3mm with less than 4% variation in its shape (width and radius) and less than 15% variation in its trap depth. We analyzed the limitations of our optical system, including the geometrical limit of Numerical Aperture and the effect of aberrations on the system's performance. We then presented a viable solution of a 4-lens assembly design to effectively alleviate the wavefront aberrations while maintaining a reasonable NA=0.187.

Looking ahead, our team is building on the solid progress and valuable insights gained from the pilot study to pursue a ring beam with a smaller radius (around 100$\mu$m or smaller) and smaller variations, using a DLi6500 .65" 1080p Type-A Development Kit recently procured from Digital Light Innovations. We are also exploring the application of blue detuned laser light to achieve a more homogeneous ring potential, where a trench of zero potential ring in between the repulsive potentials by the blue detuned laser could provide a ring trap with less variations in its depth.

The generation of the vertical confinement for the ring trap could be achieved by using a telescoping pair of cylindrical lenses to expand the aspect ratio of a Gaussian beam, red-detuned from the atomic transition addressed. Alternatively, it can be achieved by the use of a blue-detuned laser beam in its $TEM_{01}$ spatial mode, which can be created using a DMD with a well-engineered image.

Once the ring beam and the vertical confinement are both in good order, the time will come for integrating them with the actual BEC atoms in our apparatus to form a toroidal BEC and characterize its properties for validation.

A toroidal BEC within a ring trap provides a rich platform for scientific exploration due to its inherent topological properties. The central hole in the annulus serves as a nucleus for the formation of topological defects, such as vortices resulting from dynamical excitation (like optical stirring [85]), or fluxons induced by external magnetic fields [40]. The capability to execute precise and coherent quantum control on ultracold atoms in a toroidal BEC could illuminate our understanding of various properties in superfluids and superconductors. The

foundational work we have discussed in this chapter paves the way for this line of research in our laboratory for years to come.

# Chapter 6

# CONCLUSION AND FUTURE WORK

## *6.1 Summary*

This thesis has presented our comprehensive exploration into the laser cooling and trapping of $^6$Li, a fermionic atom, with the objective of creating experimental tools for the investigation of many-body fermionic dynamics in quantum degeneracy, specifically with Quantum Kicked Rotor method and within ring traps for superfluids. We have provided an extensive overview of the properties of $^6$Li, the theoretical foundations of many-body fermionic dynamics in cold atom traps, and the principles of AC Stark shift in far-off-resonance light fields.

Our experimental apparatus, capable of trapping Yb and Li, has been detailed, along with our completed experiments on YbLi MFR and Yb bosonic dynamics. We have discussed the technical adaptations for laser cooling and trapping of $^6$Li towards a single-species Fermi condensate with tunable many-body interactions, including our sub-Doppler cooling system and magnetic field stabilization method. Our progress towards quantum degeneracy and the development of a method of optical pulses to induce dynamics in the paired Fermi condensate have been presented.

Furthermore, we have elaborated on our work on ring traps and entrainment, including the development of a ring beam setup using a digital micromirror device (DMD). The significance of our developments in the context of many-body fermionic dynamics in quantum degeneracy and the use of ring traps for studying dual-superfluid systems has been underscored, contributing to the broader field of ultracold atomic physics.

## *6.2 Future directions*

Looking forward, our work has laid a solid foundation for future research in the field of ultracold atomic physics. The experimental tools and methods developed in this thesis will

enable further exploration of many-body fermionic dynamics in quantum degeneracy. Our work on ring traps and entrainment opens up new avenues for studying dual-superfluid systems and the fascinating phenomena they exhibit.

In particular, our work on the stabilization of the large bias magnetic field can be extended with the aim of accessing the narrow lines in p-wave and s-wave resonances of $^6$Li ensembles. Our method of using short pulses of standing-wave potentials to induce quantum dynamics in $^6$Li will also be further refined.

Our work on ring traps and entrainment will be extended to study the entrainment effect in dual-superfluid systems in more detail. We plan to further develop our ring beam setup using a DMD, with the goal of achieving a smoother and more precise trap. This will enable us to study the behavior of dual-superfluid systems under various conditions and gain deeper insights into their dynamics.

In conclusion, the research presented in this thesis represents our earnest efforts to contribute to the field of ultracold atomic physics. We are humbled by the opportunity to add to the collective knowledge in this fascinating area of study and look forward to the potential for future discoveries.

# BIBLIOGRAPHY


[1] E. R. I. Abraham, W. I. McAlexander, J. M. Gerton, R. G. Hulet, R. Côté, and A. Dalgarno. Triplet s-wave resonance in $^6$Li collisions and scattering lengths of $^6$Li and $^7$Li. *Phys. Rev. A*, 55:R3299–R3302, May 1997.

[2] Wolfgang Alt. An objective lens for efficient fluorescence detection of single atoms. *Optik*, 113(3):142–144, 2001.

[3] A. F. Andreev and E. P. Bashkin. Three-velocity hydrodynamics of superfluid solutions. *Soviet Physics, JETP*, 42:164, 1975.

[4] M. Antonelli and P. M. Pizzochero. Pulsar rotation with superfluid entrainment. *Journal of Physics: Conference Series*, 861:012024, 2016.

[5] Jon Applequist. An atom dipole interaction model for molecular optical properties. *Accounts of Chemical Research*, 10(3):79–85, 03 1977.

[6] Peter Atkins and Ronald Friedman. *Molecular Quantum Mechanics*. Oxford University Press, 4th edition, 2005.

[7] James R. Bainter. Active filter has stable notch and response can be regulated. *Electronics*, pages 115–117, October 1975.

[8] J. Bardeen, L. N. Cooper, and J. R. Schrieffer. Theory of superconductivity. *Phys. Rev.*, 108:1175–1204, Dec 1957.

[9] Daniel Barredo, Sylvain de Léséleuc, Vincent Lienhard, Thierry Lahaye, and Antoine Browaeys. An atom-by-atom assembler of defect-free arbitrary two-dimensional atomic arrays. *Science*, 354(6315):1021–1023, 2016.

[10] M. Bartenstein, A. Altmeyer, S. Riedl, S. Jochim, C. Chin, J. Hecker Denschlag, and R. Grimm. Crossover from a molecular bose-einstein condensate to a degenerate fermi gas. *Phys. Rev. Lett.*, 92:120401, Mar 2004.

[11] Mateusz Borkowski, Lukas Reichsöllner, Premjith Thekkeppatt, Vincent Barbé, Tijs van Roon, Klaasjan van Druten, and Florian Schreck. Active stabilization of kilogauss magnetic fields to the ppm level for magnetoassociation on ultranarrow Feshbach resonances. *Review of Scientific Instruments*, 94(7):073202, 07 2023.

[12] A. Bulgac, M. M. Forbes, S. Jin, R. N. Perez, and N. Schunck. Minimal nuclear energy density functional. *Physical Review C*, 97:044313, 2018.

[13] A. Burchianti, G. Valtolina, J. A. Seman, E. Pace, M. De Pas, M. Inguscio, M. Zaccanti, and G. Roati. Efficient all-optical production of large $^6$Li quantum gases using $D_1$ gray-molasses cooling. *Phys. Rev. A*, 90:043408, Oct 2014.

[14] Alec Cao, Roshan Sajjad, Hector Mas, Ethan Q. Simmons, Jeremy L. Tanlimco, Eber Nolasco-Martinez, Toshihiko Shimasaki, H. Esat Kondakci, Victor Galitski, and David M. Weld. Interaction-driven breakdown of dynamical localization in a kicked quantum gas. *Nature Physics*, 2022.

[15] N. Chamel. Superfluidity and superconductivity in neutron stars. *Journal of Astrophysics and Astronomy*, 38:43, 2017.

[16] Florian chäfer, Takeshi Fukuhara, Seiji Sugawa, Yosuke Takasu, and Yoshiro Takahashi. Tools for quantum simulation with ultracold atoms in optical lattices. *Nature Reviews Physics*, 2:411–425, 2020.

[17] Franco Dalfovo, Stefano Giorgini, Lev P. Pitaevskii, and Sandro Stringari. Theory of bose-einstein condensation in trapped gases. *Rev. Mod. Phys.*, 71:463–512, Apr 1999.

[18] B. DeMarco and D. S. Jin. Onset of fermi degeneracy in a trapped atomic gas. *Science*, 285(5434):1703–1706, 1999.

[19] Xue Dong, Yingchao Shi, Xingchen Xiao, Qian Zhang, Fei Chen, Xu Sun, Weizheng Yuan, and Yiting Yu. Non-paraxial diffraction analysis for developing dmd-based optical systems. *Optics Letters*, 47(18):4758–4761, 2022.

[20] I. Ferrier-Barbut, M. Delehaye, S. Laurent, A. T. Grier, M. Pierce, B. S. Rem, F. Chevy, and C. Salomon. A mixture of bose and fermi superfluids. *Science*, 345(6200):1035–1038, 2014.

[21] Christopher J. Foot. *Atomic Physics*. Oxford University Press, 2005.

[22] Cora Fujiwara. Dynamics of ultracold lithium in modulated optical lattices, 2019. PhD thesis, UC Santa Barbara.

[23] Takeshi Fukuhara, Adrian Kantian, Manuel Endres, Marc Cheneau, Peter Schauß, Sebastian Hild, David Bellem, Ulrich Schollwöck, Christian Gross Thierry Giamarchi, Immanuel Bloch, and Stefan Kuhr. Quantum dynamics of a mobile spin impurity. *Nature Physics*, 9:235–241, 2013.

[24] Monica Gutierrez Galan. Bose einstein condensates for analogue cosmology experiments, 2021. PhD thesis, University of Maryland.

[25] G. Gauthier, I. Lenton, N. McKay Parry, M. Baker, M. J. Davis, H. Rubinsztein-Dunlop, and T. W. Neely. Direct imaging of a digital-micromirror device for configurable microscopic optical potentials. *Optica*, 3(10):1136–1143, 2016.

[26] Michael Gehm. Preparation of an optically-trapped degenerate fermi gas of 6li: Finding the route to degeneracy, 2003. PhD thesis, Duke University.

[27] Stefano Giorgini, Lev P. Pitaevskii, and Sandro Stringari. Theory of ultracold atomic Fermi gases. *Reviews of Modern Physics*, 80(4):1215–1274, 2008.

[28] Alaina Green. Heteronuclear feshbach resonances in ultracold mixtures of ytterbium and lithium, 2019. PhD thesis, University of Washington.

[29] Alaina Green, Hui Li, Jun Hui See Toh, Xinxin Tang, Katherine McCormick, Ming Li, Eite Tiesinga, Svetlana Kotochigova, and Subhadeep Gupta. Feshbach resonances in p-wave three-body recombination within fermi-fermi mixtures of open-shell 6li and closed-shell 173yb atoms. *Physical Review X*, 10:031037, 2020.

[30] Andrew T. Grier, Igor Ferrier-Barbut, Benno S. Rem, Marion Delehaye, Lev Khaykovich, Frédéric Chevy, and Christophe Salomon. Λ-enhanced sub-doppler cooling of lithium atoms in $D_1$ gray molasses. *Phys. Rev. A*, 87:063411, Jun 2013.

[31] Rudolf Grimm, Matthias Weidemüller, and Yurii B. Ovchinnikov. Optical dipole traps for neutral atoms. *Advances in Atomic, Molecular, and Optical Physics*, 42:95–170, 2000.

[32] Subhadeep Gupta. Experiments with degenerate bose and fermi gases, 2003. PhD thesis, MASSACHUSETTS INSTITUTE OF TECHNOLOGY.

[33] Anders H. Hansen. Interacting quantum gases of lithium and ytterbium, 2013. PhD thesis, University of Washington.

[34] LARRY J. HORNBECK. 128 x 128 deformable mirror device. *IEEE Transactions on electron devices*, ED-30(5):539–545, 1983.

[35] Khalid Hossain, Subhadeep Gupta, and Michael McNeil Forbes. Detecting entrainment in fermi-bose mixtures. *Physical Review A*, 105:063315, 2022.

[36] D. hu, R. Wang, M. Zurauskas, P. Pande, J. Bi, Q. Yuan, L. Wang, Z. Gao, and S.A. Boppart. Automated fast computational adaptive optics for optical coherence tomography based on a stochastic parallel gradient descent algorithm. *Optics Express*, 28(16):23306–23319, 2020.

[37] Randall G Hulet, Jason H V Nguyen, and Ruwan Senaratne. Methods for preparing quantum gases of lithium. *Review of Scientific Instruments*, 91(1):011101, 2020.

[38] T. W. Hänsch and A. L. Schawlow. Cooling of gases by laser radiation. *Optics Communications*, 13(1):68–69, 1975.

[39] Texas Instruments Incorporated. TI DLP Module 2000 EVM User's Guide, 2021. Texas Instruments Technical Document, DLPU089.

[40] I.V.Vernik, S.Keil, A.V.Ustinov, N.Thyssen s, T.Doderer, H.Kohlstedt, and R.P.Huebener. Trapped fluxons in annular josephson junctions in the external magnetic field. *Proceedings of the 21st International Conference on Low Temperature Physics*, August 1996.

[41] A. D. Jackson and G. M. Kavoulakis. Bose-einstein-condensed atoms in toroidal traps. *Phys. Rev. A*, 74:065601, Dec 2006.

[42] Jakub Janarek, Dominique Delande, Nicolas Cherroret, and Jakub Zakrzewski. Quantum boomerang effect for interacting particles. *Phys. Rev. A*, 102:013303, Jul 2020.

[43] Jakub Janarek, Jakub Zakrzewski, and Dominique Delande. Many-body quantum boomerang effect. *Phys. Rev. B*, 107:094204, Mar 2023.

[44] S. Jochim, M. Bartenstein, A. Altmeyer, G. Hendl, C. Chin, J. Hecker Denschlag, and R. Grimm. Pure gas of optically trapped molecules created from fermionic atoms. *Physical Review Letters*, 91(24):240402, 2003.

[45] S. Jochim, M. Bartenstein, A. Altmeyer, G. Hendl, S. Riedl, C. Chin, J. Hecker Denschlag, and R. Grimm. Bose-einstein condensation of molecules. *Science*, 302(5653):2101–2103, 2003.

[46] Wolfgang Ketterle and Martin W. Zwierlein. Making, probing and understanding ultracold fermi gases. *arXiv 0801.2500*, 2008.

[47] Alexander Khramov. Experiments in the ultracold lithium - ytterbium system, 2013. PhD thesis, University of Washington.

[48] Alexander Y. Khramov, Anders H. Hansen, Alan O. Jamison, William H. Dowd, and Subhadeep Gupta. Dynamics of feshbach molecules in an ultracold three-component mixture. *Phys. Rev. A*, 86:032705, Sep 2012.

[49] Filip Kiałka, Benjamin A. Stickler, and Klaus Hornberger. Orbital angular momentum interference of trapped matter waves. *Phys. Rev. Res.*, 2:022030, May 2020.

[50] TOSHIYA KINOSHITA, TREVOR WENGER, and DAVID S. WEISS. Observation of a one-dimensional tonks-girardeau gas. *Science*, 305:1125–1128, August 2004.

[51] Roman V. Krems, William C. Stwalley, and Bretislav Friedrich, editors. *Cold Molecules: Theory, Experiment, Applications*. CRC Press/Taylor & Francis, 2009.

[52] Benjamin Lee. Introduction to ±12 Degree Orthogonal Digital Micromirror Devices (DMDs), 2018. Texas Instruments Technical Document, DLPA008B.

[53] John Lekavich. Basics of acousto-optic devices. *Lasers & Applications*, pages 59–64, April 1986.

[54] A. W. Lohmann and D. P. Paris. Binary fraunhofer holograms, generated by computer. *APPLIED OPTICS*, 6(10):1739–1748, 1967.

[55] Ruichao Ma. Engineered potentials and dynamics of ultracold quantum gases under the microscope, 2014. PhD thesis, Harvard University.

[56] S. Sagar Maurya, J. Bharathi Kannan, Kushal Patel, Pranab Dutta, Korak Biswas, Jay Mangaonkar, M. S. Santhanam, and Umakant D. Rapol. Interplay between quantum diffusion and localization in the atom-optics kicked rotor. *Phys. Rev. E*, 106:034207, Sep 2022.

[57] B. Merkel, K. Thirumalai, J. E. Tarlton, V. M. Schäfer, C. J. Ballance, T. P. Harty, and D. M. Lucas. Magnetic field stabilization system for atomic physics experiments. *Review of Scientific Instruments*, 90(4), 04 2019. 044702.

[58] A. J. Moerdijk, B. J. Verhaar, and A. Axelsson. Resonances in ultracold collisions of $^{6}$Li, $^{7}$Li, and $^{23}$Na. *Phys. Rev. A*, 51:4852–4861, Jun 1995.

[59] Nir Navon, Robert P. Smith, and Zoran Hadzibabic. Quantum gases in optical boxes. *Nature Physics*, 17:1334–1341, 2021.

[60] J. Nespolo, G. E. Astrakharchik, and A. Recati. Andreev-bashkin effect in superfluid cold gases mixtures. *New Journal of Physics*, 19:125005, 2017.

[61] Dennis R. Pape and Larry J. Hornbeck. Characteristics of the deformable mirror device for optical information processing. *Optical Engineering*, 22(6):675–681, 1983.

[62] L. Parisi, G. E. Astrakharchik, and S. Giorgini. Spin dynamics and andreev-bashkin effect in mixtures of one-dimensional bose gases. *Physical Review Letter*, 121:025302, 2018.

[63] D. S. Petrov, C. Salomon, and G. V. Shlyapnikov. Weakly bound dimers of fermionic atoms. *Phys. Rev. Lett.*, 93:090404, Aug 2004.

[64] Tony Prat, Dominique Delande, and Nicolas Cherroret. Quantum boomeranglike effect of wave packets in random media. *Phys. Rev. A*, 99:023629, Feb 2019.

[65] J. D. Pritchard, J. A. Isaacs, and M. Saffman. Long working distance objective lenses for single atom trapping and imaging. *Review of Scientific Instruments*, 87:073107, 2016.

[66] Anand Krishnan Ramanathan. A ring with a spin: Superfluidity in a toroidal bose-einstein condensate, 2011. PhD thesis, University of Maryland.

[67] James E. Rau. Real-time complex spatial modulation. *JOURNAL OF THE OPTICAL SOCIETY OF AMERICA*, 57(6):798–802, 1967.

[68] Stephan Reichelt, Ralf Häussler, Gerald Fütterer, Norbert Leister, Hiromi Kato, Naru Usukura, and Yuuichi Kanbayashi. Full-range, complex spatial light modulator for real-time holography. *OPTICS LETTERS*, 37(11):1955–1957, 2012.

[69] Richard J. Roy. Ytterbium and lithium quantum gases: Heteronuclear molecules and bose-fermi superfluid mixtures, 2017. PhD thesis, University of Washington.

[70] Timur Michael Rvachov. Ultracold $^{23}$Na$^{6}$Li Molecules in the triplet ground state, 2018. PhD thesis, MASSACHUSETTS INSTITUTE OF TECHNOLOGY.

[71] C. Ryu, P. W. Blackburn, A. A. Blinova, and M. G. Boshier. Experimental realization of josephson junctions for an atom squid. *Phys. Rev. Lett.*, 111:205301, Nov 2013.

[72] Roshan Sajjad, Jeremy L. Tanlimco, Hector Mas, Alec Cao, Eber Nolasco-Martinez, Ethan Q. Simmons, Flávio L. N. Santos, Patrizia Vignolo, Tommaso Macrì, and David M. Weld. Observation of the quantum boomerang effect. *Phys. Rev. X*, 12:011035, Feb 2022.

[73] Jeffrey B. Sampsell. Digital micromirror device and its application to projection displays. *Journal of Vacuum Science and Technology B*, 12(6):3242–3246, 1994.

[74] M.S. Santhanam, Sanku Paul, and J. Bharathi Kannan. Quantum kicked rotor and its variants: Chaos, localization and beyond. *Physics Reports*, 956:1–87, April 2022.

[75] C. H. Schunck, M. W. Zwierlein, C. A. Stan, S. M. F. Raupach, W. Ketterle, A. Simoni, E. Tiesinga, C. J. Williams, and P. S. Julienne. Feshbach resonances in fermionic $^{6}$Li. *Phys. Rev. A*, 71:045601, Apr 2005.

[76] Jun Hui See Toh, Katherine C. McCormick, Xinxin Tang, Ying Su, Xi-Wang Luo, Chuanwei Zhang, and Subhadeep Gupta. Many-body dynamical delocalization in a kicked one-dimensional ultracold gas. *Nature Physics*, 18:1297–1301, 2022.

[77] ND Shemonski, SA South, YZ Liu, SG Adie, PS Carney, and SA Boppart. Computational high-resolution optical imaging of the living human retina. *Nature Photonics*, 9(7):440–443, 2015.

[78] Y. R. P. Sortais, H. Marion, C. Tuchendler, A. M. Lance, M. Lamare, P. Fournet, C. Armellin, R. Mercier, G. Messin, A. Browaeys, and P. Grangier. Diffraction-limited optics for single-atom manipulation. *Phys. Rev. A*, 75:013406, Jan 2007.

[79] Jun Hui See Toh. Interaction-driven dynamical delocalization in a kicked one-dimensional ultracold gas, 2022. PhD thesis, University of Washington.

[80] Jun Hui See Toh, Mengxin Du, Xinxin Tang, Ying Su, Tristan Rojo, Carson O. Patterson, Nicolas R. Williams, Chuanwei Zhang, and Subhadeep Gupta. Evidence for a many-body anderson metal-insulator transition using kicked quantum gases. *arXiv:2305.14817*, 2023.

[81] Anton Travinsky, Dmitry Vorobiev, Zoran Ninkov, Alan Raisanen, Manuel A. Quijada, Stephen A. Smee, Jonathan A. Pellish, Tim Schwartz, Massimo Robberto, Sara Heap, Devin Conley, Carlos Benavides, Nicholas Garcia, Zach Bredl, and Sebastian Yllanes. Evaluation of digital micromirror devices for use in space-based multi-object spectrometer application. *Journal of Astronomical Telescopes, Instruments, and Systems*, 3(3):035003, 2017.

[82] G. E. Volovik, V. P. Mineev, and I. M. Khalatnikov. Theory of solutions of a superfluid fermi liquid in a superfluid bose liquid. *Soviet Physics, JETP*, 69:675, 1975.

[83] Kaiqiang Wang, MengMeng Zhang, Ju Tang, Lingke Wang, Liusen Hu, Xiaoyan Wu, Wei Li, Jianglei Di, Guodong Liu, and Jianlin Zhao. Deep learning wavefront sensing and aberration correction in atmospheric turbulence. *PhotoniX*, 2(8), 2021.

[84] D. J. Wineland and H. Dehmelt. Proposed 1014 $\Delta\nu/\nu$ laser fluorescence spectroscopy on Tl+ mono-ion oscillator. *Bulletin of the American Physical Society*, 20(4):637–637, 1975.

[85] K. C. Wright, R. B. Blakestad, C. J. Lobb, W. D. Phillips, and G. K. Campbell. Driving phase slips in a superfluid atom circuit with a rotating weak link. *Physical Review Letters*, 110:025302, 2013.

[86] Xiang-Chuan Yan, Da-Li Sun, Lu Wang, Jing Min, Shi-Guo Peng, and Kai-Jun Jiang. Production of degenerate fermi gases of 6li atoms in an optical dipole trap. *Chinese Physics Letters*, 38(5):056701, 2021.

[87] Xianhong Zhao and Xu Ma. Off-axis aberration correction for a reflective coded aperture snapshot spectral imager. *Optics Letters*, 47(5):1202–1205, 2022.

[88] Ziyun Zhuang and Ho Pui Ho. Application of digital micromirror devices (dmd) in biomedical instruments. *Journal of Innovative Optical Health Sciences*, 13(6):2030011, 2020.

[89] M. W. Zwierlein, C. A. Stan, C. H. Schunck, S. M. F. Raupach, S. Gupta, Z. Hadzibabic, and W. Ketterle. Observation of bose-einstein condensation of molecules. *Phys. Rev. Lett.*, 91:250401, Dec 2003.